T-3179

The Development and Ground Testing of the U.S. Geological Survey Airborne Sixty-Hertz Reconnaissance System

by

David C. Merkel

ProQuest LLC.
789 East Eisenhower Parkway
P.O. Box 1346
Ann Arbor, MI 48106 – 1346

T-3179

A thesis submitted to the Faculty and Board of Trustees of the Colorado School of Mines in partial fulfillment of the requirements for the degree of Master of Science in Geophysics.

Golden, Colorado

Date 4/7/86

Sign: David C. Merkel
David C. Merkel

Approved: George V. Keller
George V. Keller
Thesis Advisor

Golden, Colorado

Date 7 April 1986

P R Romig
Phillip R. Romig, Ph.D.
Department of Geophysics

ABSTRACT

Usually the sixty hertz electromagnetic fields created by power line transmission are an undesirable source of cultural noise. As a consequence, most geophysical equipment attempts to filter out this frequency. In some areas this filtering is inadequate, and it is impossible to detect any useful signal over the sixty hertz noise. As part of the U.S. Geological Survey sixty-hertz project, this study was undertaken to determine if the sixty hertz fields can be used for the detection of anomalies in electomagnetic prospecting.

Methods such as VLF and AFMAG have proven to be effective methods by measuring two orthogonal components of the magnetic part of the electromagnetic field. The data are resolved by determining the polarization characteristics which indicate anomalous field behavior related to contrasting conductive structures within the earth. With this analysis of field data in mind, the U.S. Geological Survey has designed a receiver that measures the ambient sixty hertz electomagnetic field for purposes of airborne reconnaissance work.

Preliminary ground testing with the incorporation of a phase lock loop presented some interesting results. Survey lines were recorded over three general categories of electromagnetic anomalies. Profiles for the first case were located over a buried pipe of known location. The second group

was located over fault zones occurring in the mountainous regions to the west of Denver, and the third was located over geologic contacts of dipping sedimentary structure. Response curves of highs and inflections occur throughout the data with good resolving capabilities including areas near power lines. The worst responses were obtained over the mountainous fault areas. There, the signals were comparatively low and behaved erratically, especially when directly over the faults. It is probable that the natural fields due to sferics have a major contribution to the horizontal field in some areas. Similar to the problems encountered in AMT, the highly variable nature of its sferic source precludes digital acquisition of these fields using the current sixty-hertz instrumentation.

Nonetheless, the sixty-hertz system shows promise as numerous anomalies were detected. The system is easily operated and makes extensive use of digital electronics for massive data handling and immediate field evaluation of the response.

TABLE OF CONTENTS

TABLE OF CONTENTS (continued)

LIST OF FIGURES

LIST OF FIGURES (continued)

LIST OF TABLES

ACKNOWLEDGEMENTS

I thank Dr. Frank Frischknecht for the opportunity to work for the U.S. Geological Survey. He provided the initial design of the sixty hertz system which made this research possible. Thanks to Drs. Kaufman, Keller, and Ibrahim, my professors, for their advice and consultation throughout my attendence at the Colorado School of Mines. I am also appreciative of the entire U.S.G.S. electronics lab in Denver, particularly Jerry Bradley for his design of the digital acquistion system and Don Rohret for his persistence in solving the analog and digital mixing problems. Finally, I am very grateful to my wife, Sylvia, for her editing and support during much of this project.

I. INTRODUCTION

With measurements of the ambient 60 hertz (Hz) electromagnetic (EM) field, the electrical substructure of the earth can studied. Anomalous EM fields that arise in the vicinity of conducting lateral inhomogeneities are detectable. They are observed in profile by plotting the polarization parameters which use ratios of orthogonal magnetic field components. Data behavior is variable and dependent on the inducing primary fields.

Natural EM fields having a spectral range containing 60 Hz originate from a variety of sources (Kaufman and Keller, 1981). One important source is meteorologic activity due to lightning associated with thunderstorm activity. Major lighting stroke discharge takes place in the lower latitudes with diurnal and yearly variations. The fields propagate radially outward from their sources in the Earth-ionosphere cavity where, at great distances from their source, they behave like plane waves (Labson et al., 1985). Associated with each wave are a vertical electric field and transverse magnetic field perpendicular to the propagation direction. As a consequence of the earth's conductance, a radial electrical field within the earth is directed from the source.

Where the earth may be assumed to be a homogeneously layered structure, for practical purposes the horizontal

magnetic and electric fields are proportional to the primary field's strength and the earth's response parameter. Ratios of these orthogonal field components removes the primary field's dependence, but reduces the sensitivity of the response function which contains information regarding the earth's conductivity. This ratio is the apparent wave impedance and is proprortional to the square root of the apparent resistivity. However, the presence of lateral conducting inhomogeneities polarize the field and, in the special case of E-polarization, produces an anomalous magnetic field (Kaufman and Keller, 1981).

As its source Audio MagnetoTellurics (AMT) uses sferics at frequencies above and below 60 Hz. This method has been extensively studied (e.g., Strangway et al., 1973 and Hoover et al., 1978). The signals behave erratically requiring equipment with a large dynamic range and the ability to select random spikes in order to overcome background noise. Usually, coherent spikes of magnetic and electric field records yield consistant ratios, but in the presence of inhomogeneities these ratios deviate considerably due to changing source directions.

Another geophysical method which uses sferics as its source is the Audio Frequency MAGnetic (AFMAG) technique (Ward, 1959). As in the proposed sixty-hertz method, ratios of orthogonal EM fields are compared for purposes of anomaly mapping. Both systems can employ either airborne or ground

equipment. AFMAG uses two frequencies, 150 and 510 Hz, to avoid harmonics of 60 Hz frequencies and, therefore, power line energy. In the azimuth direction which is determined by the horizontal polarization, only vertical tilt angles were examined. Nonetheless, data results obtained using the sixty-hertz method agree with those obtained using AFMAG. For example, phenomenon such as horizontal shifting of curve inflections in relation to the anomaly's location (Ward, 1966), compare to those seen in sixty-hertz data. Recently, Labson et al., (1985) have successfully demonstrated enhancement of the AFMAG method by use of the 'tipper' (Vozoff, 1972). Similarly, this procedure could apply to sixty-hertz data processing.

Another method that is similar to the sixty-hertz system is the Very Low Frequency (VLF) method. Both use a constant and remote transmitter. Similar to sferics in the primary field orientation, the VLF propagating waves produce anomalous EM fields that are due to conducting lateral inhomogeneities. VLF data behavior expresses characteristics that aid in differentiating sferics sources from power line energy.

Experience gained from use of these other geophysical methods provides a basis for understanding the sixty-hertz method. In all other methods, the source fields are assumed to be horizontal permitting the assumption that the vertical field is solely caused by the secondary anomalous field. Therefore,

the vertical field's behavior has been the the best indicator of the anomaly. For the sixty-hertz system these fields are also sensed; however, because of the additional vertical primary field created by power lines, the conventional interpretation of the response can be altered.

The most important source of 60 Hz EM energy is propagated by man-made power distribution systems. In general, currents that are induced from above the earth produce secondary fields resembling their primary source fields. Power lines and sferics generate horizontal electric fields in accordance to Faraday's law. In both cases the electrical fields cause secondary currents to flow in the ground dependent on the earth's conductive parameters and generate anomalous EM fields when in the presence of conducting lateral inhomogeneities. Although the electric fields have different orientation in the horizontal plane, only in the case of E-polarization do the anomalous magnetic fields occur. Different primary magnetic field directions of the two sources have a profound control on data curve shapes, but when properly treated do not prohibit detection of the anomaly.

Union Rural Electric Association located north of Golden, Colorado, was the source of the following information. Power line networks are divided into high voltage transmission lines and local power lines. The high voltage lines have various

voltages from 110 kilovolts and up. These transmission lines are stepped-down to 7.2 kilovolts and feed into the local power lines which follow most roads.

Each line has three conductors carrying current 120 degrees out of phase from the others along with separate ground conductor(s) which tie into earth ground every other pole. It is the resulting sinusoidal sum of current in these conductors which induce secondary currents into the earth. As an example, during one reading 42 amperes, 3 amperes, and 2 amperes of current were being used in a 110 kilovolt line resulting in an effective line source of 40.5 amperes.

Frequency deviations on these lines are guaranteed to be less than +/- .05% of 60 Hz. In reference to a separate crystal oscillator this error would produce a beat frequency of approximately a 33 second time period. In the lab where an unusually large and varying EM field exists, the beat frequency always had more than a one minute period, which is well within the specified limits. Nonetheless, it was because of this beat frequency and the slowness of the computer interface that a phase lock loop curcuit was required.

Although the sixty-hertz system was designed for airborne reconnaissance mapping of the anomalous electromagnetic field, during this testing and development the unit has been used exclusively on the ground in a vehicle mount. Because of the

usually well behaved 60 Hz signals, it is possible to obtain large and accurate quantities of data using a digital aquisition system. Analysis of phase information repeatedly demonstrated this, revealing excellent sensitivity to conductive contrast. Not only did the equipment prove exceptional, but equally remarkable was the multitude of tasks performed by the system's computer, a Hewlett-Packard 71B. One computer was responsible for all data handling from collection to plotting of the results.

II. INSTRUMENTATION

The sixty-hertz instrumentation incorporates an elaborate analog network in conjunction with a digital acquisition system (DAS). Through mu-metal cored coils three channels of EM information are sensed in a mutiplexed fashion. Separately, the signals are amplified, filtered to pass 60 Hz, split into real and quadrature components, and digitized for storage on magnetic media.

By means of analog circuitry the amplitude derived from the real and quadrature parts are fed into a level detector for auto-gain ranging control creating a feed back loop. Within this loop and after the first stage of filtering a phase lock loop (PLL) senses the signal's frequency. Signal output from the PLL is used for precise clocking of the N-path filters and phase synchronous detectors. As a consequence, this part of the system functions as a single unit.

Refering to the flow chart in Figure 1, the sixty-hertz multi-channel system is seen in whole. Because the system was intended for airborne use, the three channels are designated as transverse, in-line, and vertical, in reference to the flight path.

II.1 Analog Amplifier and Filters

From the flow chart in Figure 2 it can be seen how each

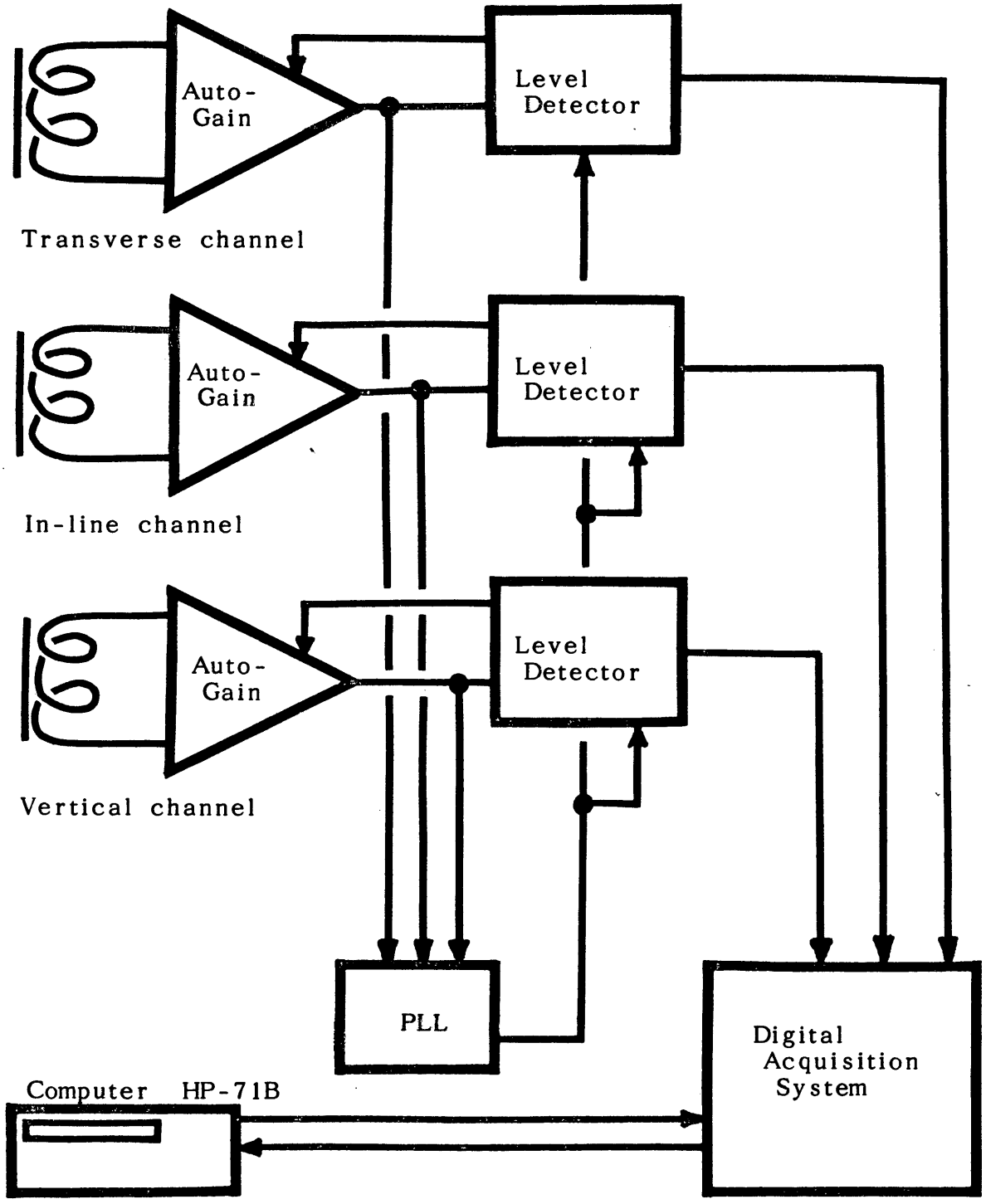

Figure 1. Flow chart of the three channel sixty-hertz receiver instrumentation.

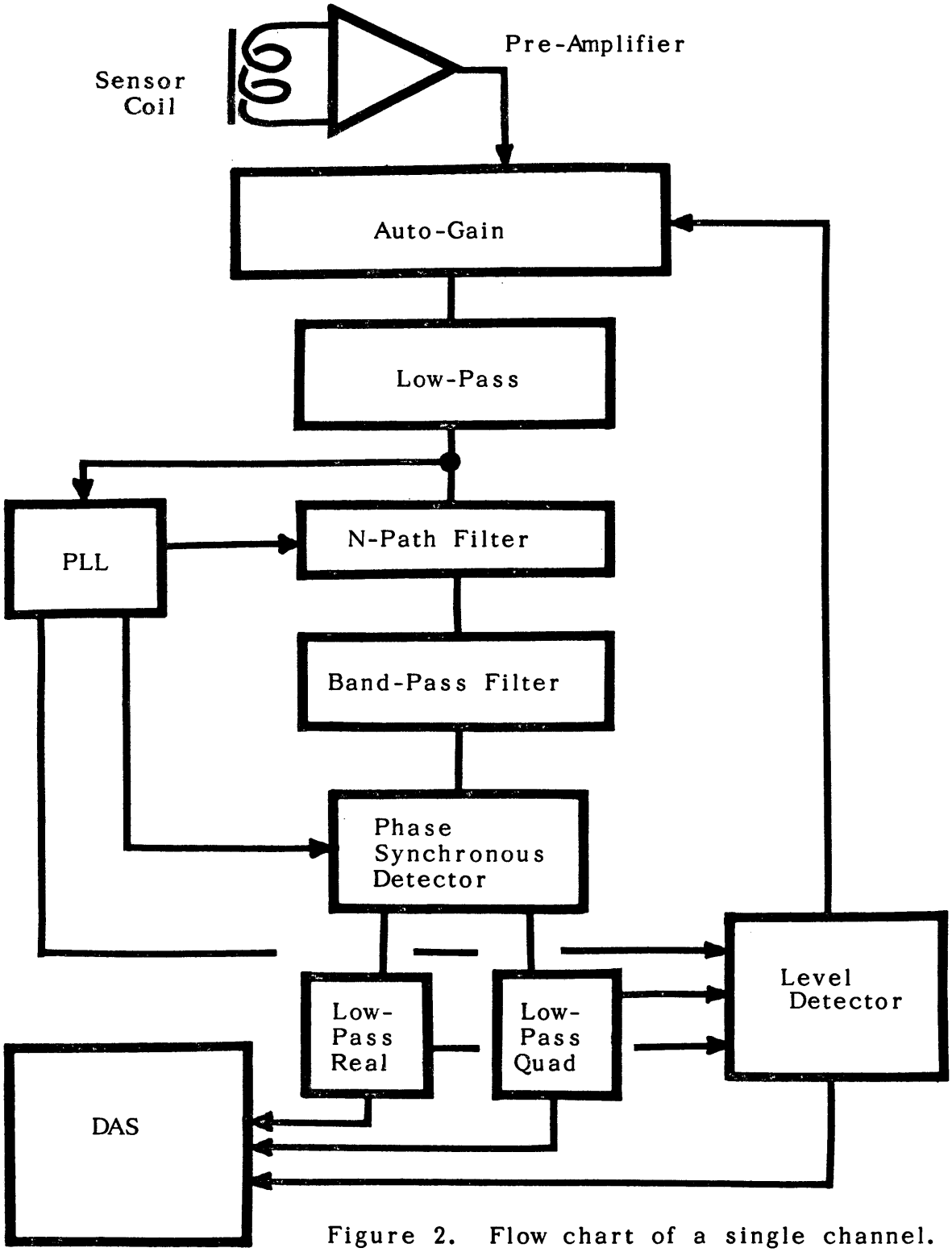

Figure 2. Flow chart of a single channel.

channel may be divided into functional blocks. The PLL and DAS are separate and serve all three channels in the same manner.

Signals of the EM field enter the system through the sensor coils. Because of the low frequency measured, coil sensitivity was a main design criterion. Each channel has two identical coils wired in series. Approximately 25 thousand turns of 32 gauge wire were wound around a core composed of mu-metal MM-60 alloy 16.5 cm (6.5 in) long and 2.5 cm (1 in) in diameter. Using a scrambled winding technique minimized capacitive and self-inductive effects between wire wrappings. Surrounding the coil with conductive foil connected to a common ground formed a Faraday Shield. When done properly, the foil around the coil does not make any connected loops thereby avoiding effects generated by eddy currents in the shield. Table 1 lists the resulting measured specifications (two coils per channel).

Table 1

Measured Sensor Coil Specifications

	f^0	L	Q	R	R^0
transverse:	790 Hz	94.1 h	23	2570 Ω	2277 Ω
in-line:	995 Hz	90.1 h	21	2696 Ω	2292 Ω
vertical:	820 Hz	93.2 h	23	2546 Ω	2257 Ω

Values in Table 1 were measured using a GenRad GR 1657 RLC digibridge. Columns marked L and R^0 are self-inductance in henries and direct current (dc) resistance in ohms, respectively. The response parameter $Q = \omega L/R$ from which the impedance resistance, R, was calculated was measured at 100 Hz.

In order to operate the coils in a linear range and make the coil capacitance negligible, the resonant frequency, f^0, must be much greater than 60 Hz. Further tuning by adding resistance and capacitance in parallel to the coil output peaked the frequency response at 60 Hz.

Coil signals feed into the pre-amplifier where they are boosted by a factor of ten. Since some of the signal at this point is unwanted contribution from higher frequencies, a passive low-pass filter filters the signal before it enters the main auto-gain ranging amplifier. Because of their low noise and low dc offset characteristics, OP-27 operational amplifiers (op-amp) were used throughout the design making the large gains possible.

The auto-gain amplifiers are an arrangement of four cascaded op-amps having gains of 2^1, 2^2, 2^4, and 2^8. Gains from 2^0 to 2^{15} in steps of 2x are acquired by switching on or off the proper combination of op-amps. The switching is controlled by feedback from the level detectors. Level detectors monitor the output voltage (v) levels between 1v and 3v so that

once the voltage is outside these ranges a gain change is triggered. Due to the long time constant involved in filtering the signal before its input into the level detector, the gain updating must be clocked to permit a settling time. Clock pulses that are too quick prevent the system from settling, resulting in ocsillating gains. Usually half a second (1.875 Hz) between pulses is adequate; however, if the input signal is behaving erratically, slowing the pulse even more buffers the instumentation against spurious gain changes.

Upon amplification the signal enters a series of filters to extract the 60 Hz. There are three active low-pass filters used in the system which are two-cascaded equal component Sallen-Keys (Lancaster, 1980). There are also two active band-pass filters in the system. One is a multiple feedback band-pass (Burr-Brown, 1966) and the second is an N-path filter (Franks, 1973). The N-path filter is a series of switched capacitors to ground clocked by the PLL. Hence, source signal for the PLL is taken before the N-path filter to avoid the creation of an unstable feedback loop.

The PLL provides the system's timing. Originally a crystal was used; however, a slight difference in frequency between it and the 60 Hz signal produced a beat frequency. Beat frequencies are caused by imposition of one frequency on another and are equal to the difference between the two

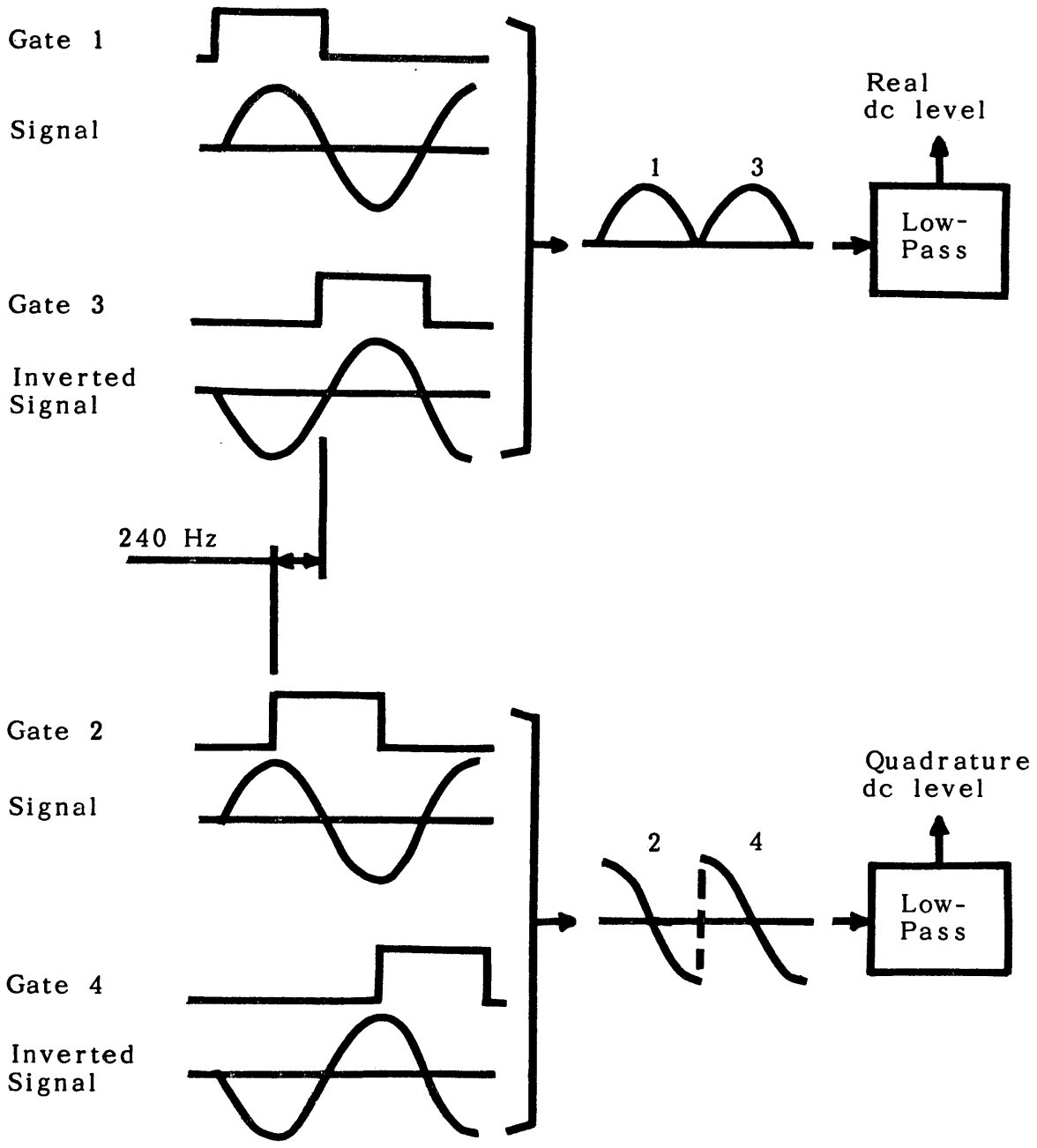

Figure 3. The phase synchronous detector operation.

frequencies. The imposition occurs in the phase synchronous detector (PSD) where the signal is divided into its real and quadrature parts. Figure 3 depicts this process and shows the gating. Gate timing comes from the system clock. Although the gates may shift in time, any frequency difference will produce beat oscillations in the real and quadrature dc levels. Likewise, any extraneous clock pulse causes flipping between the real and quadrature parts.

II.2 Digital Data Acquisition

Once the signals are reduced to dc levels of real and quadrature, six channels of information enter the DAS to begin the recording process for subsequent data analysis. Shown in the flow chart of Figure 4 is the DAS operation. This section of the instrumentation was designed for in-flight data observation for quality control and not for mass storage of the data. Nonetheless, for ground use it serves as a means of data recording and storage via the tape drive.

The multiplexer (MUX) is initialized once and is set for the number of channels to be sequentially read for each station. Because of the phase lock loop's ellimination of a beat frequency, there is no maximum sampling time for stationary acquisition. Sampling time depends upon statement execution speed of the computer which for the HP-71B is approximately fifty milliseconds per channel. For each channel the computer

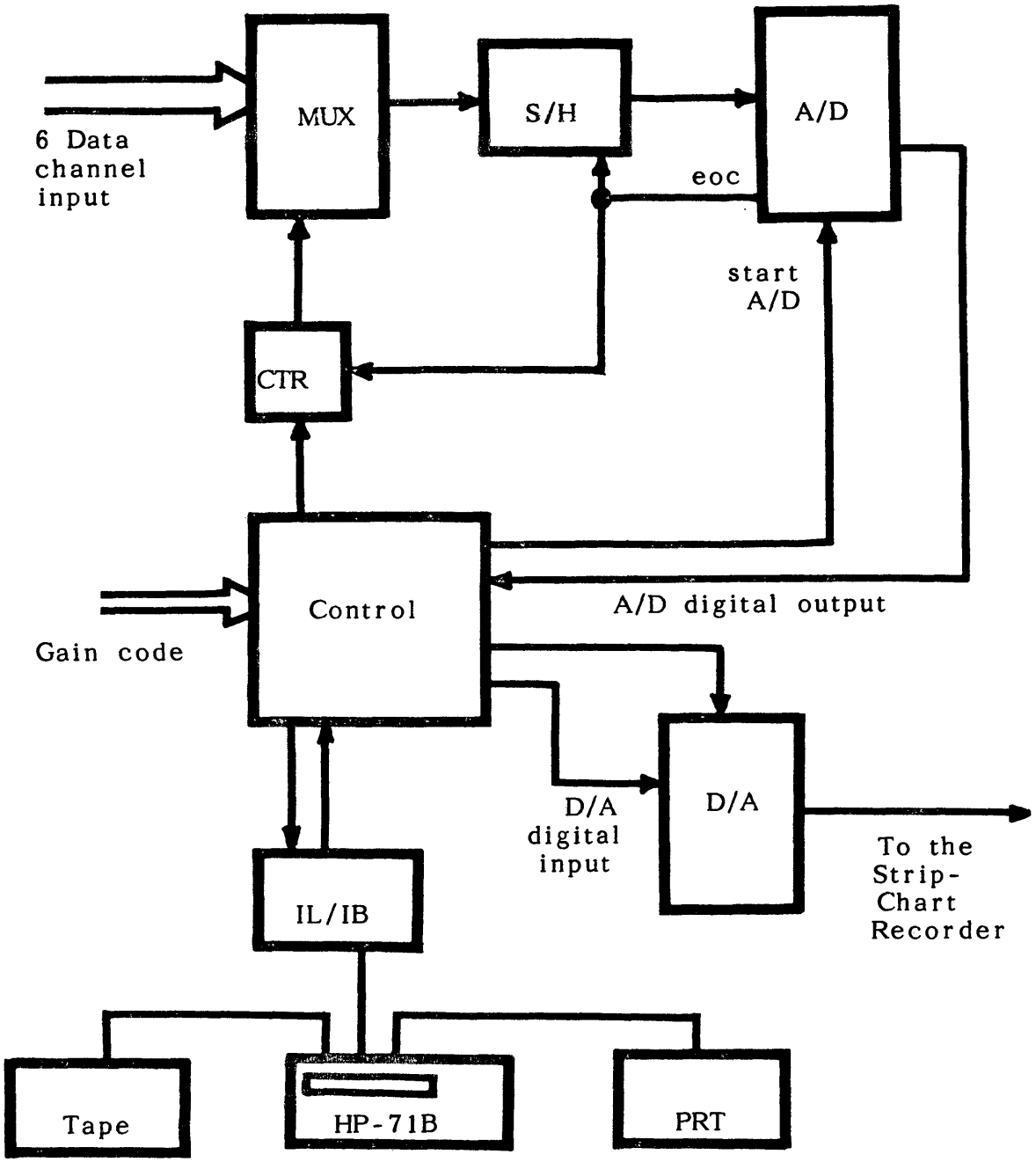

Figure 4. Flow chart of the digital acquisition system.

signals the analog to digital converter (A/D) to start. Simultaneously with the end of conversion, it clocks the counter (CTR) responsible for changing the MUX channel and sets the sample-and-hold (S/H) for the next reading. At that time the computer reads in two data bytes, thus completing the process that can be done in one computer statement for each channel. Specifics concerning general input/output may be found in Appendix A.

Hewlett-Packard's interface-loop-to-interface-bus (IL/IB) converter facilitates data transfer between the DAS and the computer. At this point there is a differentiation of the computer's function depending on whether the system is an airborne or a ground unit. If airborne, the reduced data are put into a digital to analog converter (D/A) feeding a strip chart recorder. Otherwise, the data are sent to the printer (PRT) and later stored on tape.

II.3 Calibration

Although during board layout all components were matched, there exist slight phase and amplitude differences between the three channels. Because polarization parameters depend on component ratios, these differences must be calibrated and corrected for within the software. Differences in coil sensitivity should also be compensated for; however, they were assumed to be minor and were thus neglected. Nonetheless, coil

sensitivity estimates were made in an indirect manner.

Amplitude differences were compensated for by calibrating the gains. Before calibration, windows of input voltages were determined for each gain step. With this as a guide, ratios of digitized output voltages to input voltages were averaged and entered into the program as gain tables.

Phase corrections were derived by measuring phase differences when the same input signal was used for all channels. Program statements correct in-line and vertical phases in relationship to the transverse phase. Phase measurements are referenced to the summation of the three component signals. They are compared by the PLL which sets the system timing, i.e., PSD.

Judgements of magnetic field strength in relation to measured voltages were made in comparison to AMT data taken on the Kassler line. From this AMT data the apparent resistivity for 45 Hz and 75 Hz was known. Amplitudes of 60 Hz electric and magnetic fields were collected at the same sites. Working backwards from the known AMT apparent resistivity values, the sensitivity of the 60 Hz system was calculated. The results vary from .5 gammas (γ)/millivolt (mV) to 3.4γ/mV with .8γ/mV being considered the best average. Conclusions comparing field strengths of sferics to power lines contributions are based on these calculations and shall be discussed later

upon review of the forward model relating to multiple sources. Further information concerning gain, phase, and coil calibrations are in Appendix B.

III. Fundamental Model of a Polarized EM Field

Anomalous magnetic fields which are a function of the earth's conductive subsurface can be measured with the sixty-hertz system. This statement is based on several physical laws. Through the Biot-Savart law, it is seen that, in general, magnetic fields arise due to current flow (Kaufman and Keller, 1985). In agreement with Ohm's law, electric fields (E) within the earth create current densities proportional to the earth's conductivity. Putting this in equation form where H is the anomalous secondary field yields

$$H \propto I/\text{area} = \sigma E.$$

Thus, in the presence of a uniform electric field the current flow (I) and therefore the magnetic field response is dependent on the earth's conductivity (σ) and the area of current flow.

Refering to Figure 5 for illustrative purposes, consider a cross-section of the earth having current elements going into the page as represented by the circles. For a horizontally layered earth, all horizontal current concentrations are in the same plane resulting in a purely horizontal secondary field with no vertical component above the surface. In the event that one of the current concentrations is larger due to either a higher conductivity or a less effective area for the current to pass through, an anomalous field exists. In Figure 5 the associated

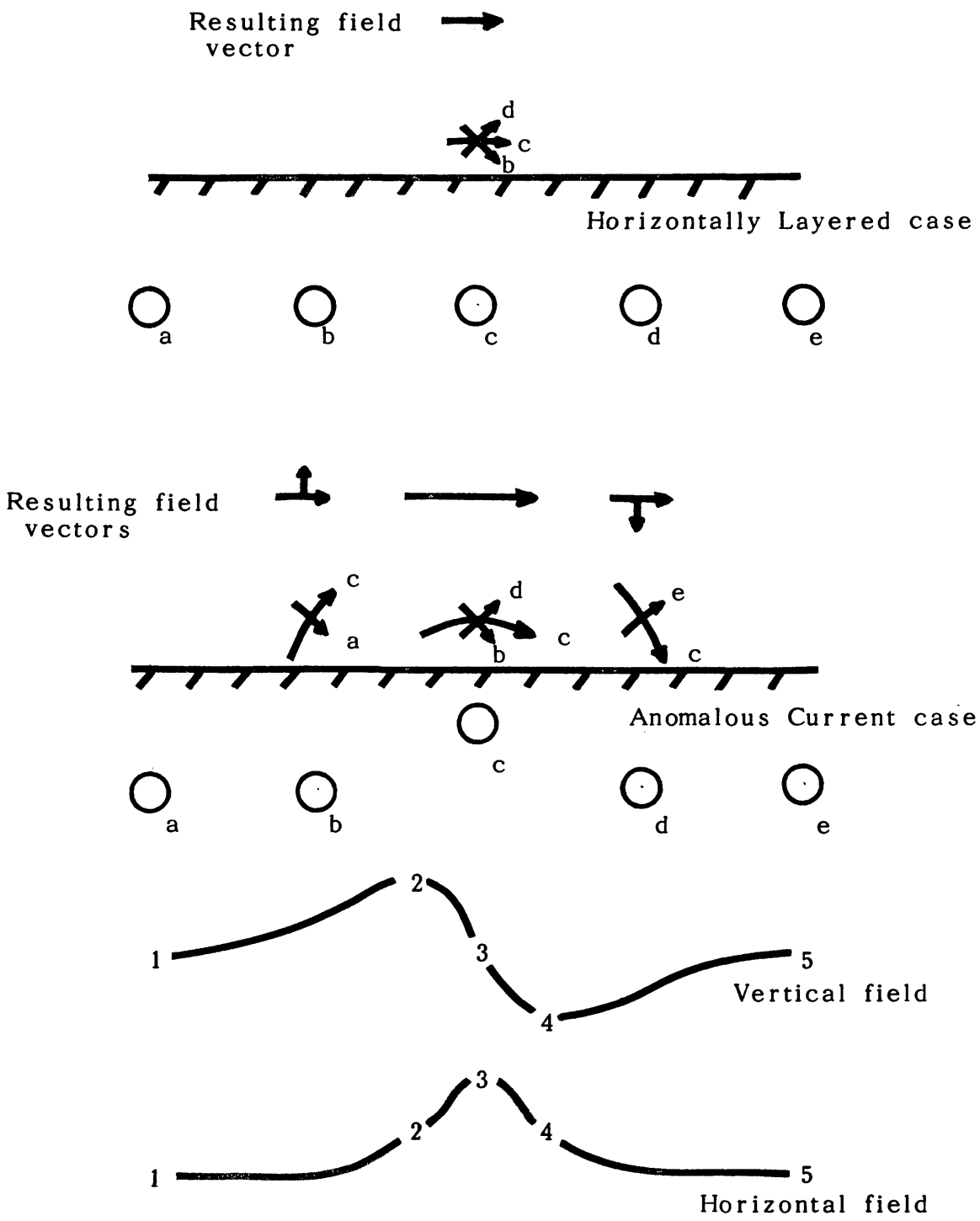

Figure 5. Simplified current element behavior.

vector field components are shown above the cross-sections. For the anomalous current case, the vector field components are plotted below it in profile.

Because of the principle of superposition, the curve of the component in the direction of the primary inducing field has an added dc offset. This becomes significant when taking field ratios as shown by the following two examples. First, let us assume zero dc offset and reasonable field values that would produce the anomalous curves similar to those shown in Figure 5. Division of the vertical field by the horizontal field emphasizes the inflection representing the anomaly. For the second case we will assign reasonable values, but with a dc offset in the vertical field that represents the addition of the power line source. Table 2 is a list of these values along with their appropriate divisions. Notice that a plot of the vertical per horizontal ratios has been transformed into a curve low and shifted with respect to the position of the anomaly.

Table 2

Example Component Values Correlating to Figure 5

station:	1	2	3	4	5
vertical:	10	20	10	0	10
horizontal:	1	5	10	5	1
vert/horz:	10	4	1	0	10

Without the vertical primary field, ratios emphasize the anomaly, but with poorly behaved values this does not happen. Furthermore, as seen in the second case above, using ratios may change the curve character while also introducing curve shifting.

Before attemping to examine any of the details, a discussion of polarized fields is in order. The primary fields play an important role, but once understood need not make the solution ambiguous.

III.1 Polarization Parameters

With the exception of EM fields in areas located near power lines, most primary 60 Hz magnetic fields due to culture are nearly vertical. Because of the large distances to the source, primary magnetic fields due to sferics are horizontal. In both cases plane wave sources are defined with their associated electric fields oriented in the horizontal plane (Born and Wolf, 1980). Although the electric fields may have different orientations in the horizontal plane, when considering two dimensional electrical stuctures only in the case of E-polarization do anomalous magnetic fields occur. In the presence of lateral inhomogeneities both sources are seen to generate anomalous fields due to secondary current flow. The anomalous fields experience phase shifting relative to their primary fields; however, in general, multiple sources can be assumed to have differing phases. Two sinusoidal signals with a

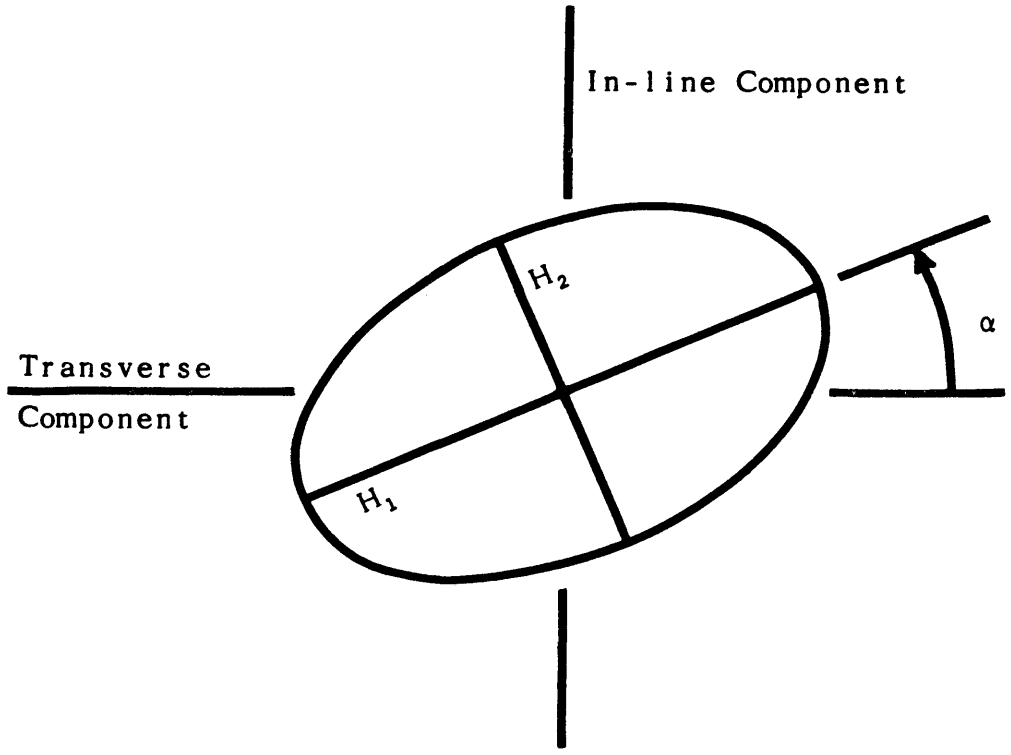

Figure 6. An elliptically polarized wave in the horizontal plane.

phase difference produce ellipitical polarization. Therefore, polarization changes in the presence of non-varying multiple plane wave sources indicate a change of the electrical structure within the earth.

Whenever two harmonic fields are compared, the tip of their resulting vector plotted in polar coordinates defines a polarized wave. Figure 6 diagrams the parameters for the horizontal polarization ellipse. The angle α refers to the tilt angle and is calculated (Smith and Ward, 1974) as

$$\alpha = .5 \text{ arctangent } \left[\frac{2\, A_l/A_T \cos(\Delta\phi)}{1 - (A_l/A_T)^2} \right]$$

where

A_l = in-line amplitude
A_T = transverse amplitude
$\Delta\phi = \phi_l - \phi_T$ phase change (in-line - transverse).

The tilt varies between 0° to 45° and is always taken in reference from the axis marked 'transverse' in the figure to H_1. At 45°, unity amplitude ratio creates a discontinuity in the tilt resulting in a circularly polarized wave. Further counter-clockwise rotation of the ellipse causes the tilt to jump to -45° while interchanging H_1 and H_2.

The other parameter describing the polarized wave is the ellipticity, and it is calculated (Kauahikaua, 1982) as

$$\frac{H_2}{H_1} = \frac{A_l\, A_T \sin(\Delta\phi)}{[A_l \cos(\Delta\phi) \sin(\alpha) + A_T \cos(\alpha)]^2 + [A_l \sin(\alpha) \sin(\Delta\phi)]^2}.$$

Polarization parameters are a mathematical tool which may or may not aid the interpretation of EM wave behavior. Therefore, in addition to polarization parameters, investigation of the amplitude ratios and the phase changes derived from the EM response enhances understanding of the data.

III.2 Free Space Coupling of an Infinitely Long Current Element

For purposes of modeling the least complex form of a polarized EM field, a free space model was chosen where an infinitely long power line source induces a secondary voltage into an infinitely long current element. Due to these currents, voltages are induced into the receiving coil. Because of the thin conductor, the solution assumes no current interaction, and coupling information is contained within the inductance formulas.

From Faraday's law and the Biot-Savart law it can be shown that in the case of a thin conducting ring where permeability (μ) is constant, inductance is proportional only to the geometric factors defining the position of the primary field source in relationship to the conductor (Telford et al., 1976). There are two types of inductances: mutual and self-inductance. Mutual inductance occurs when an external magnetic field in accordance with Faraday's law induces a voltage into another conductor. When the induced field creates a current opposing the tendency for current to change in that conductor it is considered self-inductance in accordance with Lenz's law (Johnk, 1975).

Voltage induced into a conductor is the sum of electromotive forces due to mutual and self-inductances:

$$V_2 = emf_2 + emf_1. \qquad (1)$$

Providing there is uniform current density across the conductor, application of Ohm's law and the definition of inductances relates equation 1 to a first order linear differential equation:

$$\frac{dI_2}{dt} + \frac{R_2}{L_2} I_2 = \frac{-M_{12}\, dI_1}{L_2\, dt}. \qquad (2)$$

where

I_2 = secondary current in the conductor
R_2 = total resistance of the secondary circuit
L_2 = total self-inductance of the secondary circuit
I_1 = primary current located at the source
M_{12} = mutual inductance: I_1 to the secondary circuit

Notice that the contribution due to sferics would add current to I_2; however, because the resistance R_2 and self-inductance L_2 are functions of the medium, they would operate on any additional current in the same manner yielding a similar equation.

Our interest is solving for the voltage induced into the receiver coils due to both sources. Eq. 2 solves for the current in the secondary current element. By reappling eq. 2 with the solution of I_2 as the primary current and R_3, L_3 as the measured coil impedance values, the voltage in the receiver coils due to the current element can be found. Applying eq. 2 once more using I_1, R_3, and L_3 solves for the voltage in the receiver coil due to the primary field. By

summing these two voltages, the steady-state sixty-hertz response due to the field about the current element can be written as

$$V_3 = K_{11} \{ [M_{12} K_1 + M_{23} K_{30} K_2] \sin(\omega t) + [M_{12} K_3 + M_{23} K_{30} K_4] \cos(\omega t) \} \quad (3)$$

where

$$K_{11} = \frac{A_1 Q_3}{Q_2^2 + 1} \qquad (A_1 \text{ is the primary amplitude})$$

$$K_1 = 1 - \omega$$

$$K_2 = \frac{Q_2}{Q_2^2 + 1} (Q_2\omega - Q_2 - Q_3 + Q_2/Q_3)$$

$$K_3 = \omega/Q_3 + Q_3$$

$$K_4 = \frac{Q_2}{Q_2^2 + 1} (Q_2 Q_3 + Q_2\omega/Q_3 + \omega - 1)$$

$$K_{30} = \frac{M_{12}}{L_2}$$

M_{13} = mutual inductance: power line to coils

M_{23} = mutual inductance: current element to coils

$$Q_2 = \frac{\omega L_2}{R_2} \qquad \text{(response parameter: current element)}$$

$$Q_3 = \frac{\omega L_3}{R_3} \qquad \text{(response parameter: receiver coils).}$$

Examining eq. 3, it can be seen that the real and quadrature parts of the equation are those factors modifing the sine and

cosine functions, respectively. Reductions to amplitude and phase are given by

$$\text{Amplitude} = (\text{real}^2 + \text{quad}^2)^{\frac{1}{2}} \tag{4}$$

$$\text{phase} = \text{arctangent}\left(\frac{\text{quad}}{\text{real}}\right). \tag{5}$$

In the case where there is one source, the K_{11} term is proportional to all components and divides out upon taking component ratios. Thus, polarization effects due to changes in the primary field's magnitude are eliminated. From the remaining expression the left side of the sum in both the real and quadrature parts represents the primary field's contribution while the right halves describe the secondary current element.

The mutual inductance between a line source and a coil is a function of the magnetic flux intersecting the area of the coil and their separation distance. Assuming that the area of the coils and the number of windings are equal, upon taking component ratios of the fields the mutual inductance term reduces to

$$M_{13} \text{ and } M_{23} = \frac{\cos(\theta)}{r}$$

where θ is the angle of the coil's plane in relation to the source element at a separation distance r. The mutual inductance term describes the spatial relationship of the

secondary field's coupling to the receiver and is responsible for the component curves shapes of highs in the horizontal and an inflection in the vertical.

The values K_1 and K_3 are particular constants of this system. In the absence of secondary currents they constitute the system's response. The constants K_2 and K_4 establish the conductor's response function. As depicted in Figure 7, their behavior is a function of the response parameter Q_2. The lower graph in the figure is an example plot of the phase and will be discussed in the next section.

Within eq. 3 there exist two undetermined constants: Q_2 and K_{30}. These values identify the secondary current element's conductive quality and its coupling coefficient to the primary source. There is no way to understand the complete circuits of the primary line source or the secondary current element. Nonetheless, different values for Q_2 based on the response function's behavior in conjunction with arbitrary values of K_{30} may be used to calculate model polarization curves.

III.3 Discussion of the Model's Results

In Figure 8, the details concerning the model's layout are shown. The computer program listing can be found in Appendix C under the heading of FM. Six different models numbered g1 through g6 were plotted to show varying behavior due to a

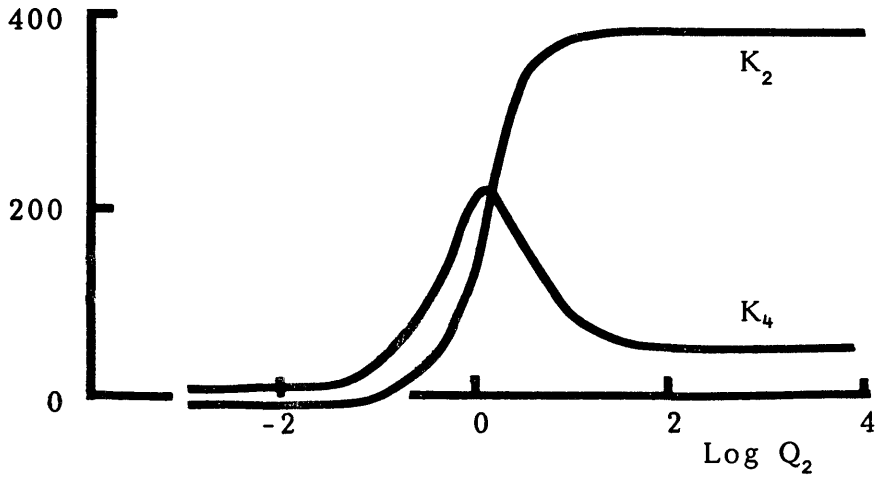

Response Function g1

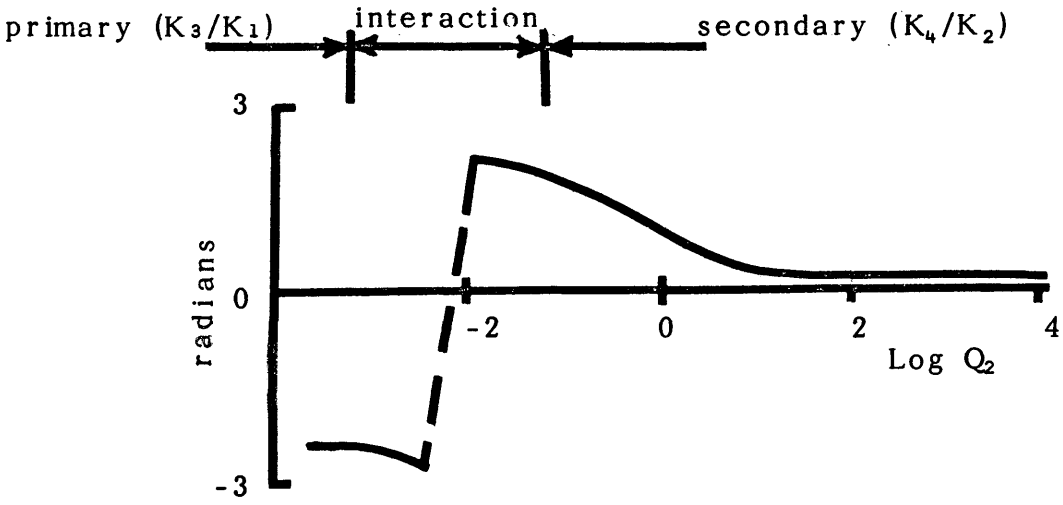

$$\text{Phase} = \text{arctangent}\left[\frac{\text{Quad}}{\text{Real}}\right] \qquad g2$$

Figure 7. The response function behavior - g1, and measured phase behavior - g2

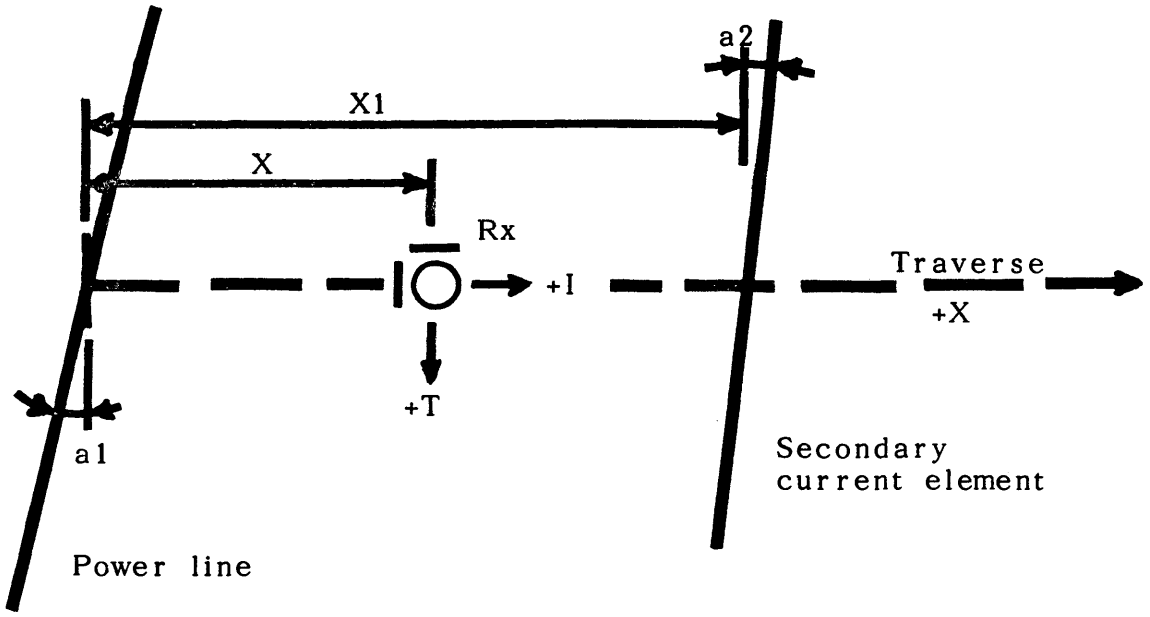

Plan View

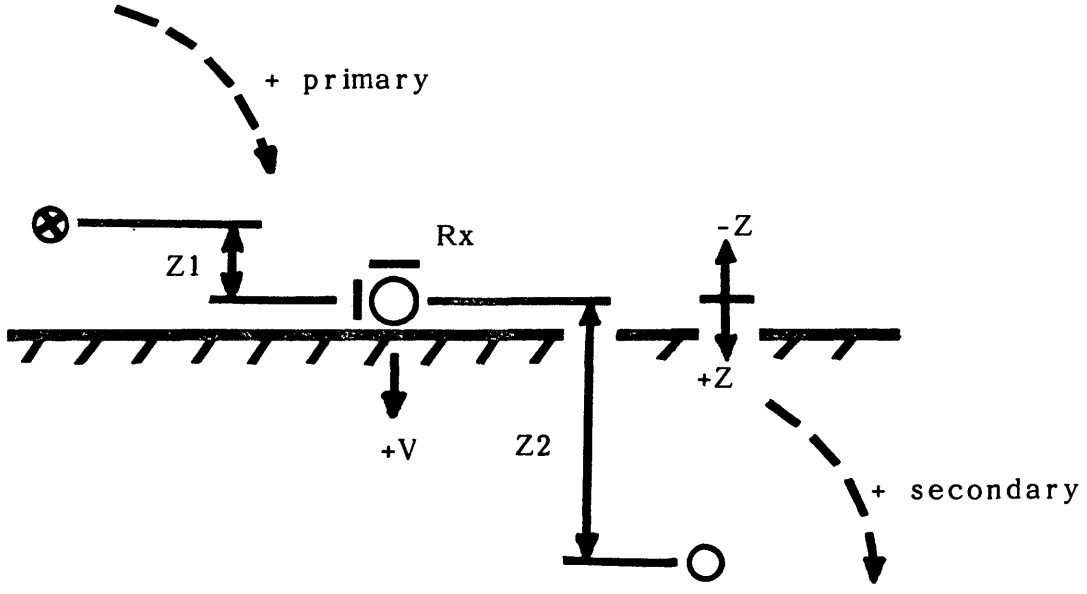

Cross-Section

Figure 8. The forward model's geometry.

single current element. It should be kept in mind that a composite of multiple current elements relates more so to the field data collected by the sixty-hertz system. As with the field data, twenty-five graphs were generated for each line. This was done because sometimes anomalies would appear in certain graphs but not in others. Due to the large number of graphs, only those of selected interest are shown here while other supporting graphs appear in Appendix D.

The units of length defining the geometry are relative values and are noted in the caption below each graph along with the other particulars describing the model. The numbers on the graphs represent the stations. They are 132 units apart, and for all cases have the anomaly located midway between stations 5 and 6.

Throughout the analysis of the models, references are made to primary and secondary field contributions. Ratios of primary to secondary fields are controlled by the constant M/L (K_{30}) and -Q (Q_2) which represent the secondary field coupling geometry and conductor quality, respectively. With regards to the forward models discussed below, certain points are labeled in order to reference and highlight graph behavior which affect polarization curve shapes. The first two points are general assessments of the geometric parameters associated with the mutual inductance terms:

1) The primary field has only a decay type affect. The more distant from source the more unform the field is.

2) The portion of the curve due to the secondary field is symmetric about the conductor. The secondary's contribution is proportional to the magnitude of the curve highs and inflections.

The highs shown in the graphs of Figure 9 typify the horizontal fields in agreement with point 2. Differences between the in-line and transverse channels are attributed to the angle formed by the traverse and secondary current directions. Underlying points to observe about the graphs are:

3) Anomaly depth correlates to the response width. For example, graph g4 in relation to g3 has the anomaly at 1/10 the depth while the width is approximately 4/10 as much.

4) In accordance with point 1, for distances to power lines more than the aspect ratio of 6000 (power line distance) to 1320 (traverse length), the primary field's change becomes insignificant.

Point 4 is illustrated by graph g3 in comparison to g6. When the M/L difference is compensated for, graph g6 has a similar response to g3 for the anomaly located 10x the distance from source. Replacing the relative length units with metres in graph g3 correlates to an anomaly 1.6km from a power line source and a traverse distance of 400m.

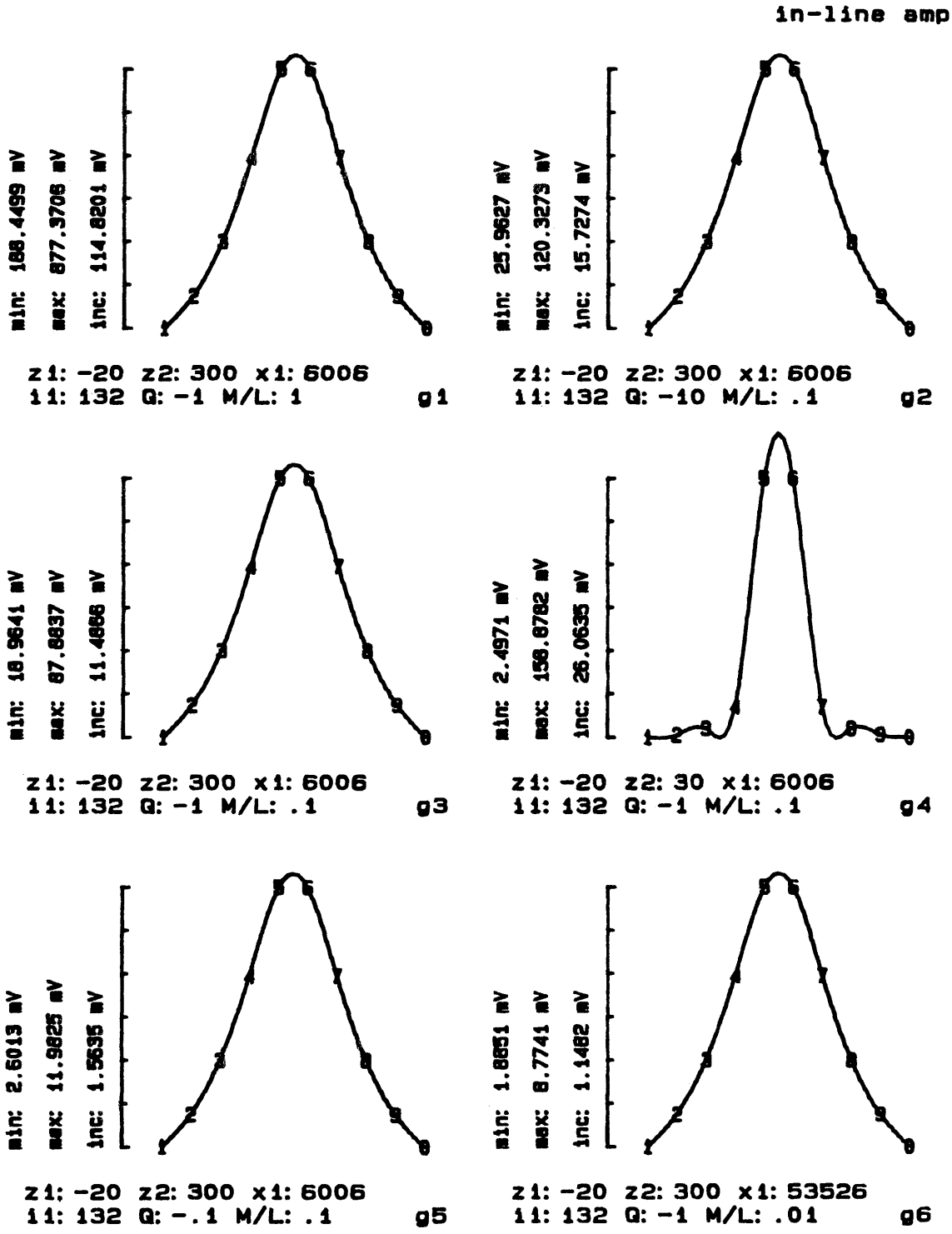

Figure 9. Forward model in-line amplitude graphs.

Although curve inflections are not shown in every graph in Figure 10, all vertical real and quadrature parts display this phenomenon with dc offsets equal to the primary field. This is a consequence of point 2. In addition, the following points can be made:

5) In the presence of good secondary signal where both real and quadrature parts have zero crossings, vertical amplitudes are highs.

6) Horizontal shifting and asymmetry in the vertical amplitude are caused by the primary field's influence on the response.

Point 6 does not contradict point 4 which pertains to an asymmetry in the horizontal fields. The phenomenon referred to in point 6 results as the vertical secondary field interacts with the vertical primary field. The anomalous curve behavior remains intact over the anomaly, but with a slight bias. It is because of the secondary field's symmetry about the anomaly that results in the above conclusion.

As illustrated in the lower graph of Figure 7, the plotted phase is for an anomaly buried 300 units down and 6000 units from the source, with M/L equal to one. Due to the response function's behavior at both ends of the scale shown, two asymptotic conditions are created. The measured phase for low values of Q_2 approaches the system's phase while the

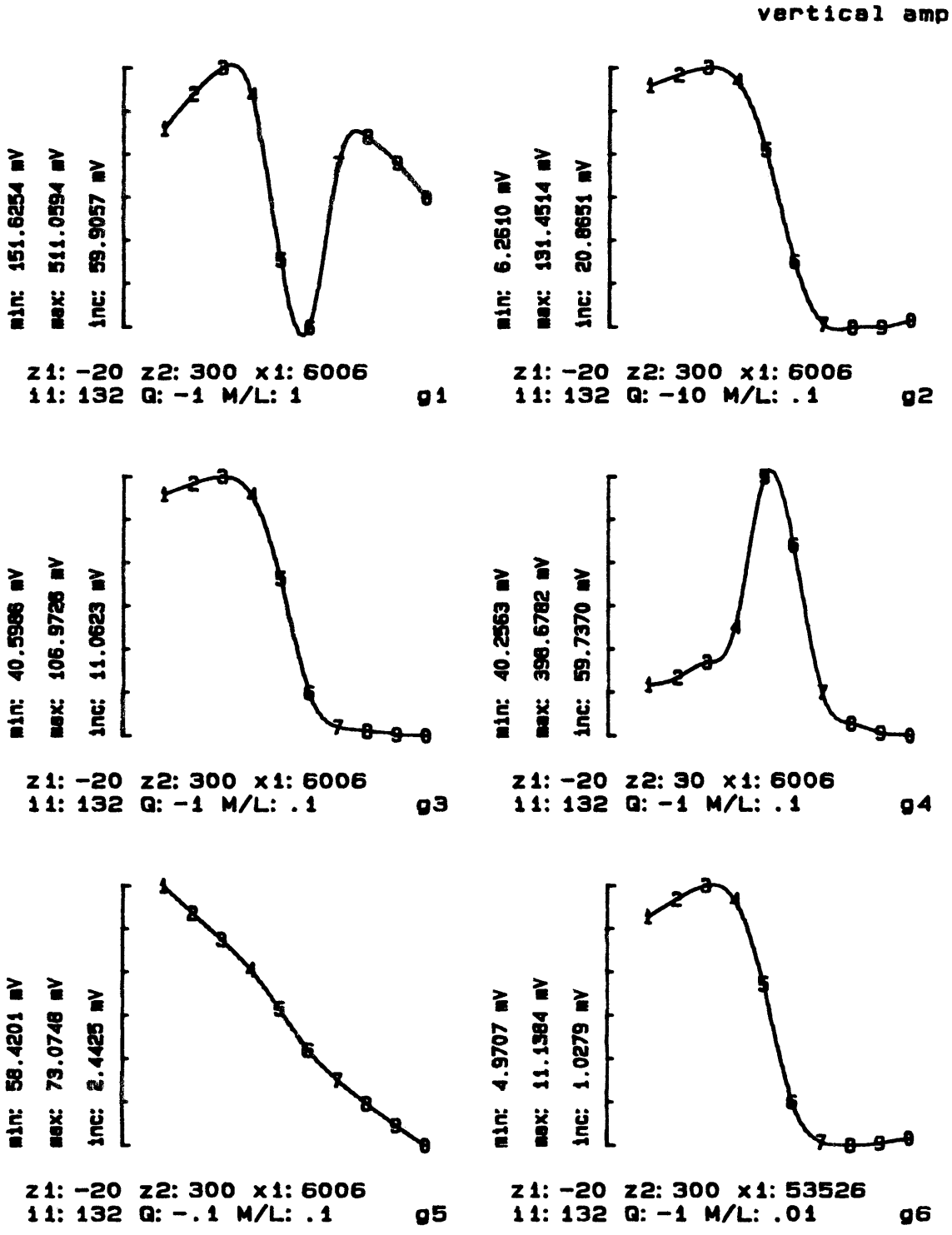

Figure 10. Forward model vertical amplitude graphs.

measured phase at large values of Q_2 approximates the conductor's phase. In the context used here, the system's phase is defined as the inverse tangent of K_3/K_1, and the conductor's phase is the inverse tangent of K_4/K_2.

In effect, the graph of Figure 7 is a plot of relative secondary to primary field contributions. From the area on the graph marked 'interaction', as Q_2 increases the more predominate the secondary signal becomes in relation to the primary field. This is illustrated by the graphs in Figure 11 and the data in Table 3. Graph g3 has relatively more primary than g2, and graph g5 has more primary than g3. This progression is noted in Table 3 by increases in the phase differences (conductor phase minus the measured phase) and follows the behavior of the graph in Figure 7. As shown in

Table 3

Phase Values (reference to Figure 11)

	peak phase	conductor phase	difference
g1:	.8855	.8557	.0002
g2:	.2104	.2105	.0001
g3:	.8540	.8557	.0017
g4:	.8548	.8557	.0009
g5:	1.4877	1.5050	.0173
g6:	.8555	.8557	.0002

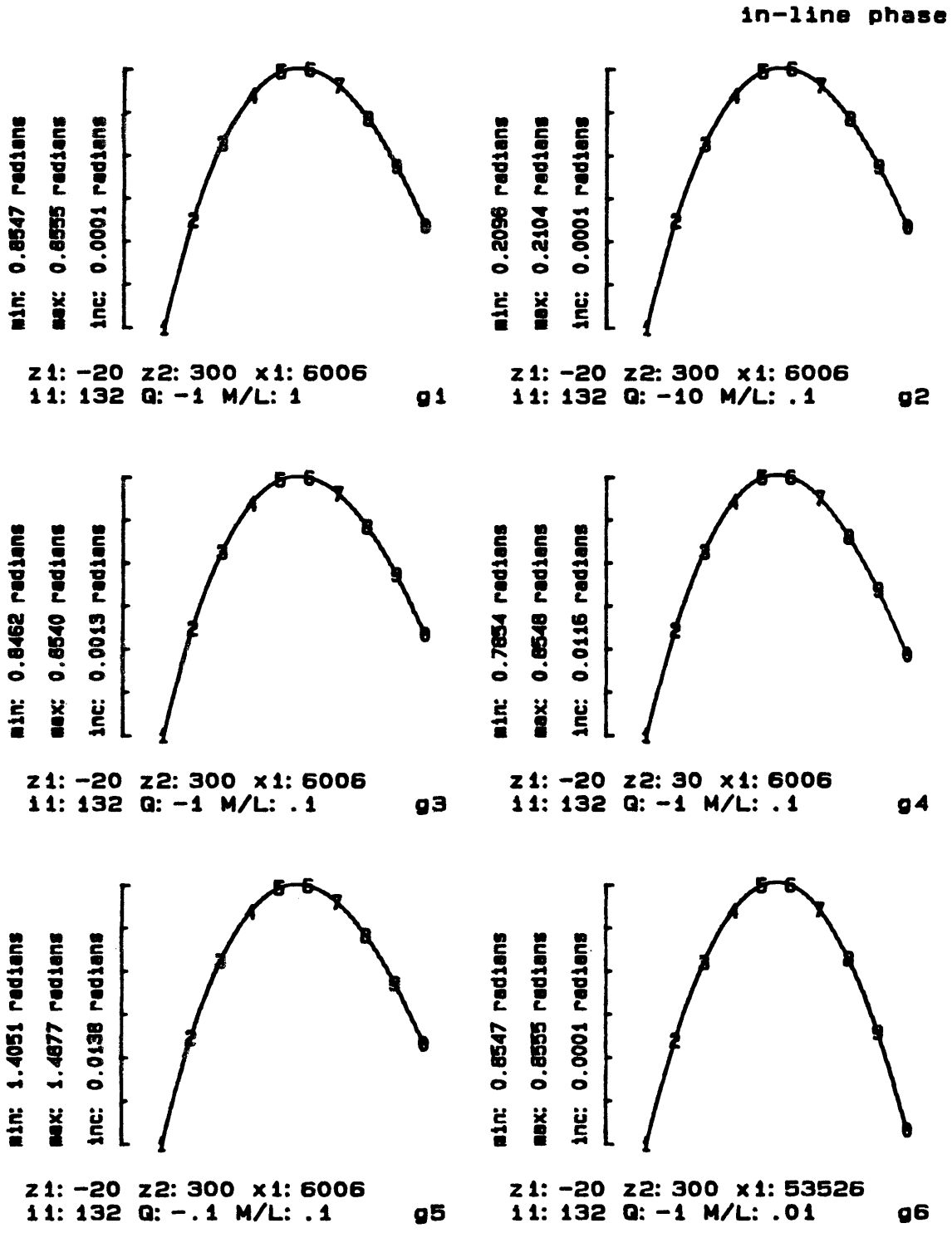

Figure 11. Forward model in-line phase graphs.

Figure 12 graph g2, there is a shift of of the zero crossing in the vertical phase which is due to dc offsetting in the curve of the quadrature part. The increased Q_2 causes a decreased quadrature value which increases the primary's contribution resulting in the asymmetry. Due to changes of Q_2, the secondary field's contribution changes relative to the primary field. This represents one cause of how the measured phase may vary.

For the horizontal fields, the peak values attained over the anomaly are the closest approximation of the conductor's phase. This is due to optimum coupling at that point. Effect of the secondary field coupling on the vertical phase can be seen in the zero crossings. As shown for graphs g2 and g4, the primary field has greater influence on the side of the anomaly closest to the source. This accounts for the smoother graph behavior on that side in comparison to the far side. On the far side the effect of the secondary field is relatively stronger and exhibits a better approximation of the conductor's phase. These examples show a second cause of varying phase which is related to changes in the mutual inductance. The following point sums the above as:

7) The validity of phase measurements representing the conductor's quality depends upon the relative contribution of the secondary field. The greater the secondary field

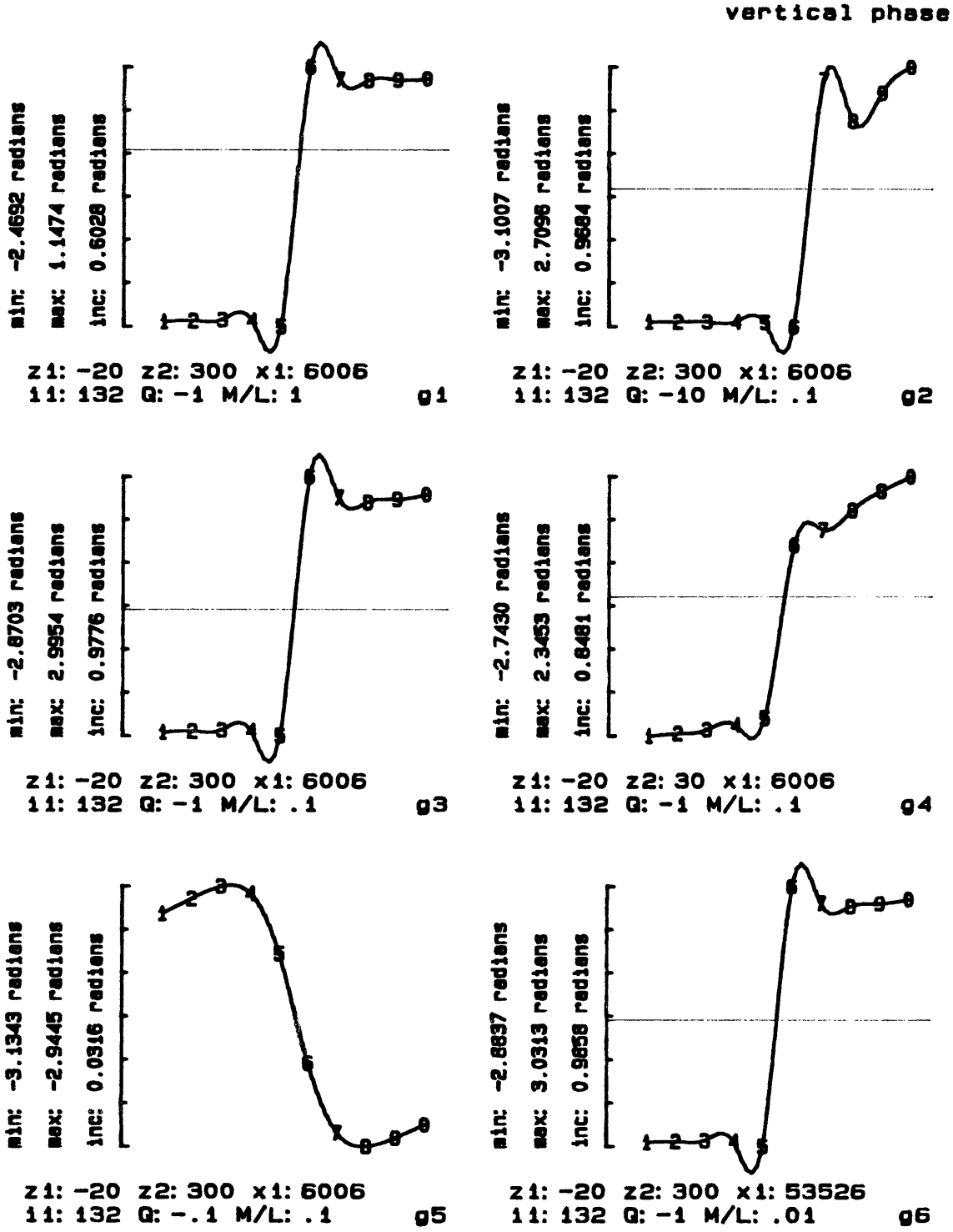

Figure 12. Forward model vertical phase graphs.

contribution the better the measured phase approximates the conductor's phase.

The phases stated above relate to an unknown primary source. Measured absolute values are rendered useless until viewed in comparison with another phase. For this reason calculation of polarization relies upon phase differences between two channels which removes the primary's dependence but not its influence. This interaction is manifested in the following ways. Because the conductor's phase is constant, the primary field's influence correlates to a variance of the phase. Therefore, the curve of the component with the greater primary influence will dominate the curve shape of the phase change. This is seen in the horizontal phase change. The transverse phase has more primary field influence than the in-line due to the poor coupling angle of the receiver. Thus, the curve shape of the horizontal phase change is similar to the transverse phase. Because the vertical component has the most influence of the primary field, its curve shape dominates the vertical phase change.

Amplitude ratios express the same interactive behavior between secondary and primary fields as seen in the phase. For the model's case where the horizontal field has a major contribution by the secondary current element, the horizontal amplitude ratios approximate the tangent of the angle between the traverse and the current element's azimuth. This is due to

the same coupling dependance for real and quadrature parts except for different trigonometric coefficients. For the models the coefficients differ by a factor of ten, and this factor approximates the values of the curves observed in Figure 13. The graphs in the figure show the identical shapes as seen in the phase graphs: both are ratios of sums of primary and secondary fields. Thus, as a corrollary to point 7:

8) The greater the secondary field influence, the closer the hoizontal amplitude ratio approximates the tangent of the angle between the traverse and conductor's azimuth.

Vertical to horizontal amplitude ratios show predominant asymmetric lows in the curves. The asymmetry is a consequence of points 4 and 6 above.

Tilt and ellipticity are polarization functions dependent on the interaction of an amplitude ratio and phase change. For instance, horizontal curve highs in amplitude ratio and phase change pass this character to the horizontal polarization curves. Three sets of polarization defined by in-line per transverse (i/t), vertical per transverse, (v/t), and vertical per in-line (v/i) were calculated. All vertical per horizontal sets have similar amplitude ratio curves and similar phase change curves. However, interactions of these amplitude ratios and phase changes show more complicated behavior that tend to vary the profile shapes. Nonetheless, tilt and ellipticity

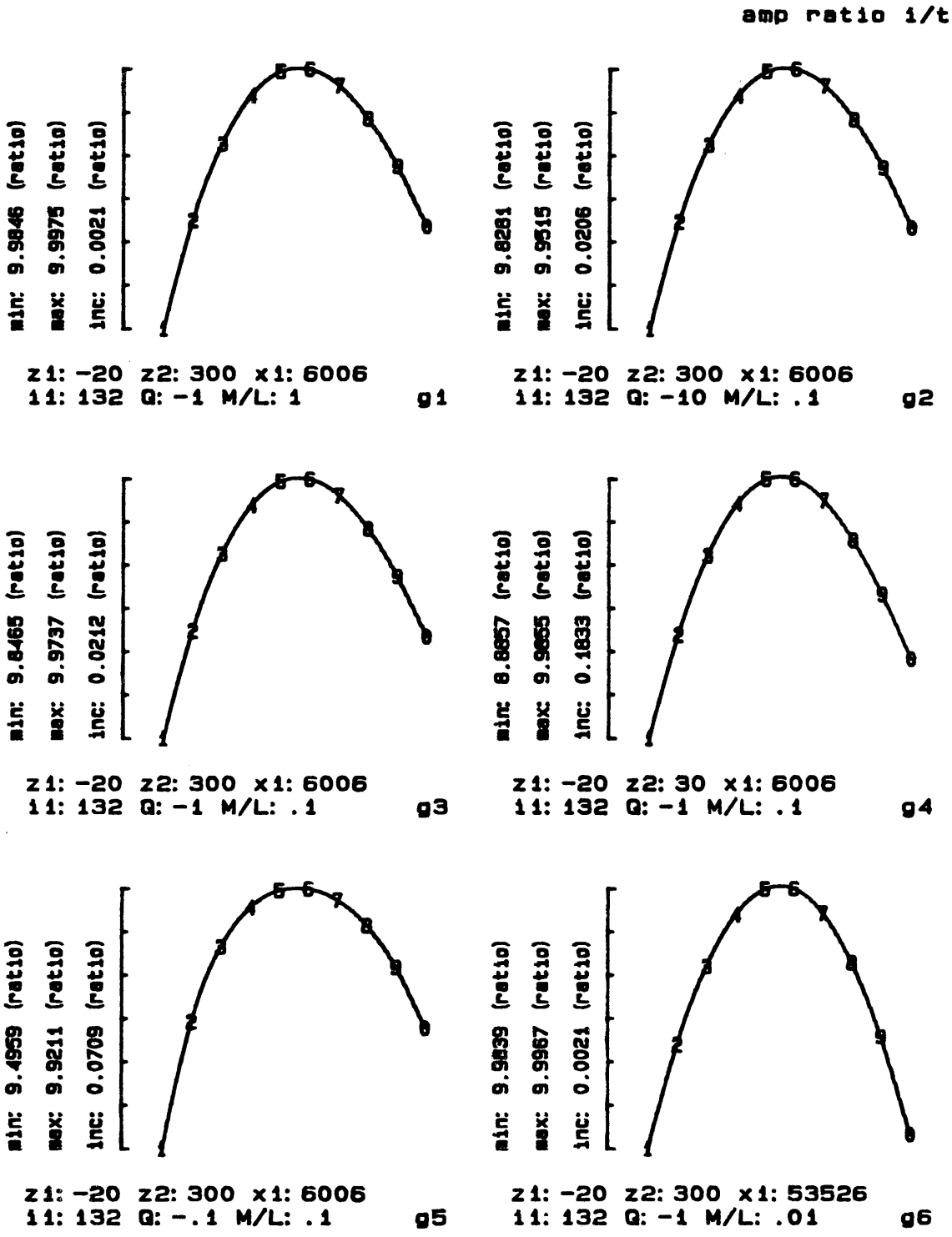

Figure 13. Forward model amplitude ratio graphs i/t.

plots identify anomalous field behavior.

Figure 14 presents graphs of the vertical polarization tilt as asymmetric highs and cross-overs. Horizontal shifting is seen in Figure 14 graph g2, and a shift in the opposite direction for the complementary polarization tilt shown in Figure 15 graph g2. In the same figure, graphs g1 and g3 display a third type of curve behavior, the shoulder type of response. Graphs of polarization ellipticity in Figure 16 display various distorted curve lows. In part they resemble the amplitude ratio curves, but inverted with more asymmetry. As noted in point 6, the vertical primary field influence is responsible for the asymmetry which, in general, seems to be responsible for the distorted polarization curve shapes.

III.4 Multiple Sources

As mentioned earlier, using AMT apparent resistivities assisted in calculating the sixty-hertz system sensitivity. From those results it is seen that a 1 mV reading correlates to approximately .8γ. The Kassler line shows typical voltage readings for the horizontal field which relate to a magnetic intensity in the range of .4γ to 13.6γ. At station 5 the AMT for 45 and 75 Hz showed a background magnetic intensity level as .5γ and .8γ, respectively. Recorded spikes in the record were approximately 2γ. Based on these values, EM fields due to sferics can have a considerable contribution to

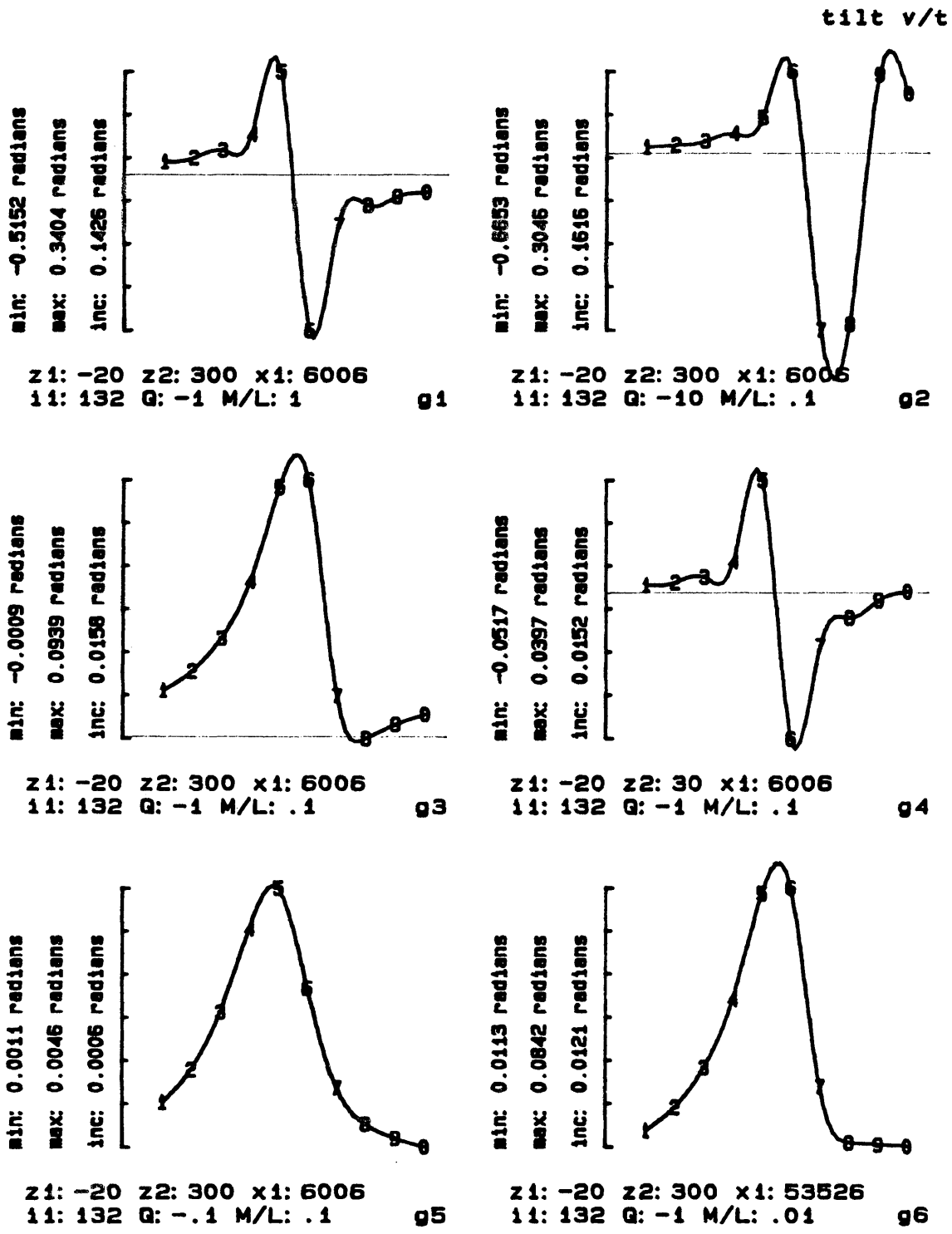

Figure 14. Forward model polarization tilt angle graphs v/t.

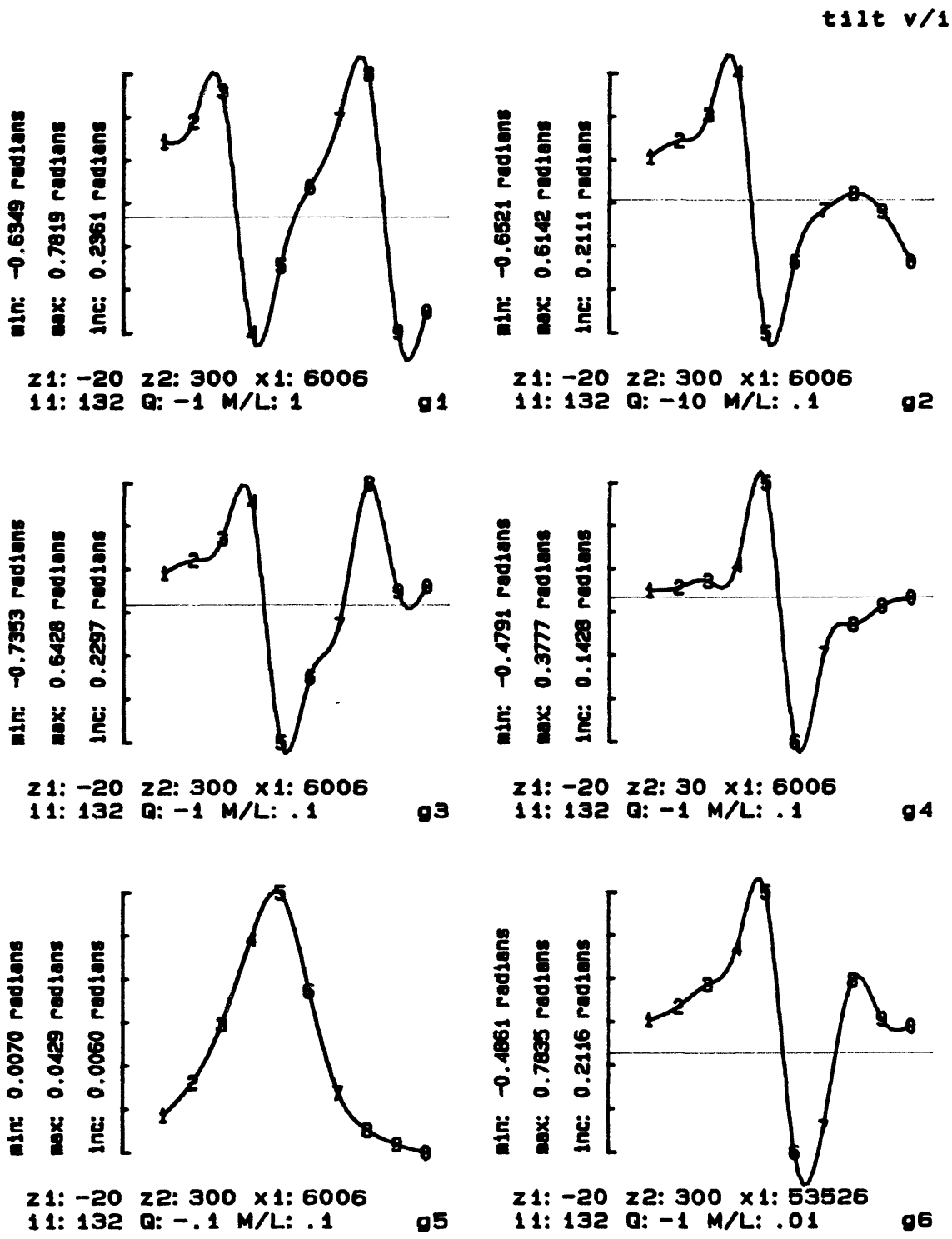

Figure 15. Forward model polarization tilt angle graphs v/i.

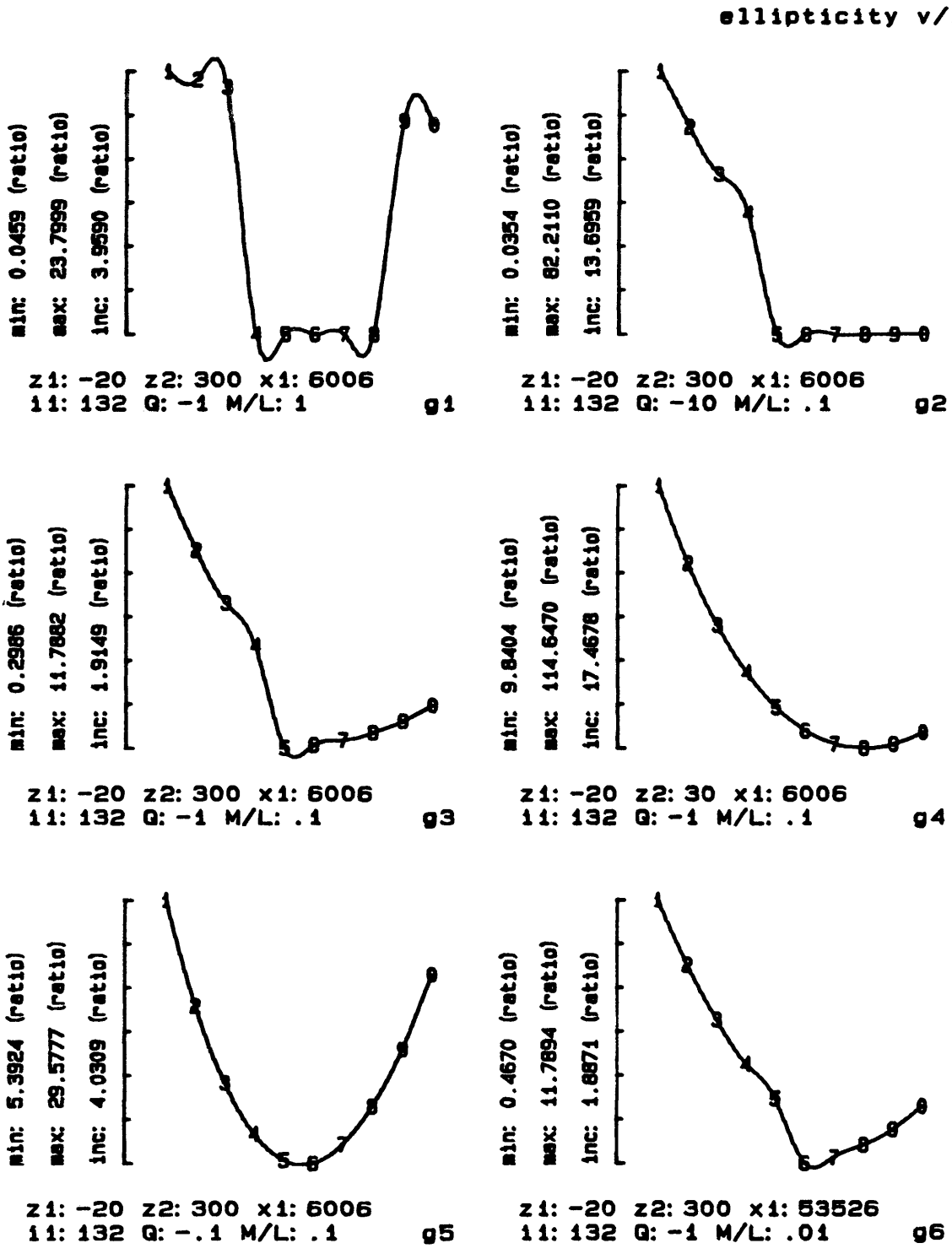

Figure 16. Forward model polarization ellipticity graphs v/i.

the measured 60 Hz signal.

Therefore, expanding the single current element model into to a more realistic model based on multiple sources adds the presence of a horizontal primary field. The resulting equation would be the same as the one used above. The difference is the additional coupling due to the horizontal primary field which would be accounted for in the mutual inductance term. The numerical effect is a dc offset in the horizontal components as already seen for the vertical. Also, different amplitudes would exist for each of the three channels. This would result in noisy polarization values when in the presense of varying fields such as sferics. Although adding complexity to the curves, conductive contrast would still be evident, but in a more subdued fashion.

IV. DISCUSSION OF FIELD DATA RESULTS

Field testing the sixty-hertz system was done over a variety of different anomalies that were expected to give an adequate EM response. In theory, profiles across lateral inhomogeneities create anomalous field behavior that simulates secondary current elements buried beneath the earth's surface. The larger the conductive contrast or shallower the depth, the more likelihood there is of detecting the anomaly. Because of multiple source directions, occurrences of E-polarization are common. Therefore, selecting sites for any of the three targets were based on road access and power line locations.

The map in Figure 17 shows the eleven test site locations. They are classified into three general groups. The first, the plains to the east of Denver, has horizontal subsurface geologic structure where buried pipes were targeted. Also observed were various effects due to cultural noise. The second group was in mountainous regions which are more prone to faulting and to isolation from power lines. Increases in porosity accompanied by the presence of water tend to make faults more conductive than their suroundings. At the third location which lies in a transition zone between the previous two physiographic provinces, profiles were recorded over geologic contacts of sediments turned on edge exposing layers of differing conductivity.

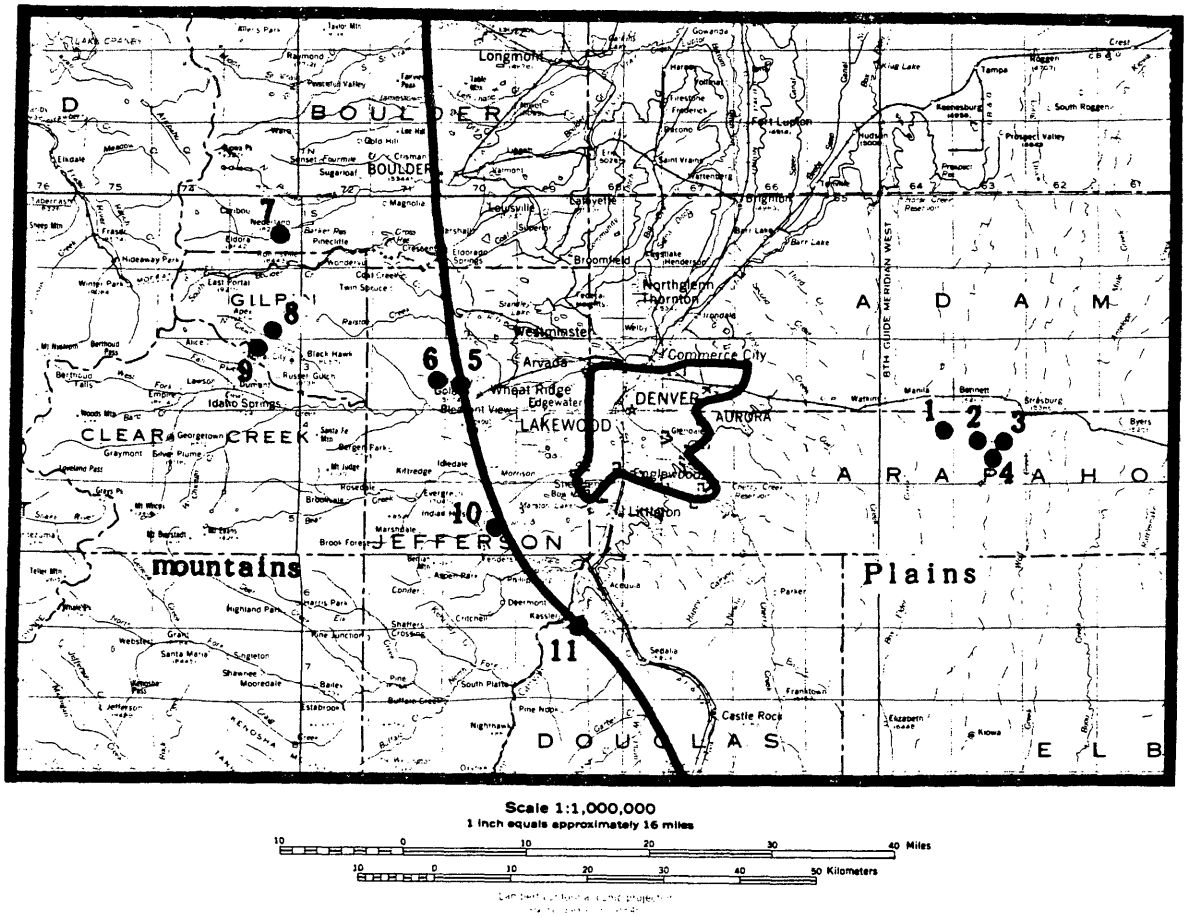

Site title

1 - Watkin line 1
2 - Bennett line 1
3 - Bennett line 4
4 - Bennett line 5
5 - Golden line 1
6 - Golden line 2
7 - Nederland line 1
8 - Central City line 1
9 - Central City line 3
10 - Indian Hills line 1
11 - Kassler lines

Figure 17. Area map of test sites.

Due to the many graphs generated by the field data, only three sets of tilt and ellipticity graphs representing the groups noted above, are presented here. Additional profiles that support remarks made in the text can be found in Appendix D.

IV.1 Field Procedures

The equipment was adapted for ground use by packing the various electronic components into a protective container. Two 12 volt gel-cells feeding into DC-DC converters provided the power supply while the computer operated on its own batteries. Although limited by the power consumption of the printer, a full charge would last a day.

Stations were located by odometer readings from the field vehicle. At each station the probe mounted on a tripod attached to an eight metre line was put out and leveled with a constant orientation relative to the vehicle. Effects due to the truck were derived from the graphs D1 and D2 in Appendix D, and are

Table 4

Truck Effects

	tilt			ellipticity		
	truck	max truck	K3	truck	max truck	K3
i/t:	.1	.064	1.2	.16	.04	11.8
v/t:	.5	.05	1.1	.37	.5	1.6
v/i:	.01	.04	1.2	.12	10.5	4.2

tabulated in Table 4. The column entitled 'truck' is file K1 taken on the Kassler line 2 at station 13. The values show a polarization change as the truck moved from 8m to 60m away from the probe. The column entitled 'max truck' is file C4 taken at station 17 of Central City line 3. Here, the probe was placed at different horizontal angles around the truck in order to observe probe orientation effects. The values are the maximum polarization change between two stations which represent a 45 degree difference in the probe's position. These values are compared to the anomalous response on Kassler line 3 (file K3). Clearly, the truck has a measurable response, but it is constant and somewhat less than the anomaly's.

Once set up, the computer program sampled two readings, calculated the polarization values, and printed them out. If the two measurements were comparable, the last reading was stored. Otherwise, another set of readings were taken. At the end of the line the readings were stored on magnetic tape while the printer generated character plots of the data. This enabled a quick on-site analysis of the line while providing a hard copy of the work. One person can perform the survey, and stations take about five minutes each.

IV.2 Buried Pipes and Cultural Effects

Figure 18 outlines the location of Bennett line 5. Several features along this traverse show typical noise related to

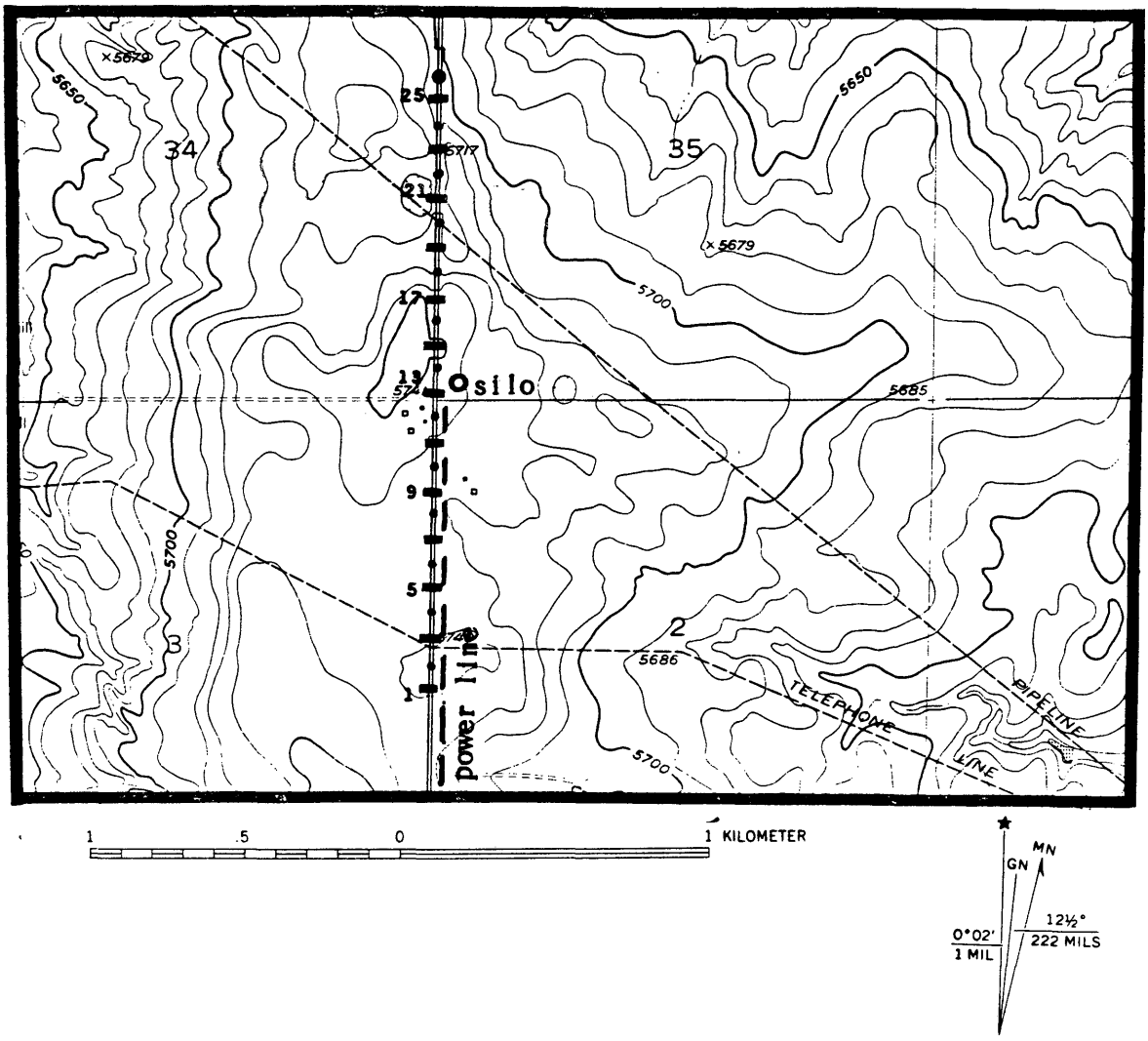

U.S.G.S. Strausburg NW Quadrangle;
T4S, R63W, sections 34,35
T5S, R63W, sections 2,3
Colorado Interstate Gas Pipeline
Sensor probe orientation: due south

Figure 18. Detail map of Bennett line 5.

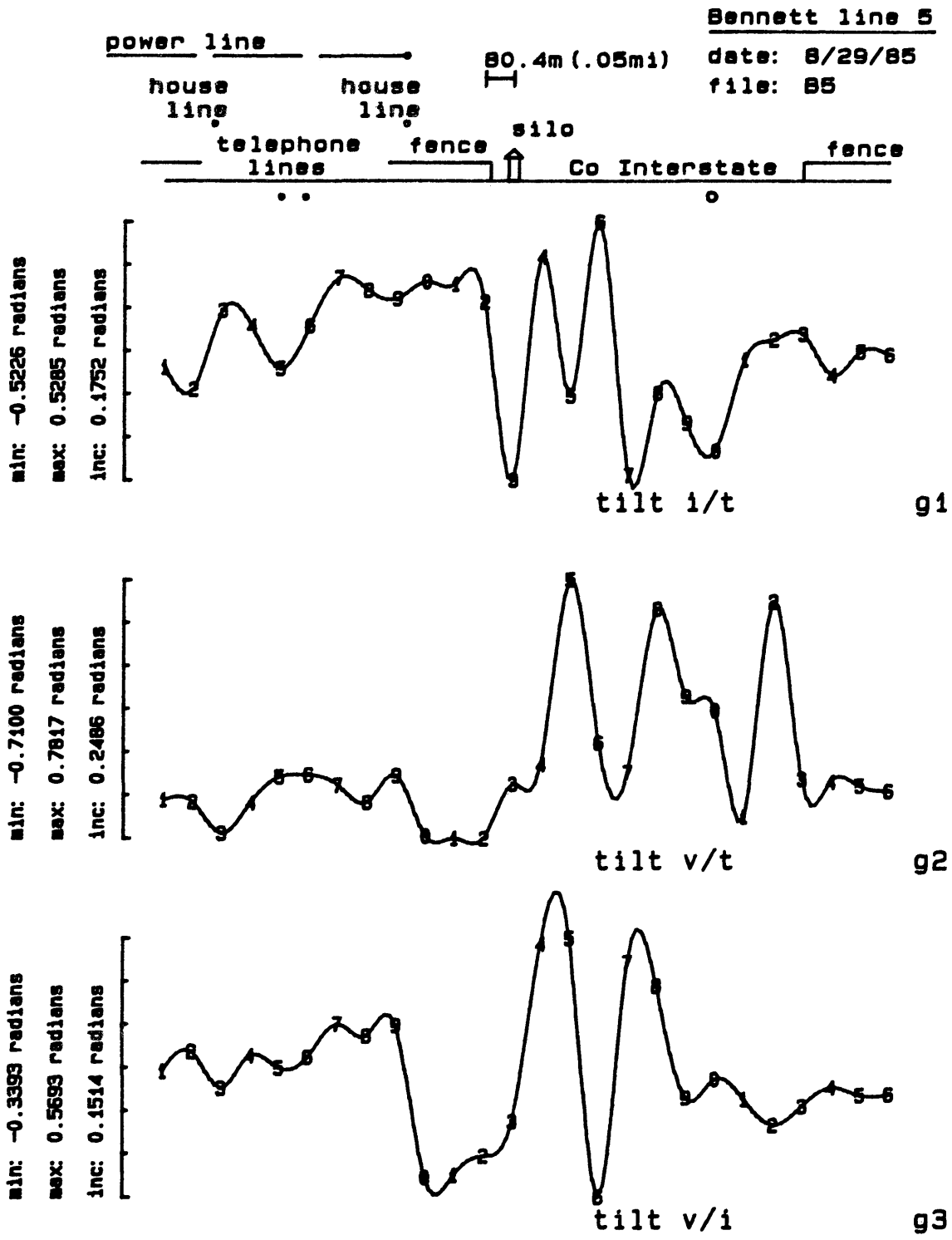

Figure 19. Bennett line 5 polarization tilt angles.

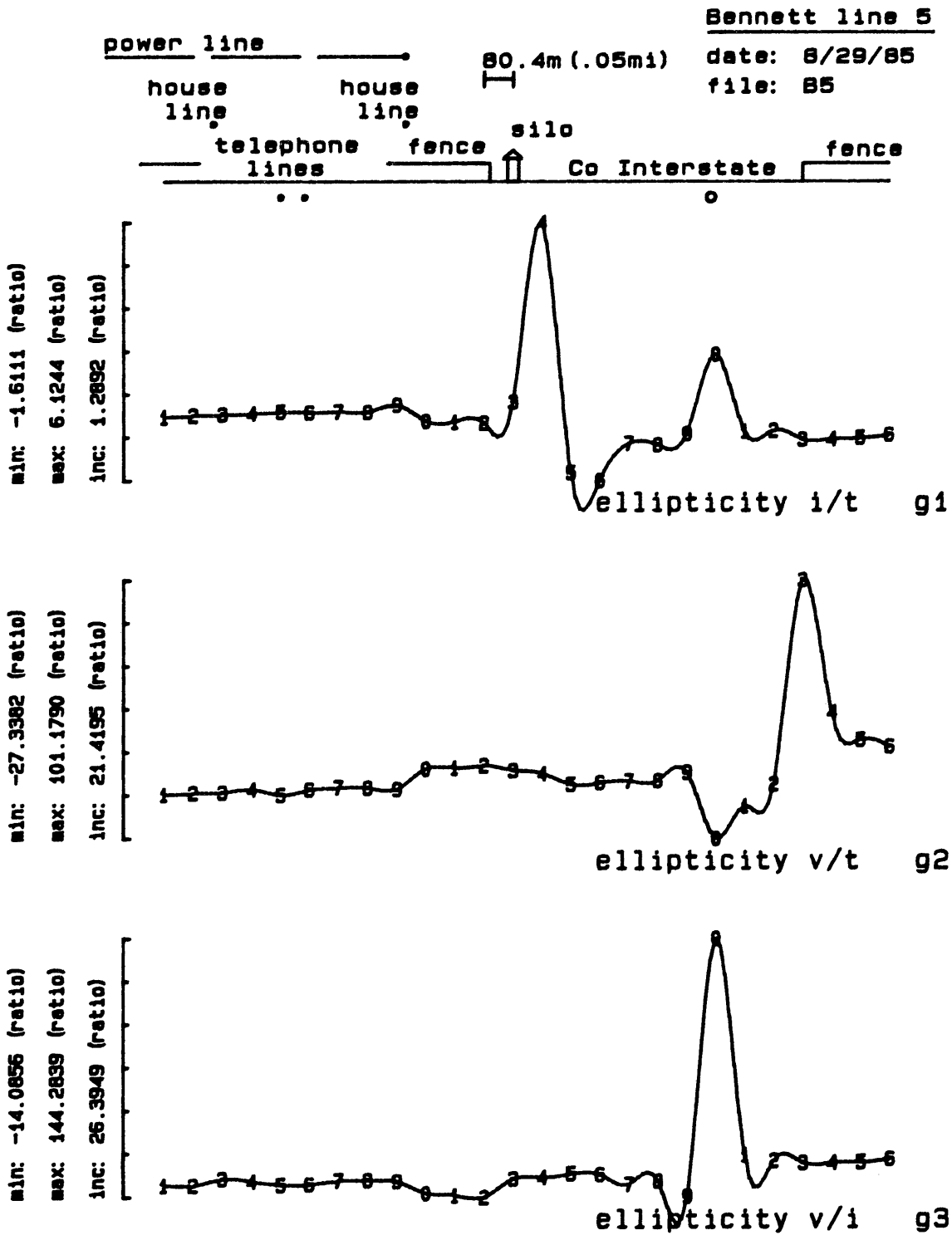

Figure 20. Bennett line 5 polarization ellipticities.

culture surrounding the targeted pipe. Colorado Interstate Gas Company, who operates this pipeline, provided the following information typical of pipelines in the area. The 50.8 cm (20 in) diameter steel pipe is buried approximately one metre below the surface, insulated with tar, and wrapped in tape. On this line there are two pipes located 7.6m apart. A full rectified 60 Hz signal feeds into the pipe for cathodic protection. The importance of this signal in relation to the response is not very well understood because over an Amoco pipe on Bennett line 4, which has a filtered wave input, an excellent response was acquired. This particular pipe on Bennett line 5 was constructed in the 1950's and may be more prone to electrical contact with the ground as a result of a deteriorating insulating cover.

Figures 19 and 20 present data results for the pipes and show a more distinctive response in the ellipticity than in the tilt. In Table 5, comparison of anomalous graph behavior due to various pipes indicates a more intense vertical than horizontal polarization. Horizontal polarization responds better to lateral surface features such as that evident from the metal silo at station 13 or the metal drums on the Central City line 1 (Appendix D, D24).

Curve highs represent the most general graph behavior; however, shoulder type curves also appear. Correlating to

Table 5

Pipe Responses

	tilt			ellipticity		
	i/t	v/t	v/i	i/t	v/t	v/i
W20:	-	1.3	1.3	-	6.4	6.4
B1:	.1	.2	.1	-	560	10
B4:	.7	1.5	.1	4.2	18	119
B5:	.3	1.2	-	2.5	21	158

graphs g1 and g3 of the forward model in Figure 14, shoulder type shapes emerge in graphs of tilt for the Watkins line 1, Bennett line 4 (Appendix D, D10, D17) and Bennett line 5 (Figure 19).

Inflection type graphs also occur in the data because of the vertical secondary field contribution. In the polarization curves, the stronger the anomalous field the more definite the plus and minus side lobes appear in conjunction with a zero crossing. Bennett line 4, as seen in Appendix D graph g3 of D17 and D18, displays this quality in an excellant response. With increasing primary field contribution the side lobes become less pronounced resulting in a split type of curve shape. This type of behavior is seen at station 9 (Figures 19 and 20) where an overhead house line and termination of the power line coincide.

An interesting feature of the sixty-hertz system is its ability to function in the vicinity of power lines. Power line effects cause definite curve highs in all the graphs while other cultural noise such as that seen in house lines above create subtle distractions. Nonetheless, their presence is a known factor, and the effects are easily compensated for.

IV.3 Mountain Faults

Four profiles were recorded over mountain faults zones. The general response was poor with highly variable data, especially when directly over the faults. As stated in section III.4, this is likely to occur due to multiple source directions. Because of the high resistivity and complexly folded rocks, linear current behavior within the earth is less pronounced in the mountains than in the plains.

As seen in Table 6, the anomalous responses due to faults are weak. From the four data sets, the Golden line 2 located on the map shown in Figure 21 displayed the best response. Refering to the ellipticity graph g3 Figure 23, the fault at station 9 causes a split type response. To a lesser extent the same behavior occurs in the polarization tilt graphs g1 and g2 in Figure 22. It is not uncommon in the data to see good and poor signitures of the same anomaly, such as the tilt and ellipticity responses as viewed in graphs g3. Graph g1 and g3 of Figure 24 are further examples of this.

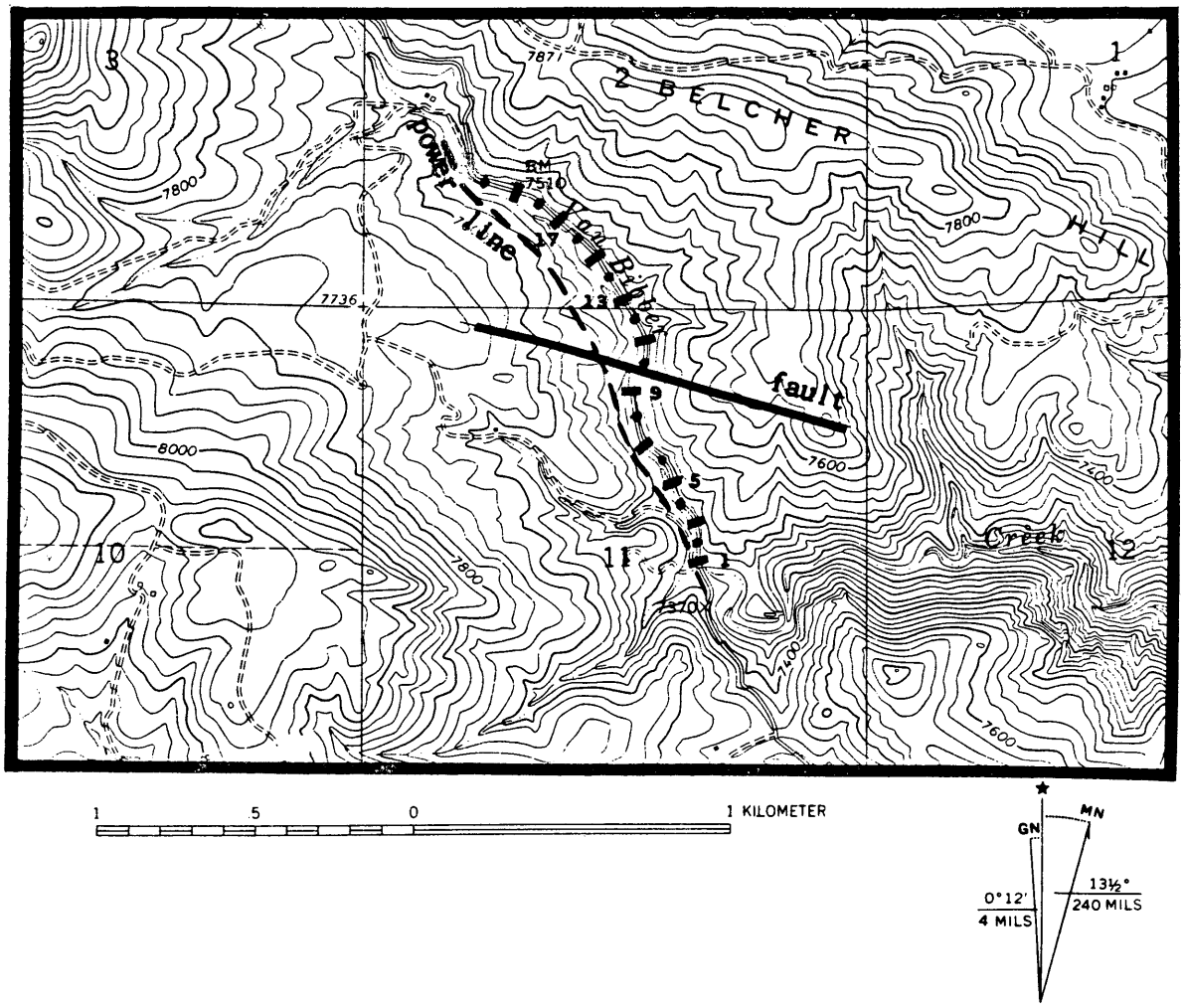

U.S.G.S. Ralston Buttes Quadrangle;
T3S, R71W, sections 2,11
Geologic reference: U.S.G.S. prof. paper 520
mica schist unit, well foliated
Hurricane Hill Fault;
strike: N 74° W
Sensor probe orientation: S 70° E

Figure 21. Detail map of Golden line 2.

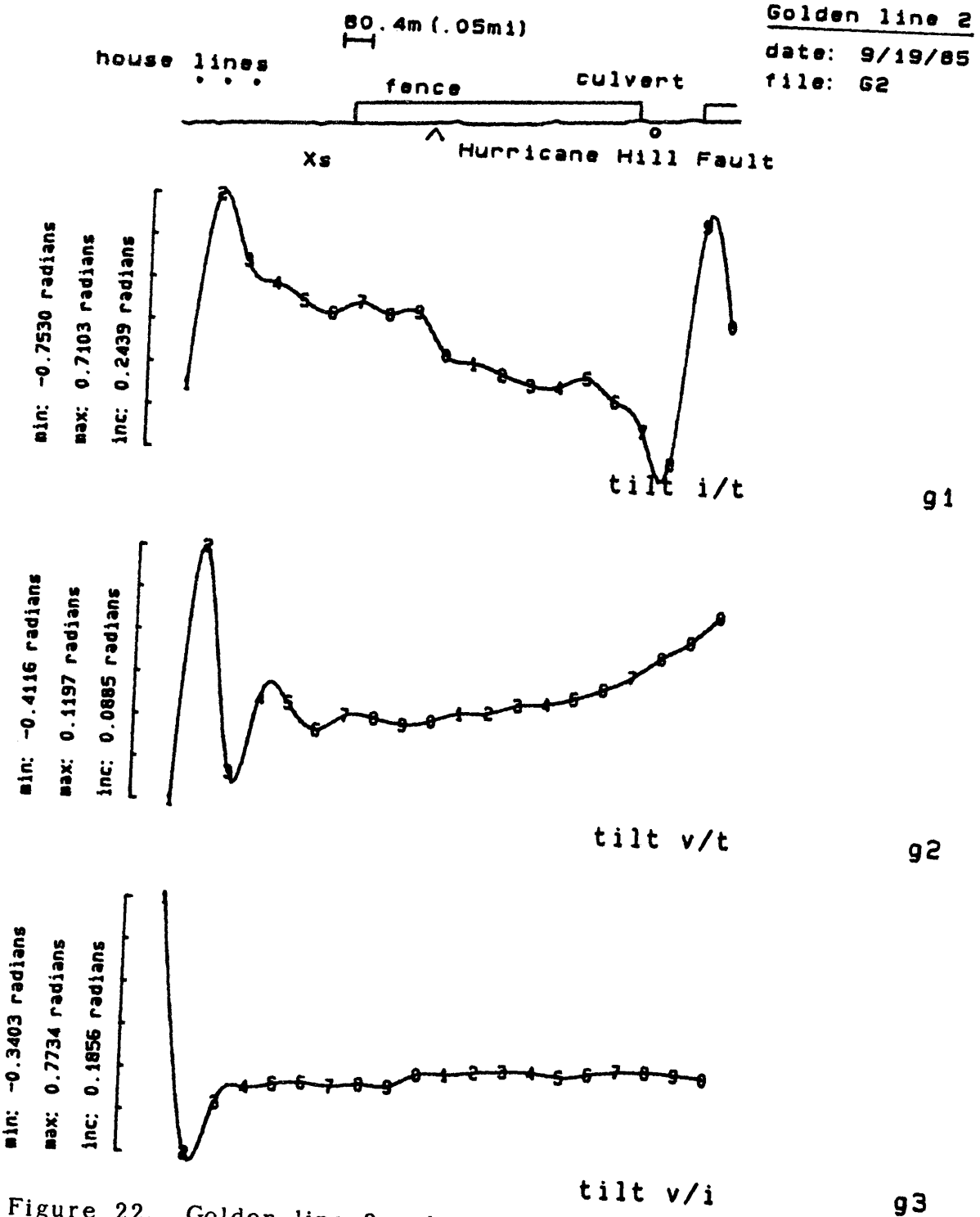

Figure 22. Golden line 2 polarization tilt angles.

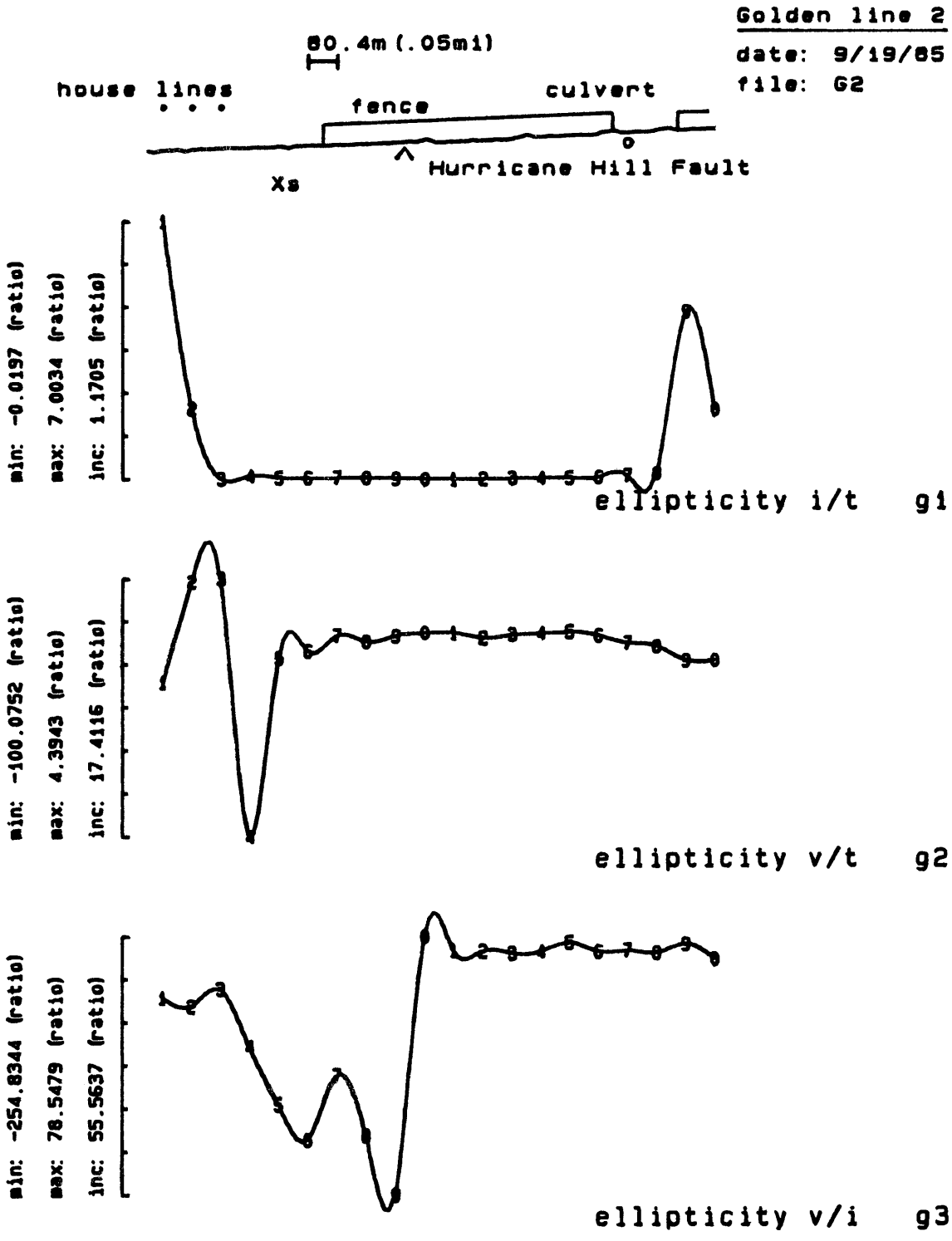

Figure 23. Golden line 2 polarization ellipticities.

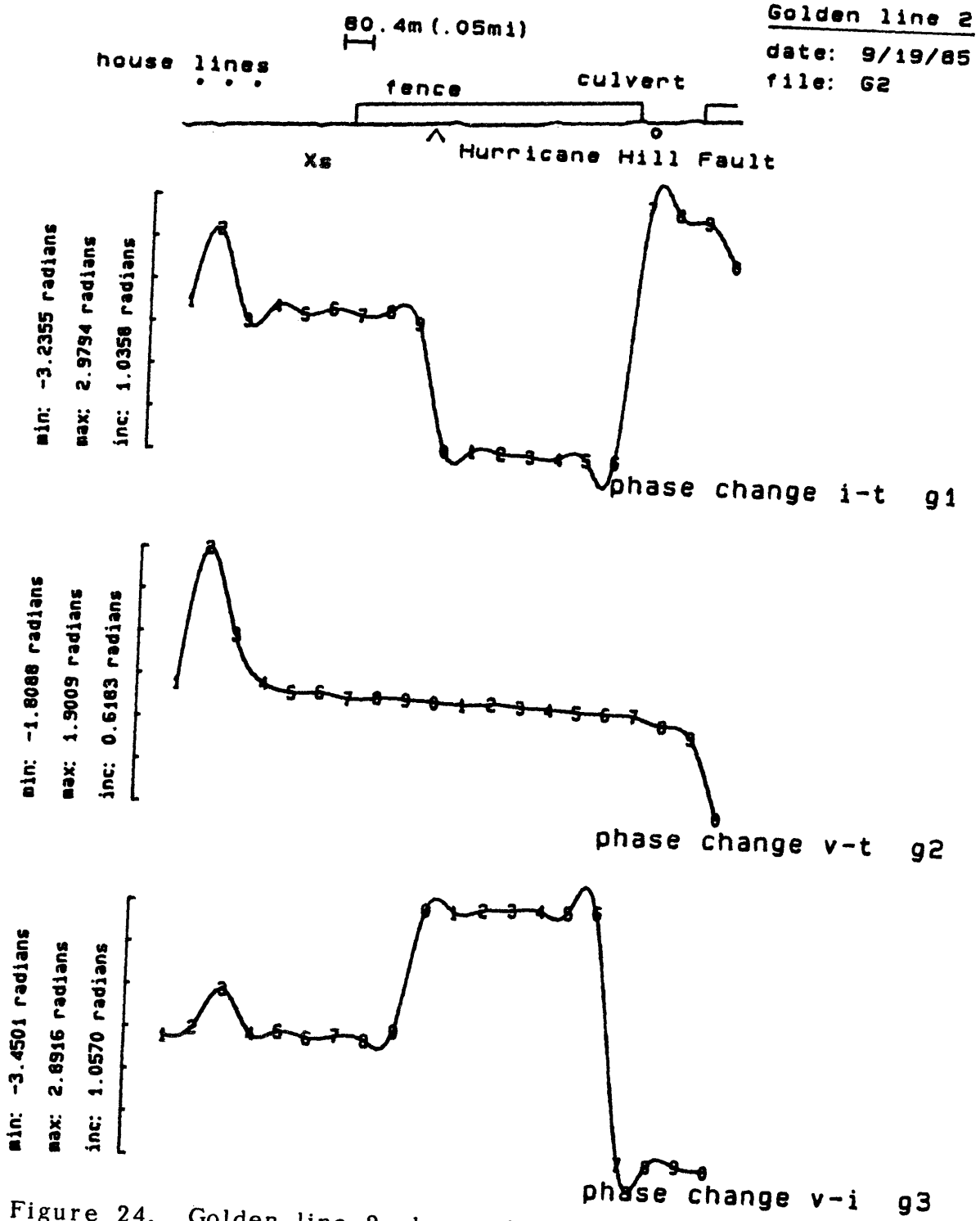

Figure 24. Golden line 2 phase changes.

Table 6

Fault Responses

	tilt			ellipticity		
	i/t	v/t	v/i	i/t	v/t	v/i
G2:	.3	-	.05	-	-	330
N1:	1.3	.1	-	2	noise	-
C1:	1.5	1.2	-	2.1	1	-
C3:	noise	noise	noise	noise	1	130

Phase change due to the culvert is larger than the phase change that occurred near the house lines. This also happened in Bennett line 1 (Appendix D, graph D13). The curve's split type behavior near the culvert is a consequence of the in-line phase. As shown by the forward model in Figure 12, this would be expected of the vertical phase, but not the in-line.

IV.4 Geological Contacts

Between the Rocky Mountain Front Range and the Great Plains there exists an area of numerous geologic contacts where the sediments of the plains have been turned up and exposed on edge due to uplifting of the mountains and subsequent erosion. These exposed formations have a general character that can be observed along all parts of the foothills. For example, the geologic cross sections for Golden line 1 and the Kassler lines appear the same. This accounts for the similar EM responses

received in both areas.

Signals were less erratic over the sediments in comparison to the mountains. This was noticeable on the Indian Hills line 1 while acquiring data across the different structures.

The location of the Kassler lines are shown on Figure 25. Line 3 is a repeat of line 2's stations 6 through 12 with additional stations taken midway. Polarization curves in Figures 26 and 27 shows the original and overlapping data which demonstrates good repeatability. The data given in Table 7 compares the responses of the Kassler and Golden lines (Appendix D, D28, D29 and D30) over the contact associated with the Ralston Creek Formation (Jrc).

Table 7

Contact Responses

	tilt			ellipticity		
	i/t	v/t	v/i	i/t	v/t	v/i
G1:	.1	.4	1.4	.03	.1	12
K3:	.1	1.1	1.3	6.5	1.6	4

AMT data at 45 and 75 Hz (Figure 28) obtained over the Kassler line 3 gives an indication of the various apparent resistivities. The east-west (EW) E-field line crosses the

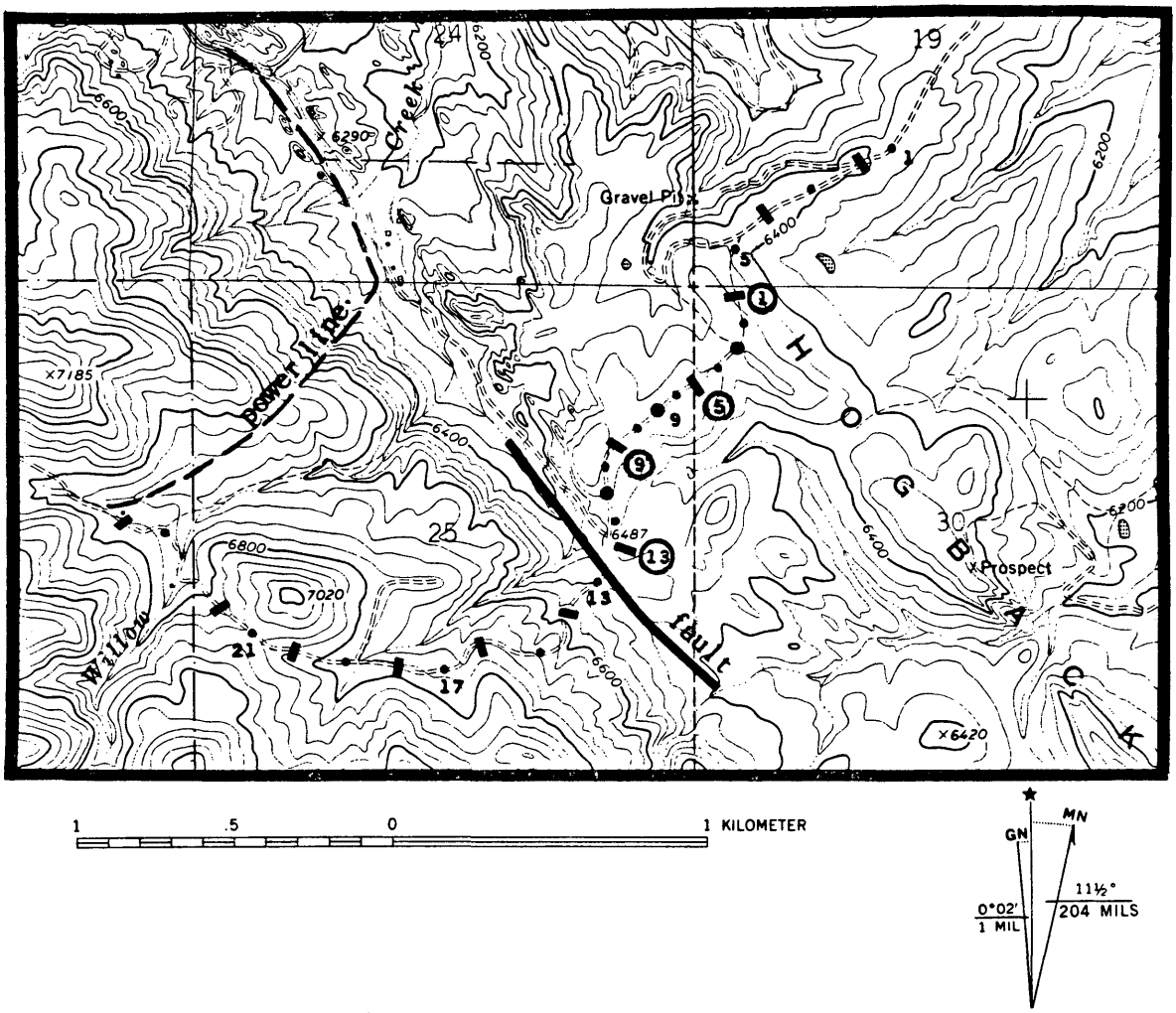

U.S.G.S. Kassler Quadrangle;
T7S, R68W, sections 19,30 and T7S, R69W, sections 25,25
Geologic reference: U.S.G.S. Denver 1° x 2° quadrangle, I-1163
Perry Fault; strike N 45° W
Kassler line 2; stations 1–24
Kassler line 3; stations ① - ⑬
AMT and VLF profiles
Sensor probe orientation: N 45° E

Figure 25. Detail map of Kassler lines.

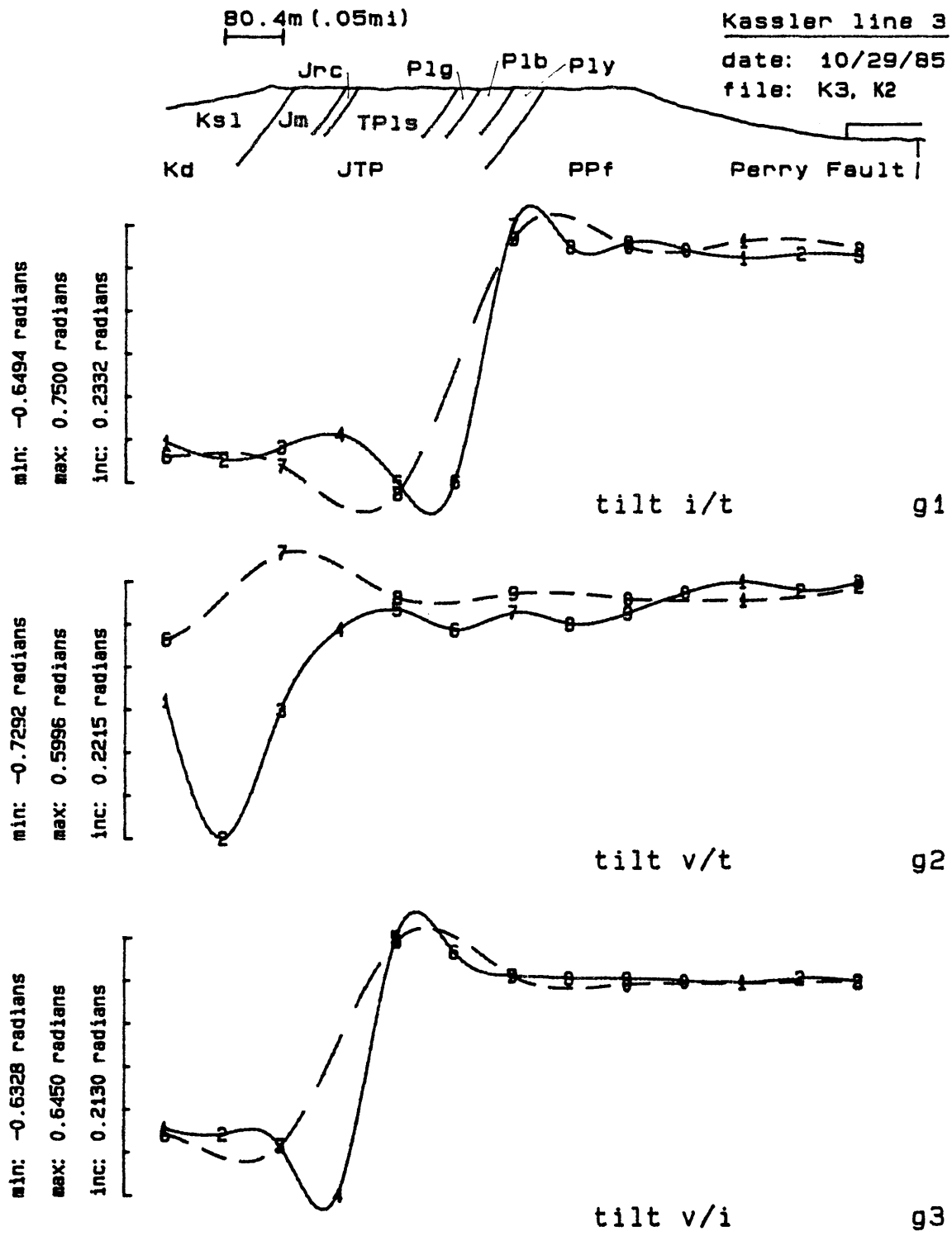

Figure 26. Kassler line 3 polarization tilt angles.

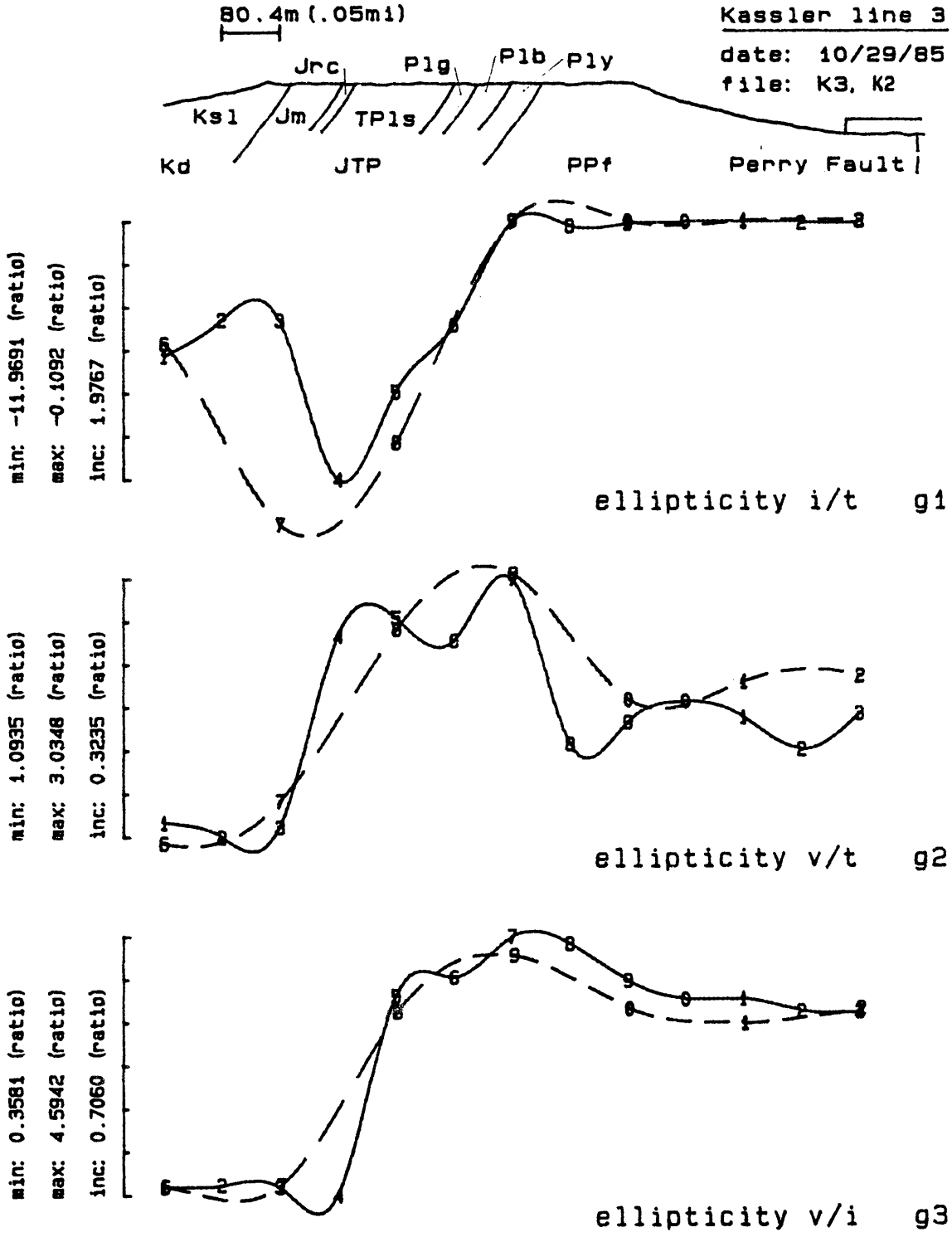

Figure 27. Kassler line 3 polarization ellipticities.

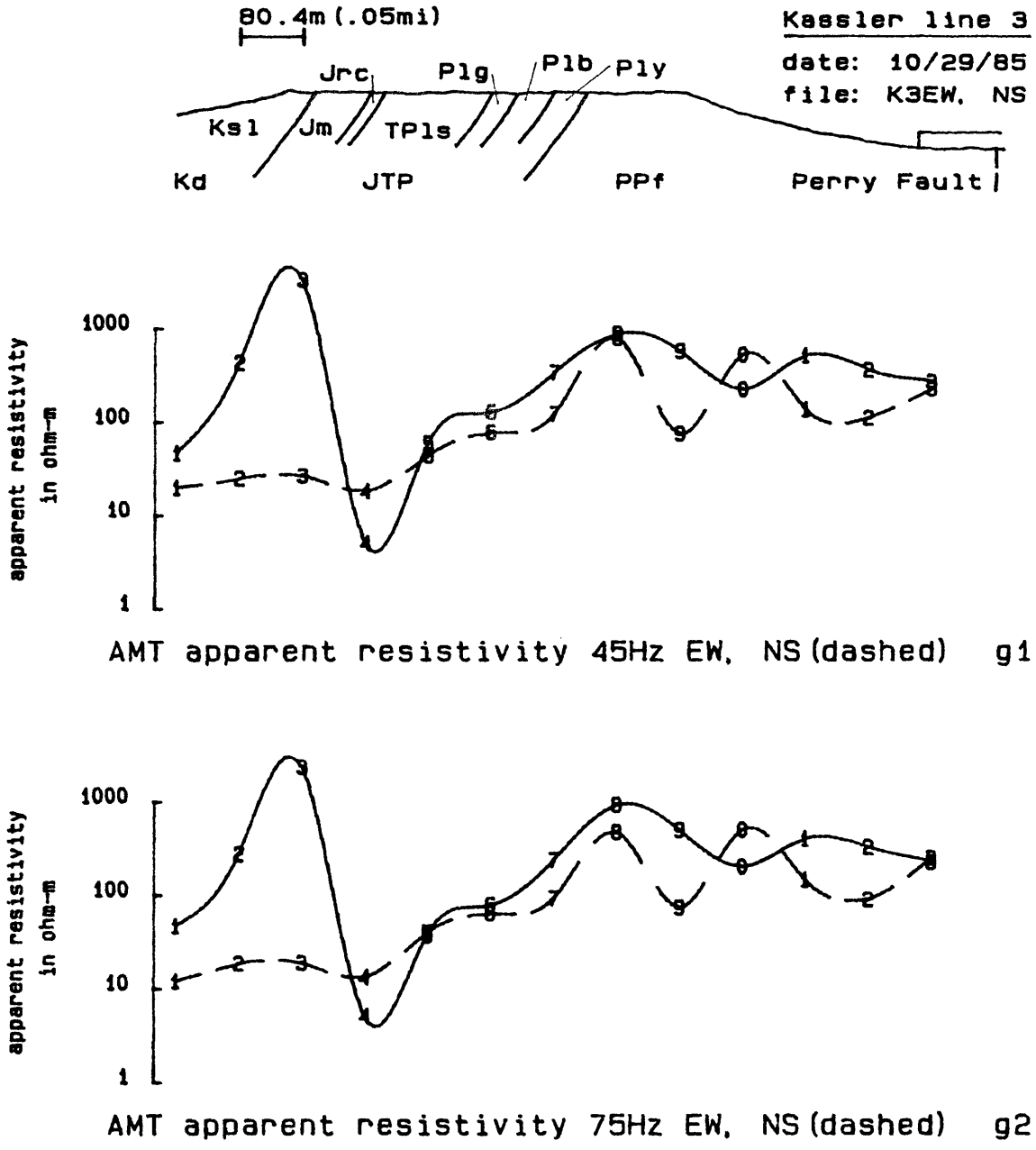

Figure 28. Kassler line 3 AMT apparent resistivities.

structure's strike. As expected, the curve forms an inflection at stations 1 through 6 indicating a correlation with surface charges built-up at the interface associated with the geologic contact. Due to the principles expressed in the Postulate of Charge Conservation and Ohm's law, whenever stationary current applicable to low frequencies intersects a boundary of differing conductivities, a surface charge is created in accordance to Coulomb's law. The measured electrical field senses this extra source by increasing the field on one side of the contact and decreasing it on the other. In contrast, the tangential north-south (NS) E-field experiences no discontinuity, but senses the extra magnetic field due to E-polarization, thereby decreasing the apparent resistivity.

The AMT information is extremely helpful in that it identifies a two dimentional electrictical structure across a geologic contact. This is seen in the graphs at station 3.5 and to lesser extent at a second contact near station 7. This correlates well with the observed sixty-hertz amplitude data (Appendix D, D33) revealing a curve high and inflection in the in-line and vertical channels, respectively. Viewing the polarization curves, the tilt and the ellipticity also show responses at these areas. The horizontal shift observed in graphs g3 can be explained as being caused by the dual contacts. This inward shifting was observed during physical

modeling of two vertical plates by Ward et al., in 1966.

VLF data was also collected over the Kassler line 3. The data shown in Figure 29, graph g2, displays a curve inflection at stations 3.5 and 9. Interestingly enough, the higher frequency response of the VLF does not show a distinct shift reflective of the decreased skin depth of the dipping stucture. More so, it associates the response with the topography rather than with the electrical structure due to the contacts, especially at station 9.

IV.5 System Conclusions and Recommendations

As seen in the data, horizontal primary fields due to sferics are sources to be reckoned with. Although not as strong as power line sources, their presence causes noise and adds dc offsetting to the secondary responses. Power line sources have the advantage of a more consistant source permitting digital recording of the data. At no time did the instrumentation appear to be not operating properly; however, noise in the mountainous zones required slowing the gain clock in order to filter out random spikes from prematurely stepping the gain. The PLL provided excellent system clocking, and the computer proved to be a powerful, reliable tool.

The single current element model, although simplified, shows varying response behavior as observed in the field data. Expanding the well known response function into an equation

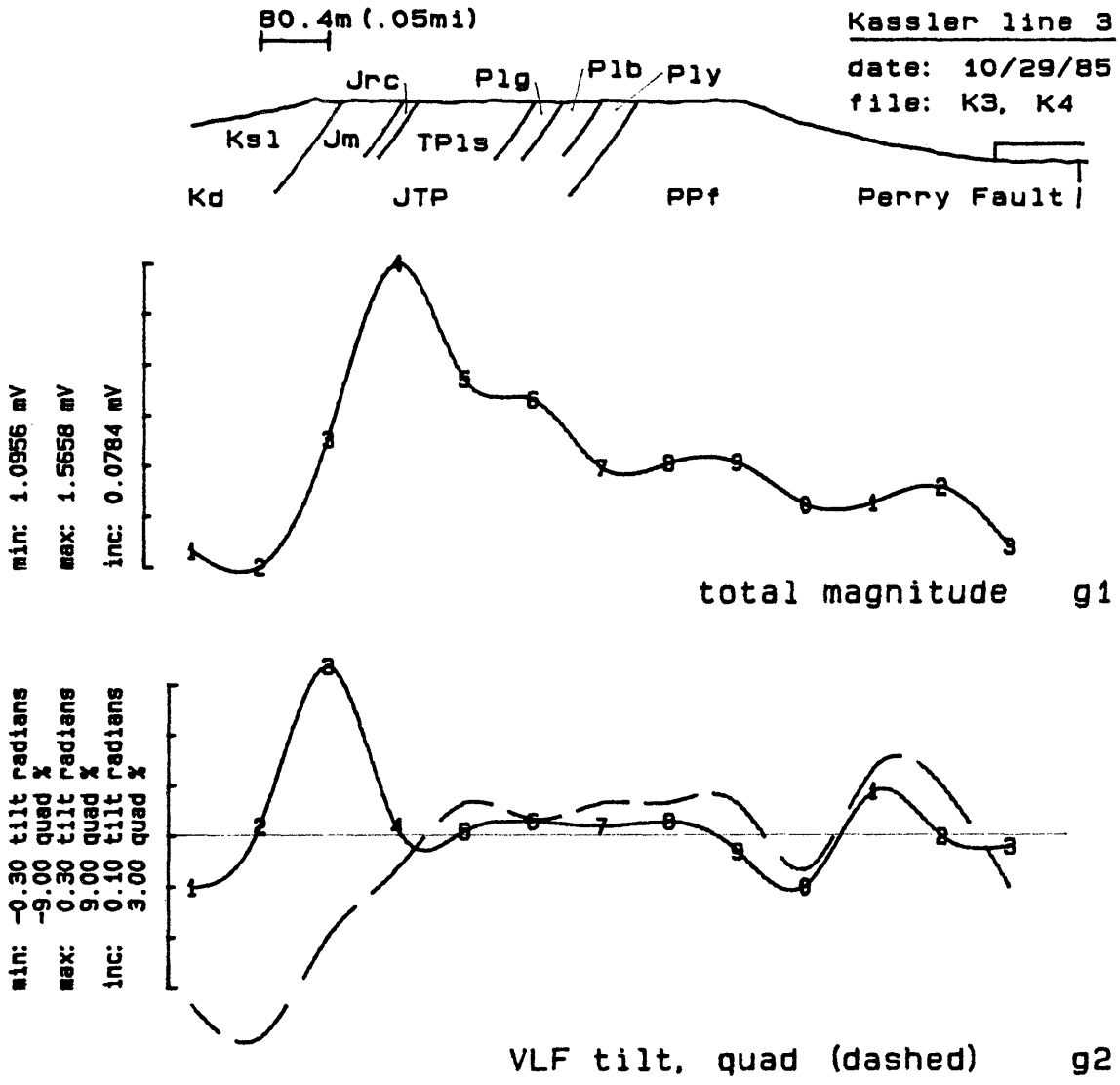

Figure 29. Kassler line 3 VLF polarization parameters.

expressing the receiver's response to the anomaly yields the characteristic curve shapes of highs and inflections. It also defines the interaction between the primary and the secondary fields from which amplitude ratios and phases are seen as the ratios of sums. This apparent behavior of the primary and secondary fields can then be identified and related to either the system response or the secondary conductor.

Data collected in the field for the sixty-hertz system suffers many of the same problems that can be seen in field data collected for AFMAG. One major difference with the use of the sixty-hertz system is in the vertical primary field. It adds a dc offset to the vertical field component which may distort the expected polarization curve character. Tilt and ellipticity calculations are mathematical tools that work best in an ideal situation. Otherwise, as a consequence of the numerical effect, horizontal shifting or different curve shape responses may appear. Nonetheless, with a three component system many of the ambiguities are resolved by considering all of the input parameters determining the polarization.

In comparison, the sixty-hertz system shows a deeper investigation depth and less terrain effect than the VLF. Comparing the system to AMT, AMT has the advantage of a better signal to noise ratio while also having a more definitive response curve shape.

Recommendations to be made at this stage of the development are to proceed as planned with airborne installation of the sixty-hertz system. Testing for data type responses in the air would prove most informative if they overlapped those data lines run on the ground. For the DAS, which was designed as an in flight monitoring tool, it is recommended that observation of the phase change between the vertical and in-line channels will show the most consistant response related to the anomaly's detection. As for data reduction, the two vertical sets of polarization parameters could be combined into one set contained in the vertical plane of the horizontal tilt angle. By a coordinate transformation of axis in reference to Figure 6, the horizontal signal along the H_l azimuth has

$$\text{amplitude} = [A_l^2 \sin^2(\alpha) + A_T^2 \cos^2(\alpha) + A_l A_T \sin(2\alpha) \cos(\Delta\phi)]^{\frac{1}{2}}$$

$$\text{phase} = \text{arctangent} \left[\frac{\text{quad}_T - \text{quad}_l \, \text{Tan}(\alpha)}{\text{real}_T - \text{real}_l \, \text{Tan}(\alpha)} \right].$$

Although this would reduce the the number of graphs by four because data stacking is not practical with an airborne system, effects due to noise may be seen from the different ratios represented in the numerous plots of the data.

References Cited

Born, M., and Wolf, E., 1980, Principles of Optics, New York, Pergamon Press, p. 14-27.

Burr-Brown Research Corporation, 1966, Handbook of Operational Amplifiers, Tucson, 33 p., 78p.

Franks, L.E., 1973, N-path filters, in Modern Theory and Design, Temes and Mitra, Eds., John Wiley and Sons, Inc., p. 495-496.

Hoover, D.B., Long, C.L., and Senterfit, R.M., 1978, Some results from audiomagnetotelluric investigations in geothermal areas, Geophysics, vol. 43, p. 1501-1514.

Johnk, C.T.A., 1975, Engineering Electromagnetic Fields and Waves, New York, John Wiley and Sons, Inc., 45 p.

Kane, G., Harper, S., and Ushijima, D., 1982, The HPIL System, Berkeley, Osborne/McGraw-Hill Inc., p. 88-89.

Kauahikaua, J.P., 1982, The subsurface resistivity structure of Kilauea volcano, Hawaii, Ph.D. thesis, University of Hawaii, 26 p., p. 127-128.

Kaufman, A.A. and Keller, G.V., 1981, The Magnetotelluric Sounding Method, Amsterdam, Elsevier, 1 p., 408 p.

Kaufman, A.A. and Keller, G.V., 1985, Inductive Mining Prospecting Part 1: Theory, Amsterdam, Elsevier, p. 41-67.

Labson, V.F., Becker, A., Morrison, H.F., and Conti, U., Geophysical exploration with audiofrequency natural fields, Geophysics, vol. 50, p. 656-657.

Lancaster, D., 1980, Active Filter Cookbook, Indianapolis, Howard W. Sams and Co. Inc., 128 p., 139 p., 142 p.

Smith, B.D. and Ward, S.H., 1974, On the computation of polarized ellipse parameters, Geophysics, vol. 34, p. 867-869.

Strangway, D.E., Swift, C.M., Jr., and Holmer, R.C., The application of audio-frequency magnetotellurics (AMT) to mineral exploration, Geopyhsics, vol. 38, p. 1159-1175.

Telford, W.M., Geldart, L.P., Sheriff, R.E., and Keys, D.A., 1976, Applied Geophysics, Cambridge, Cambridge University Press, 502 p., 516 p.

Ward, S.H., 1959, AFMAG - airborne and ground, Geophysics, vol. 24, p. 761-789.

Ward, S.H., O'Donnell, J., Rivera, R., Ware, G.H., and Fraser, D.C., 1966, AFMAG - applications and limitations, Geophysics, vol. 31, p. 576-605.

Vozoff, K., 1972, The magnetotelluric method in the exploration of sedimentary basins, Geophysics, vol. 37, p. 98-141.

APPENDIX A

General I/O Considerations

Computer software utilizing Hewlett-Packard's IL/IB interface implementing IEEE standard 488 bus communications initiates the operation of the DAS. The commands recognized by the DAS are outlined below along with the program statements relating to I/O operation. Complete program listings are contained in Appendix C.

- General operation: Due to the lack of control by the computer on the ATTN line pin, it was elected to strobe valid addressing by the pulsing of the REN line pin. Certain commands are trapped by the IL/IB converter while others are put on the data lines (see Kane et al., 1982, for code listing). Table 8 lists the commands used by the IL/IB and DAS.

Table 8

IL/IB Command List

	command	decimal	hex
IL/IB:	IFC	144	90
	REN	146	92
	NRE	147	93
DAS:	multiplexer	32+	20+
	A/D start	48	30
	D/A output	16	10

- Initialization and setting of the multiplexer: Pulsing the IFC initializes the DAS by triggering a power up reset (POR). The multiplexer is set by strobing the REN line while the command number 32 + the number of desired channels is on line. For example, 6 channels are desired, thus 32 + 6 is 38. This is used in program T5, statements 180 and 190.

- A/D start: The command number 48 initiates the A/D conversion. Next, the computer reads the data while the end of conversion signal clocks the multiplexer and the sample-and-hold for the next conversion. This command is used in program T5, statements 1050 and 1070. The HP-71B requires a second input statement (1060 and 1080) to read the IL buffer containing the conversion code. The DAS outputs two bytes interpreted as (most/least significant bit (msb/lsb)):

```
          1st              2nd        (order of bytes read)
   msb       lsb   msb        lsb
  [---- ----      ----] ----
       A/D data          gain data    (index).
```

The voltage to bit representation is:

$$\text{voltage} = \frac{5 \text{ v (+/- full scale)}}{2048 \text{ (11 bits full scale)}} \times \text{A/D output}$$

$$= .00244141 \times \text{A/D output.}$$

The 12th bit acts soley as a sign bit (0 for minus) while the remaining 11 bits behave the same regardless of the polarity of the A/D's analog input. Comparison of the

$$4.9975458 = .00244141 \times 2047 \text{ (maximum 11 bits)}$$

constant determines the signal's polarity. The value of the lower 4 bits in the second byte, + 1, index the gain tables denoted as array G2. These considerations are used in program T5, statements 1140 through 1200.

- D/A output: The Command number 16 indicates to the DAS to accept data for the D/A. Data format is the same as the input format noted above for the A/D. The first byte is the most significant while only the upper four bits of the second byte are used. The range of the D/A is 10 volts from -5 to +5 volts. A zero output by the computer relates to a -5 volts on the D/A. Output values are interpreted as:

$$\text{code output} = \text{value output} \times \frac{4096 \text{ (12 bits)}}{10\text{v (full scale)}} \times \frac{1}{16}$$

$$= 25.6.$$

This constant yields the value of the upper data byte in the integer part while multiplication of the fractional part by 256 equals the second output byte. It is used in program TEST4, statement 370.

APPENDIX B

System Constants

In order to extract correct polarization parameters, the measuring system must have matched channels. Software adjustments for gain and phase accomplished this in the program statements for gain tables and phase corrections. The constants used for this were derived from calibrating the system and are disscused below. Coil sensitivity was also calculated by an indirect means, and although not considered for data reduction, it does aid data interpretation.

Gain testing determined proper gains for each channel. The results are the constants used in array G2 in program T5. Tests were conducted in an approximate six foot cubic shielded room of two inch thick aluminum having a sixty hertz attenuation of 54 decibels. Before making the gain calculations, windows of input voltages were determined for each of the sixteen gain selections. Table 5 lists the approximate input voltages that were fed into the pre-amplifier where an increase and decrease stepping of the auto-gain occurred.

As shown in Table 9, voltages are in units of millivolts. Noise levels were in the 1.5 to 3 microvolt range as determined by input shorting test. Losses in gain linearity were noted [2]

Table 9

Gain Voltage Widows

gain index	nominal gain	increase step	decrease step
1	1	40[2]	38
2	2	23	19.1
3	4	11	10.1
4	8	5	4.8
5	16	3.2	2.56
6	32	1.6	1.4
7	64	.8	.856
8	128	.437	.415
9	256	.187	.165
10	512	.078	.070
11	1024	.036	.036
12	2048	.022	.017
13	4096	.009	.009
14	8192	.005	.004
15	16384	.0025	[3]
16	32768	.001	[3]

for input voltages larger than 40 mV. Voltages marked ([3]) range below accurate signal input capability.

Using the windows as a guide, one input signal was fed into the pre-amplifier's three channels simultaneously while the main amplifier was pre-set to a selected gain. Input signals were created by a sixty hertz source provided by a Hewlett-Packard synthesizer/function generator model 3325A. With a Data Precision digital wave analyzer model 6000, input voltages were measured peak to peak with an accuracy of 62 microvolts. The lower inputs were produced by an attenuated resistor network of 915 to 1. Therefore, an output by the signal generator in

millivolts was measured and divided by 915 to determine an input value.

The computer then read in the A/D conversion results, and in conjunction with the input signal, calculated the gain as

$$\text{gain} = \frac{\text{amplitude of A/D conversion in volts}}{\text{peak to peak signal input in volts}} .$$

An average of three conversions were taken for each input. This was done for three different voltages spanning the window. The program TEST4 performed this task on an HP-75C computer. After analyzing the results, selected gains for each channel were chosen. Further program documentation may be found in Appendix C.

Phase differences existed between the channels. Correcting the problem in the software consisted of adding extra statements that add a constant to the calculated phase. The value of the constants are the phase differences between channels.

The phase difference was determined by inputting a single 60 Hz signal into the pre-amplifier's three channels simultaneously. A test program, TEST6, facilitated the calculations by reading into the computer the A/D conversion of the signal. The phase for each channel was computed and then subtracted from the transverse phase. An average of phase differences resulted as

transverse - in line = -.036 radians (-2.06 deg)
transverse - vertical = .113 radians (6.47 deg).

These measurements are particular to the individual boards which for the test the boards were inserted as:

board 2 - transverse channel
board 1 - in line channel
board 3 - vertical channel.

Program T5 incorporates the above phase corrections in lines 840 and 1240 in the array P4.

Coil sensitivity estimates were made based on AMT apparent resistivity data from the Kassler line. At those stations output from the AMT pre-amplifier's east-west (EW) channel was fed into the main amplifier of the sixty-hertz system bypassing the sixty-hertz pre-amplifier. An otherwise normal station was taken. AMT apparent resistivity is calculated as

$$\rho = \frac{1}{\omega\mu} \frac{E^2}{H^2}$$

where

ρ = apparent resistivity
E = measured E-field voltage/25m electrode separation
H = constant (k) x measured H-field voltage
k = converts millivolts to γ
ω = 2π 60 Hz
μ = $4\pi \times 10^{-7}$ h/m

The constant k is the factor relating to system sensitivity. Clearly, with known values of ρ the factor k may be calculated. Because of noise, k varied from station to station. Program CALK assisted calculation of the sensitivity and is documented in Appendix C.

APPENDIX C

Computer Program Listings

```
10 ! program 'test6'
20 ! phase test
50 !
60 ! initial i/o
70 ASSIGN IO ':c,:p,:i,:
il'
80 PRINTER IS ':p'
85 DISPLAY IS ':c'
90 !
130 ! system response cm
ds
140 ! ifc: 144   90
150 ! ren: 146   92
160 ! nre: 147   93
170 ! mul: 38    26 (32+
chn)
180 ! a/d: 48    30
190 ! d/a: 16    10
200 !
210 ! initial ifc, ren,
set mulx
220 A$=CHR$(144)&CHR$(14
6)&CHR$(38)&CHR$(147)&CH
R$(146)
230 SEND CMD A$
240 !
250 ! a/d cmd list
260 A$=CHR$(48)&CHR$(147
)&CHR$(146)
270 !
280 ! d/a cmd list
290 B$=CHR$(16)&CHR$(147
)&CHR$(146)
300 !
310 ! initial prog
320 ! 1:tran, 2:in ln, 3
:vert
330 DIM M1(3),P(3),G2(3,
16),A(3),I(3),Q(3),P4(3)
,A3(6)
340 DIM I$[6],Q$[6],Q2$[
2]
350 INTEGER J,K
360 OPTION ANGLE RADIANS

370 M5=1
380 G2(1,1)=M5/31.6
390 G2(1,2)=M5/65.87
400 G2(1,3)=M5/128.3
410 G2(1,4)=M5/254.8
420 G2(1,5)=M5/502
430 G2(1,6)=M5/1010
440 G2(1,7)=M5/2120
450 G2(1,8)=M5/4068
460 G2(1,9)=M5/8130
470 G2(1,10)=M5/16300
480 G2(1,11)=M5/33000
490 G2(1,12)=M5/66700
500 G2(1,13)=M5/125000
510 G2(1,14)=M5/222000
520 G2(1,15)=M5/554000
530 G2(1,16)=M5/872000
540 G2(2,1)=M5/31.24
550 G2(2,2)=M5/64.42
560 G2(2,3)=M5/127.2
570 G2(2,4)=M5/253
580 G2(2,5)=M5/498
590 G2(2,6)=M5/1005
600 G2(2,7)=M5/2000
610 G2(2,8)=M5/4038
620 G2(2,9)=M5/8070
630 G2(2,10)=M5/16200
640 G2(2,11)=M5/32800
650 G2(2,12)=M5/66500
660 G2(2,13)=M5/130000
670 G2(2,14)=M5/229000
680 G2(2,15)=M5/617000
690 G2(2,16)=M5/870000
700 G2(3,1)=M5/30.9
710 G2(3,2)=M5/63.4
720 G2(3,3)=M5/125.5
730 G2(3,4)=M5/249.6
740 G2(3,5)=M5/489
750 G2(3,6)=M5/985
760 G2(3,7)=M5/1972
770 G2(3,8)=M5/3960
780 G2(3,9)=M5/7900
790 G2(3,10)=M5/16000
800 G2(3,11)=M5/32200
810 G2(3,12)=M5/65600
820 G2(3,13)=M5/130000
830 G2(3,14)=M5/225000
840 G2(3,15)=M5/577000
850 G2(3,16)=M5/870000
860 !
870 ! phase correction
880 P4(1)=0 @ P4(2)=0 @
P4(3)=0
890 !
900 DESTROY A1,A2,A3,A4,
A5,A3
905 N1=1
910 FOR N=1 TO N1
920 !
930 ! read in signal
940 FOR K=1 TO 3
950 J=2*K
960 SEND CMD A$ MLA TALK
 5
970 ENTER :LOOP ;I$[J-1,
J]
980 SEND CMD A$ MLA TALK
 5
990 ENTER :LOOP ;Q$[J-1,
J]
1000 NEXT K
1010 !
1020 ! reduce data
1030 FOR K=1 TO 3
1040 J=2*K
1050 R1=NUM(I$[J])/16
1060 G1=FP(R1)*16+1
1070 I(K)=(NUM(I$[J-1])*
16+INT(R1))*.0024414
1080 IF I(K)>4.9975458 T
HEN I(K)=I(K)-5 ELSE I(K
)=-I(K)
1090 !
1100 Q(K)=(NUM(Q$[J-1])*
16+INT(NUM(Q$[J])/16))*.
0024414
1110 IF Q(K)>4.9975458 T
HEN Q(K)=Q(K)-5 ELSE Q(K
)=-Q(K)
1112 A3(J-1)=A3(J-1)+I(K
)
1114 A3(J)=A3(J)+Q(K)
1120 M1(K)=I(K)*I(K)+Q(K
)*Q(K)
1130 A(K)=SQR(M1(K))
1140 P(K)=ANGLE(I(K),Q(K
))+P4(K)
1150 NEXT K
1160 !
```

```
1170 ! cal output
1180 A1=A1+P(1)-P(2)
1190 A2=A2+P(1)-P(3)
1470 NEXT N
1480 !
1485 PRINT
1490 PRINT 'avg of ';N1;
' readings'
1492 FOR J=1 TO 6
1494 PRINT ' a ';J;': ';
A3(J)/N1
1496 NEXT J
1500 PRINT ' T-I: ';A1/N
1
1510 PRINT ' T-V: ';A2/N
1
1515 PRINT
1520 !
1530 GOTO 900
1540 STOP
1550 END
```

```
10 ! program 'test4'; ca
l gain
20 DIM I$[6],Q$[6],I(6),
Q(6),G1(
3)
30 !
40 SENDIO '','TL+,REN,CD
:90',''
50 SENDIO '','tl+,cd:26,
nre,ren'
,''
60 !
70 ASSIGN IO ':p,:i,:i1'
90 PRINTER IS ':p'
100 !
110 DISP
120 INPUT ' amp in: ';A
130 INPUT 'auto gain: ';
G$
140 G1(1)=0 @ G1(2)=0 @
G1(3)=0
150 FOR N=1 TO 3
160 FOR K=1 TO 3
170 J=2*K
180 I$[J-1,J]=ENTIO$('',
'TL+,CD:
30,NRE,REN,CD:44,SDA')
190 Q$[J-1,J]=ENTIO$('',
'TL+,CD:
30,NRE,REN,cd:44,SDA')
200 NEXT K
210 !
220 DISP
230 FOR K=1 TO 3
240 J=2*K
250 R1=NUM(I$[J])/16
260 L=INT(R1)
270 G=16*FP(R1)+1
280 I(K)=(NUM(I$[J-1])*1
6+L)*.00
24414
285 IF I(K)>9.996 THEN P
RINT 'In
 full scale'
286 IF I(K)<.002 THEN PR
INT 'In
under scale'
290 IF I(K)>4.9975458 TH
```

```
EN I(K)=
I(K)-5 ELSE I(K)=-I(K)
300 !
310 L=INT(NUM(Q$[J])/16)
320 Q(K)=(NUM(Q$[J-1])*1
6+L)*.00
24414
325 IF Q(K)>9.996 THEN P
RINT 'Qd
 full scale'
326 IF Q(K)<.002 THEN PR
INT 'Qd
under scale'
330 IF Q(K)>4.9975458 TH
EN Q(K)=
Q(K)-5 ELSE Q(K)=-Q(K)
340 DISP 'I';I(K);'Q';Q(
K);'   G
';G
350 NEXT K
360 !
370 R1=(I(1)+5)*25.6
380 O$[1]=CHR$(INT(R1))
390 O$[2]=CHR$(FP(R1)*25
6)
400 SENDIO '','TL+,CD:10
,NRE,REN
',O$
410 !
420 FOR K=1 TO 3
430 A2=SQR(I(K)*I(K)+Q(K
)*Q(K))
440 G1(K)=G1(K)+A2/A
450 NEXT K
460 NEXT N
470 PRINT
480 PRINT 'amp in';A
490 PRINT 'auto G:';G$
500 PRINT 'average gain'
510 FOR K=1 TO 3
520 PRINT K;G1(K)/3
530 NEXT K
540 !
550 PRINT
560 GOTO 110
570 STOP
580 END
```

```
10 ! program 't5' for co
llecting field data
20 ! output to file/prin
ter
30 ! before run, dim a4(
12,50), a7(50)
40 !
50 ! initial i/o
60 ASSIGN IO ':p,:i,:il'
70 PRINTER IS ':p'
80 !
90 ! system response cmd
s
100 ! ifc: 144   90
110 ! ren: 146   92
120 ! nre: 147   93
130 ! mul: 38    26 (32+
chn)
140 ! a/d: 48    30
150 ! d/a: 16    10
160 !
170 ! initial ifc, ren,
set mulx
180 A$=CHR$(144)&CHR$(14
6)&CHR$(38)&CHR$(147)&CH
R$(146)
190 SEND CMD A$
200 !
210 ! a/d cmd list
220 A$=CHR$(48)&CHR$(147
)&CHR$(146)
230 !
240 ! d/a cmd list
250 B$=CHR$(16)&CHR$(147
)&CHR$(146)
260 !
270 ! initial prog
280 ! 1:tran, 2:in ln, 3
:vert
290 DIM M1(3),P(3),G2(3,
16),A(3),I(3),Q(3),P4(3)
300 DIM I$[6],Q$[6],Q2$[
2]
310 INTEGER J,K,L
320 OPTION ANGLE RADIANS

330 M5=1000
340 G2(1,1)=M5/31.6
350 G2(1,2)=M5/65.07
360 G2(1,3)=M5/128.3
370 G2(1,4)=M5/254.8
380 G2(1,5)=M5/502
390 G2(1,6)=M5/1010
400 G2(1,7)=M5/2120
410 G2(1,8)=M5/4068
420 G2(1,9)=M5/8130
430 G2(1,10)=M5/16300
440 G2(1,11)=M5/33000
450 G2(1,12)=M5/66700
460 G2(1,13)=M5/125000
470 G2(1,14)=M5/222000
480 G2(1,15)=M5/554000
490 G2(1,16)=M5/872000
500 G2(2,1)=M5/31.24
510 G2(2,2)=M5/64.42
520 G2(2,3)=M5/127.2
530 G2(2,4)=M5/253
540 G2(2,5)=M5/498
550 G2(2,6)=M5/1005
560 G2(2,7)=M5/2000
570 G2(2,8)=M5/4038
580 G2(2,9)=M5/8070
590 G2(2,10)=M5/16200
600 G2(2,11)=M5/32800
610 G2(2,12)=M5/66500
620 G2(2,13)=M5/130000
630 G2(2,14)=M5/229000
640 G2(2,15)=M5/617000
650 G2(2,16)=M5/870000
660 G2(3,1)=M5/30.9
670 G2(3,2)=M5/63.4
680 G2(3,3)=M5/125.5
690 G2(3,4)=M5/249.6
700 G2(3,5)=M5/489
710 G2(3,6)=M5/985
720 G2(3,7)=M5/1972
730 G2(3,8)=M5/3960
740 G2(3,9)=M5/7900
750 G2(3,10)=M5/16000
760 G2(3,11)=M5/32200
770 G2(3,12)=M5/65600
780 G2(3,13)=M5/130000
790 G2(3,14)=M5/225000
800 G2(3,15)=M5/577000
810 G2(3,16)=M5/870000
820 !
830 ! phase correction
840 P4(1)=0 @ P4(2)=-.03
6 @ P4(3)=.113
850 S=S+1
860 DISP 'stat:';S;
870 INPUT ' or ';S1$
880 IF LEN(S1$)<>0 THEN
S=VAL(S1$)
890 !
895 I2=.05
900 A7(S)=A7(S-1)+I2
910 DISP 'ai:';A7(S);
920 INPUT ' or ';S1$
930 IF LEN(S1$)<>0 THEN
A7(S)=VAL(S1$)
940 !
950 INPUT 'com: ';C$
960 PRINT 'sta:';S;'/';A
7(S);' ';TIME$
970 PRINT C$
980 !
990 ! PRINT @ PRINT TIME
$;'     ';S;'/';A7(S)
1000 FOR L=1 TO 2
1010 !
1020 ! read in signal
1030 FOR K=1 TO 3
1040 J=2*K
1050 SEND CMD A$ MLA TAL
K 5
1060 ENTER :LOOP ;I$[J-1
,J]
1070 SEND CMD A$ MLA TAL
K 5
1080 ENTER :LOOP ;Q$[J-1
,J]
1090 NEXT K
1100 !
1110 ! reduce data
1120 FOR K=1 TO 3
1130 J=2*K
1140 R1=NUM(I$[J])/16
1150 G1=FP(R1)*16+1
1155 PRINT 'g';G1;
1160 I(K)=(NUM(I$[J-1])*
16+INT(R1))*.0024414
```

```
1170 IF I(K))4.9975458 T
HEN I(K)=(I(K)-5)*G2(K,G
1) ELSE I(K)=-I(K)*G2(K,
G1)
1180 !
1190 Q(K)=(NUM(Q$[J-1])*
16+INT(NUM(Q$[J])/16))*.
0024414
1200 IF Q(K))4.9975458 T
HEN Q(K)=(Q(K)-5)*G2(K,G
1) ELSE Q(K)=-Q(K)*G2(K,
G1)
1210 !
1220 M1(K)=I(K)*I(K)+Q(K
)*Q(K)
1230 A(K)=SQR(M1(K))
1240 P(K)=ANGLE(I(K),Q(K
))+P4(K)
1250 A4(J-1,S)=I(K)
1260 A4(J,S)=Q(K)
1270 NEXT K
1280 PRINT
1290 !
1300 ! cal output
1310 ! opt 1 mag
1320 M=SQR(M1(1)+M1(2)+M
1(3))
1330 A4(7,S)=M
1340 PRINT ' mag:';M
1350 !
1360 ! opt 2 h tilt
1370 P1=P(2)-P(1)
1380 IF M1(1)=M1(2) THEN
 T3=.7853982 @ GOTO 1400
1390 T3=.5*ATAN(2*A(2)*C
OS(P1)/(A(1)*(1-M1(2)/M1
(1))))
1400 A4(8,S)=T3
1410 PRINT ' h t:';T3
1420 !
1430 ! opt 3 h  ellip
1440 E3=A(1)*A(2)*SIN(P1
)/((A(2)*COS(P1)*SIN(T3)
+A(1)*COS(T3))^2+(A(2)*S
IN(T3)*SIN(P1))^2)
1450 A4(9,S)=E3
1460 PRINT ' h e:';E3
1470 !
1480 ! opt 4 v tilt
1490 IF M1(3)=M1(2) THEN
 T3=.7853982 @ GOTO 1520
1500 P1=P(3)-P(2)
1510 T3=.5*ATAN(2*A(3)*C
OS(P1)/(A(2)*(1-M1(3)/M1
(2))))
1520 A4(10,S)=T3
1530 PRINT ' v t:';T3
1540 !
1550 ! opt 5 v ellip
1560 E3=A(3)*A(2)*SIN(P1
)/((A(3)*COS(P1)*SIN(T3)
+A(2)*COS(T3))^2+(A(3)*S
IN(T3)*SIN(P1))^2)
1570 A4(11,S)=E3
1580 PRINT ' v e:';E3
1590 !
1600 NEXT L
1610 !
1620 ! S=S+1 @ A7(S)=A7(
S-1)+I2 @ GOTO 990
1630 INPUT 'store: ','ye
s';C$
1640 IF C$()'yes' THEN G
OTO 1000
1650 !
1660 PRINT 'stored--)';S
1670 PRINT
1680 STOP
1690 END



10 ! prog 'calk'
20 ! cal k-factor
30 C1=1/SQR(2*PI*60*PI*.
0000004)/25/1.6
40 C2=.4*PI
50 !
60 FOR J=1 TO 2
70 IF J=1 THEN PRINT '45
 '; ELSE PRINT '75 ';
80 PRINT 'Hz AMT E ew'
90 !
100 FOR K=1 TO 8
110 N2=2*K
120 N1=N2-1
130 ! stat
140 IF K=8 THEN S=11 ELS
E S=K+1
150 ! avg ratio e/h
160 A1=(A4(13,N2)+A4(13,
N1))/2
170 !
180 ! cal k1 units of (a
mp-turn/m)/volts
190 K1=C1*A1/SQR(B4(J,S)
)
200 !
210 PRINT 'stat:';S;' re
s:';B4(J,S)
220 PRINT ' dif:';A4(13,
N2)-A4(13,N1)
230 PRINT '  k1:';K1
240 PRINT ' k-f:';K1*C2
250 PRINT
260 NEXT K
270 NEXT J
280 STOP
290 ! cal amp-res
300 C1=1/(1.6*1.6*2*PI*6
0*.0000004*PI)
310 INPUT 'k1: ';K1
320 PRINT 'k1: ';K1
330 !
340 FOR K=1 TO 8
350 N2=2*K
360 N1=N2-1
370 A5(K)=C1*(A4(13,N2)+
A4(13,N1))^2/(2500*K1*K1
)
380 IF K=8 THEN PRINT '1
1'; ELSE PRINT K+1;
390 PRINT A5(K)
400 NEXT K
410 STOP
```

```
10 ! file: 'fdat'
20 ! progam plot/store d
ata
30 ASSIGN IO ':p,:t'
40 PRINTER IS ':p'
50 DIM M1(12),M2(12),P$(
12)[20]
60 INTEGER I,K,N,N1,N2
70 REAL S,B
80 !
90 INPUT 'file: ';F$
100 INPUT '1st plot:';N1
110 INPUT 'end plot:';N2
120 INPUT 'com: ';C$
130 INPUT 'no. of stat:
';I
140 CREATE DATA F$
150 ASSIGN #1 TO F$
160 PRINT #1;C$
170 PRINT #1;I
180 FOR N=N1 TO N2
190 M1(N)=MAXREAL
200 M2(N)=-MAXREAL
210 NEXT N
220 !
230 P$(1)='tran real in
mV'
240 P$(2)='tran quad in
mV'
250 P$(3)='in-line real
in mV'
260 P$(4)='in-line quad
in mV'
270 P$(5)='vert real in
mV'
280 P$(6)='vert quad in
mV'
290 P$(7)='magnitude in
mV'
300 P$(8)='horz tilt in
rad i/t'
310 P$(9)='horz elliptic
ity i/t'
320 P$(10)='vert tilt in
 rad v/i'
330 P$(11)='vert ellipti
city v/i'
350 !
360 FOR K=1 TO I
370 FOR N=1 TO 12
380 IF N<7 THEN PRINT #1
;A4(N,K)
390 IF A4(N,K)<M1(N) THE
N M1(N)=A4(N,K)
400 IF A4(N,K)>M2(N) THE
N M2(N)=A4(N,K)
410 NEXT N
420 PRINT #1;A7(K)
430 !
440 NEXT K
450 !
460 PRINT 'file: ';F$
470 PRINT C$
480 PRINT
490 FOR N=N1 TO N2
500 PRINT P$(N)
510 PRINT 'min:';M1(N)
520 PRINT 'max:';M2(N)
530 S=23/(M2(N)-M1(N))
540 PRINT 'inc:';1/S
550 PRINT '=============
==========='
560 B=M1(N)*S-1
570 R2=A7(1)
580 !
590 FOR K=1 TO I
600 IF A7(K)<>R2 THEN R2
=R2+I2 @ PRINT @ GOTO 60
0
610 PRINT TAB(A4(N,K)*S-
B);STR$(MOD(K,10))
620 R2=R2+I2
630 NEXT K
640 !
650 NEXT N
660 !
670 COPY F$ TO F$&':T'
680 ASSIGN #1 TO *
690 PURGE F$
700 STOP
710 END
```

```
10 ! file: 'rdat'
20 ! progam read data
30 DIM A7(30)
40 INTEGER I,K,N
50 !
60 INPUT 'file: ';F$
70 COPY F$&':c' TO F$
80 ASSIGN #1 TO F$
90 READ #1;C$
100 READ #1;I
110 !
120 FOR K=1 TO I
130 FOR N=1 TO 6
140 READ #1;A4(N,K)
150 NEXT N
160 READ #1;A7(K)
170 NEXT K
180 !
190 ASSIGN #1 TO *
200 PURGE F$
210 !
220 ! cal amp and phase
230 DIM P4(3)
240 P4(1)=0 @ P4(2)=-.03
6 @ P4(3)=.113
250 !
260 FOR K=1 TO 3
270 J=2*K
280 N=J-1
290 J1=J+6
300 N1=N+6
310 !
320 FOR L=1 TO I
330 A4(N1,L)=SQR(A4(N,L)
*A4(N,L)+A4(J,L)*A4(J,L)
)
340 !
350 A4(J1,L)=ANGLE(A4(N,
L),A4(J,L))+P4(K)
360 NEXT L
370 NEXT K
380 RUN CAL
390 STOP
400 END
```

```
10 ! prg 'cal'
15 ! calulates data
20 REAL C,S,R,P,T,R1
30 INTEGER N1,N2,J1,J2,J
3,J4
40 OPTION ANGLE RADIANS
50 !
60 N1=9 @ N3=10
70 N2=7 @ N4=8
80 J1=13 @ J2=14
90 J3=19 @ J4=20
100 FOR N=1 TO 3
110 FOR K=1 TO I
120 DISP K
130 R=A4(N1,K)/A4(N2,K)
140 A4(J1,K)=R
150 !
160 P=A4(N3,K)-A4(N4,K)
170 A4(J2,K)=P
180 C=COS(P)
190 S=SIN(P)
200 !
210 IF R<>1 THEN T=.5*AT
AN(2*R*C/(1-R*R)) ELSE T
=.7853982
220 A4(J3,K)=T
230 !
240 R1=(A4(N1,K)*C*SIN(T
)+A4(N2,K)*COS(T))^2+(A4
(N1,K)*S*SIN(T))^2
250 IF R1=0 THEN A4(J4,K
)=MAXREAL ELSE A4(J4,K)=
A4(N1,K)*A4(N2,K)*S/R1
260 !
270 A4(25,K)=SQR(A4(7,K)
*A4(7,K)+A4(9,K)*A4(9,K)
+A4(11,K)*A4(11,K))
280 NEXT K
290 !
300 IF N=1 THEN N1=11 @
N3=12
310 IF N=2 THEN N2=9 @ N
4=10
320 J1=J1+2 @ J2=J2+2
330 J3=J3+2 @ J4=J4+2
340 NEXT N
350 DESTROY N1,N2,N3,N4,
```

```
10 ! 'FM' forward model
15 ! based on free air c
ouplins
20 INTEGER I
30 DIM Q3(3),K3(3),K2(3)
,K4(3)
40 REAL M2,M1,R2,Q,L2,Z1
,Z2,K1,I1
50 OPTION ANGLE RADIANS
52 STD
60 !
70 INPUT 'Q: ';Q
90 INPUT 'M/L: ';M1
130 !
140 W=2*PI*60
150 Q3(1)=-94.1/2570*W
160 Q3(2)=-90.1/2696*W
170 Q3(3)=-93.2/2546*W
180 K1=1-W
210 !
220 R=Q/(Q*Q+1)*M1
230 FOR K=1 TO 3
240 K3(K)=W/Q3(K)+Q3(K)
250 K2(K)=R*(Q*W-Q-Q3(K)
-Q/Q3(K))
260 K4(K)=R*(-Q*Q3(K)+1-
Q*W/Q3(K)-W)
270 NEXT K
280 !
290 Z1=-20
300 Z2=300
310 X1=53526
330 A7(1)=0
340 !
350 C1=COS(.245)
360 S1=SIN(.245)
370 C2=COS(.1)
380 S2=SIN(.1)
390 !
420 ! stat inc
430 I1=1/4*528
431 !
432 T1$='z1:'&STR$(Z1)&'
 z2:'&STR$(Z2)&' x1:'&ST
R$(X1)
434 T2$='i1:'&STR$(I1)&'
 Q:'&STR$(Q)&' M/L:'&STR
$(M1)
```

```
436 DISP T1$
438 DISP T2$
440 I=10
450 FOR K=1 TO I
460 X=(K+400)*I1
470 A7(K+1)=A7(K)+.05
475 ! put in mV
490 D1=.001*(X*C1*X*C1+Z
1*Z1)
500 D2=.001*((X-X1)*(X-X
1)*C2*C2+Z2*Z2)
510 !
520 ! tran
530 M1=Z1/D1 @ M2=Z2/D2
540 R=M1*S1*K1+M2*S2*K2(
1)
550 Q=M1*S1*K3(1)+M2*S2*
K4(1)
560 A4(1,K)=R
570 A4(2,K)=Q
580 A4(7,K)=SQR(R*R+Q*Q)
590 A4(8,K)=ANGLE(R,Q)
600 !
610 ! in-line
620 R=M1*C1*K1+M2*C2*K2(
2)
630 Q=M1*C1*K3(2)+M2*C2*
K4(2)
640 A4(3,K)=R
650 A4(4,K)=Q
660 A4(9,K)=SQR(R*R+Q*Q)
670 A4(10,K)=ANGLE(R,Q)
680 !
690 ! vert
700 M1=X*C1/D1 @ M2=(X-X
1)*C2/D2
710 R=M1*K1+M2*K2(3)
720 Q=M1*K3(3)+M2*K4(3)
730 A4(5,K)=R
740 A4(6,K)=Q
750 A4(11,K)=SQR(R*R+Q*Q
)
760 A4(12,K)=ANGLE(R,Q)
770 NEXT K
780 DESTROY M2,M1,R2,Q,L
2,Z1,Z2,K1,Q3,K2,K3,K4,D
1,D2,C1,C2,S1,S2,X1,I1,R
790 RUN CAL
```

APPENDIX D

Supporting Graphs and Maps

APPENDIX D (index continued)

vertical real

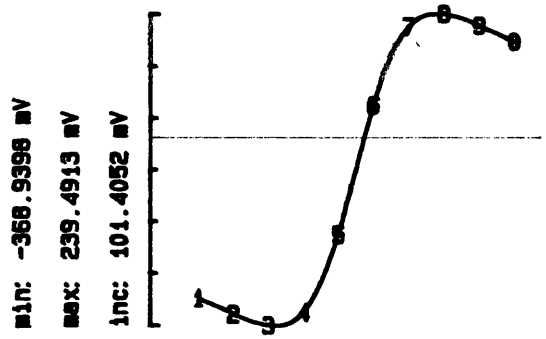

z1: -20 z2: 300 x1: 6006
i1: 132 Q: -1 M/L: 1 g1

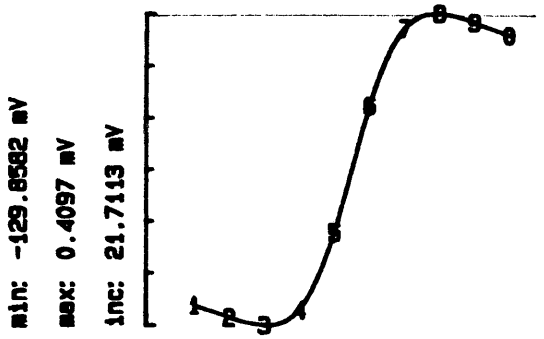

z1: -20 z2: 300 x1: 6006
i1: 132 Q: -10 M/L: .1 g2

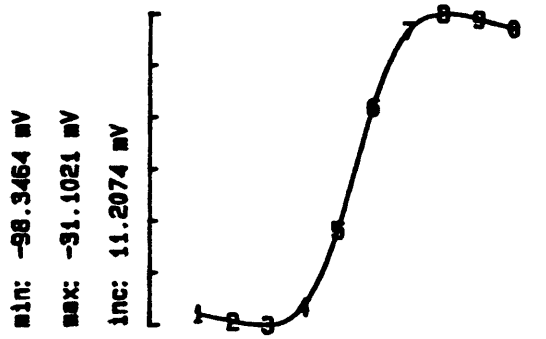

z1: -20 z2: 300 x1: 6006
i1: 132 Q: -1 M/L: .1 g3

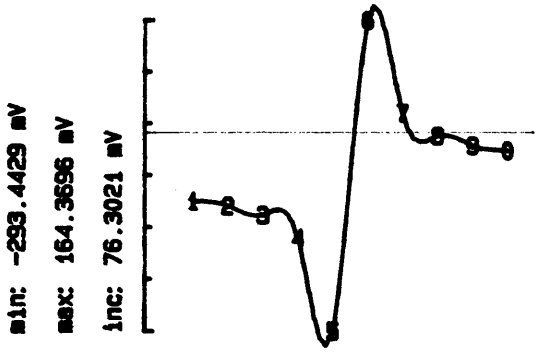

z1: -20 z2: 30 x1: 6006
i1: 132 Q: -1 M/L: .1 g4

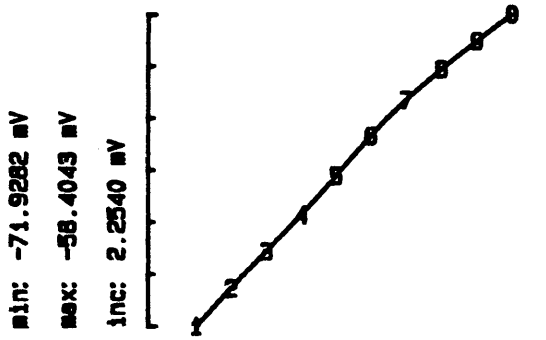

z1: -20 z2: 300 x1: 6006
i1: 132 Q: -.1 M/L: .1 g5

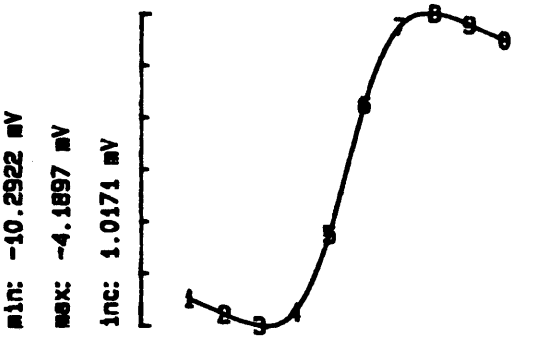

z1: -20 z2: 300 x1: 53526
i1: 132 Q: -1 M/L: .01 g6

Graphs D1

vertical quad

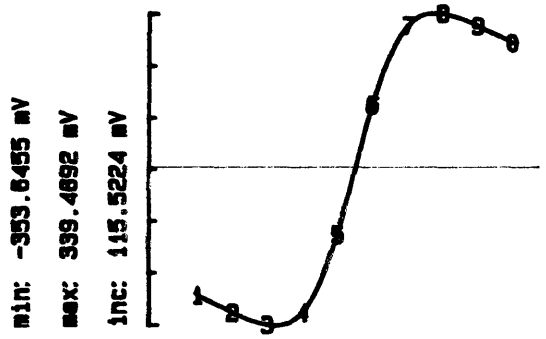

z1: -20 z2: 300 x1: 6006
i1: 132 Q: -1 M/L: 1 g1

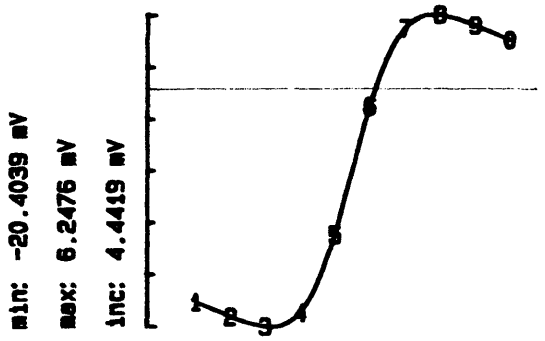

z1: -20 z2: 300 x1: 6006
i1: 132 Q: -10 M/L: .1 g2

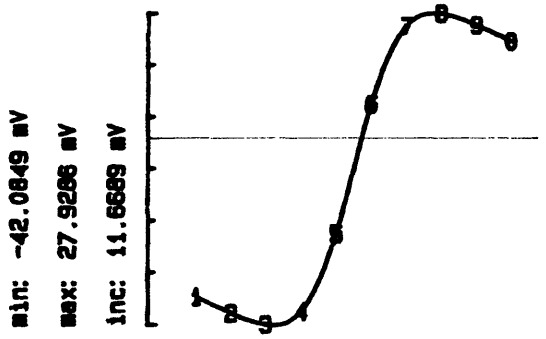

z1: -20 z2: 300 x1: 6006
i1: 132 Q: -1 M/L: .1 g3

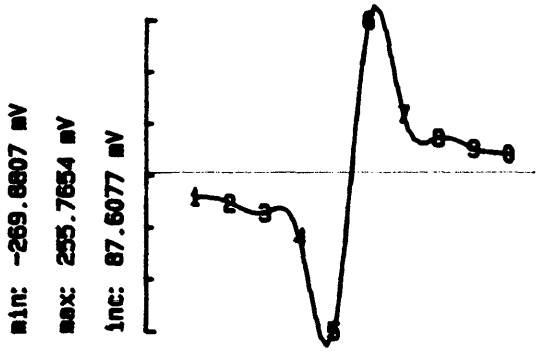

z1: -20 z2: 30 x1: 6006
i1: 132 Q: -1 M/L: .1 g4

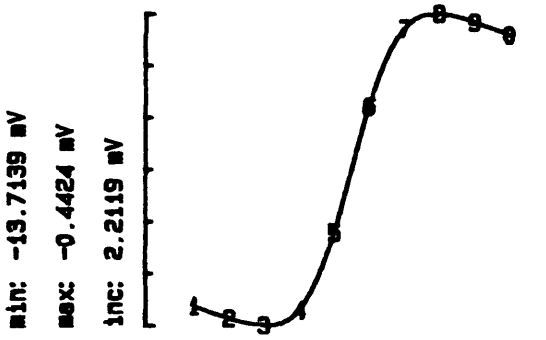

z1: -20 z2: 300 x1: 6006
i1: 132 Q: -.1 M/L: .1 g5

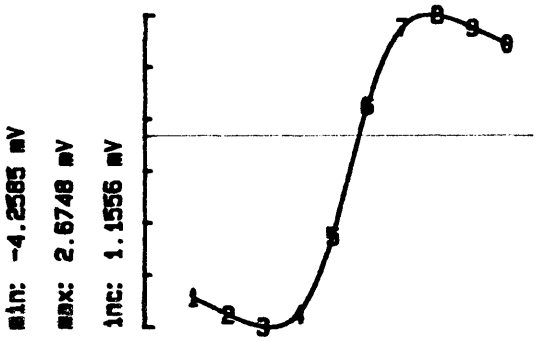

z1: -20 z2: 300 x1: 53526
i1: 132 Q: -1 M/L: .01 g6

Graphs D2

transverse phase

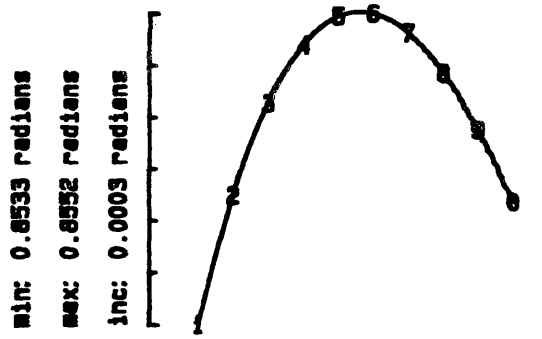

z1: -20 z2: 300 x1: 6006
i1: 132 Q: -1 M/L: 1 g1

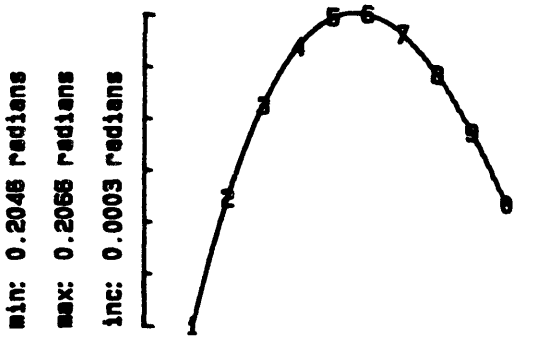

z1: -20 z2: 300 x1: 6006
i1: 132 Q: -10 M/L: .1 g2

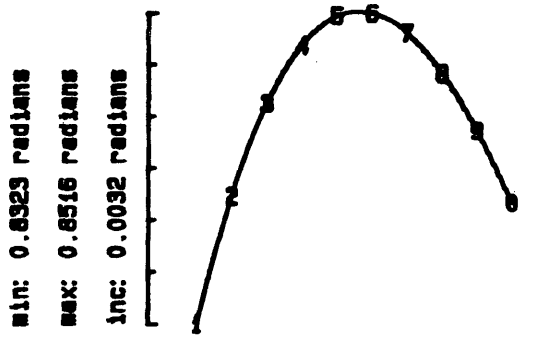

z1: -20 z2: 300 x1: 6006
i1: 132 Q: -1 M/L: .1 g3

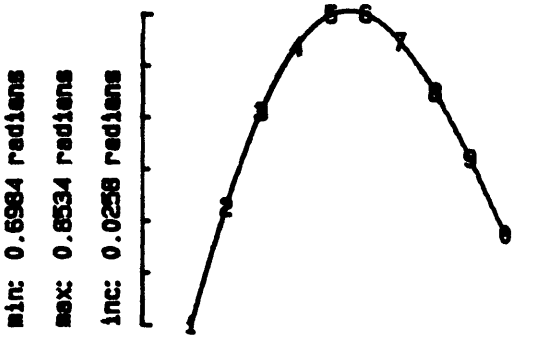

z1: -20 z2: 30 x1: 6006
i1: 132 Q: -1 M/L: .1 g4

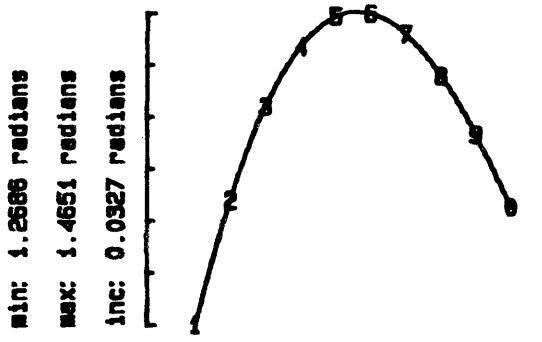

z1: -20 z2: 300 x1: 6006
i1: 132 Q: -.1 M/L: .1 g5

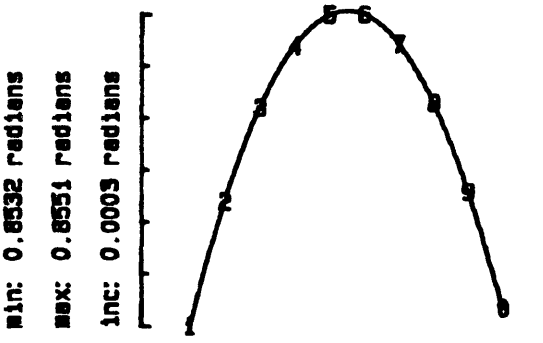

z1: -20 z2: 300 x1: 53526
i1: 132 Q: -1 M/L: .01 g6

Graphs D3

tilt i/t

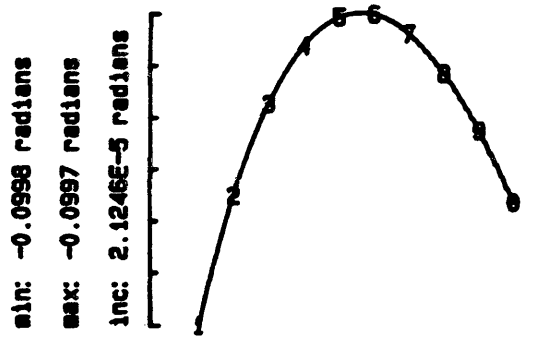

z1: -20 z2: 300 x1: 6006
i1: 132 Q: -1 M/L: 1 g1

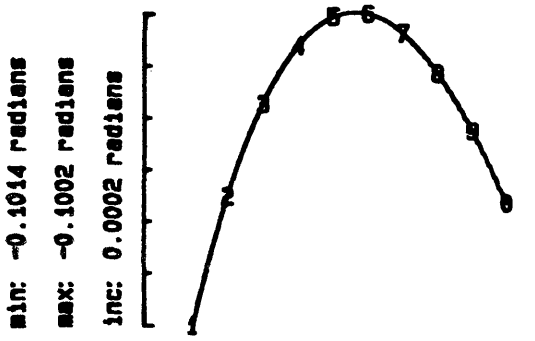

z1: -20 z2: 300 x1: 6006
i1: 132 Q: -10 M/L: .1 g2

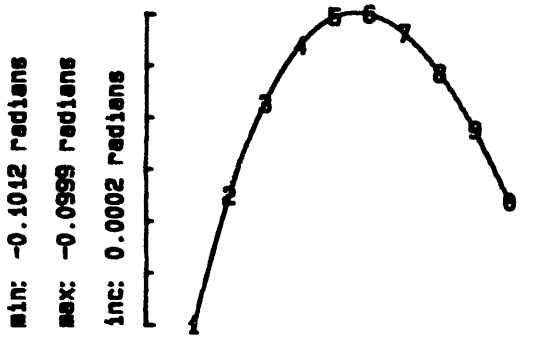

z1: -20 z2: 300 x1: 6006
i1: 132 Q: -1 M/L: .1 g3

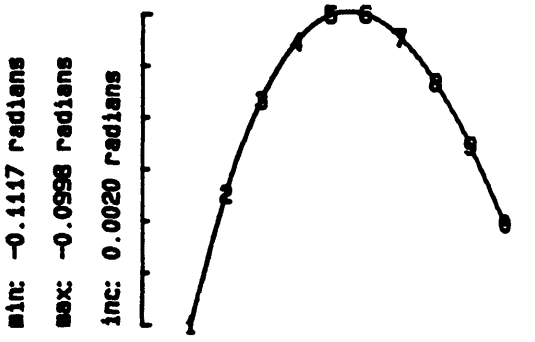

z1: -20 z2: 30 x1: 6006
i1: 132 Q: -1 M/L: .1 g4

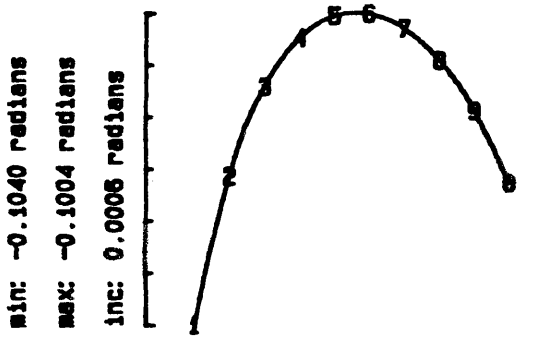

z1: -20 z2: 300 x1: 6006
i1: 132 Q: -.1 M/L: .1 g5

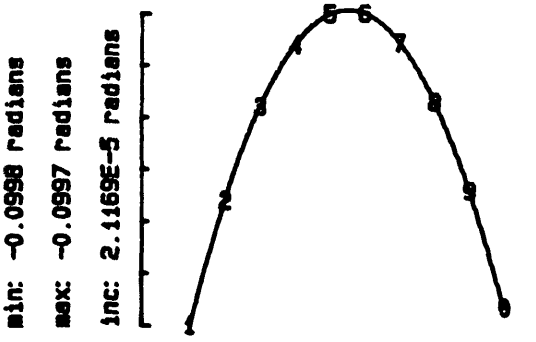

z1: -20 z2: 300 x1: 53526
i1: 132 Q: -1 M/L: .01 g6

Graphs D4

ellipticity i/t

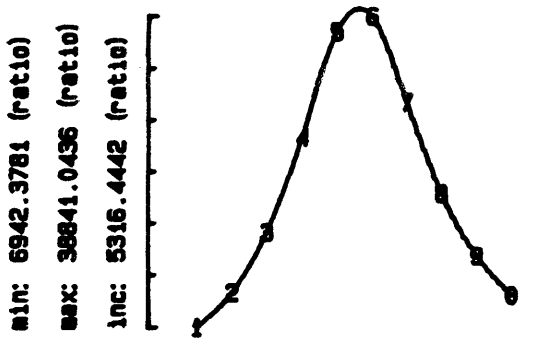

z1: -20 z2: 300 x1: 6006
i1: 132 Q: -1 M/L: 1 g1

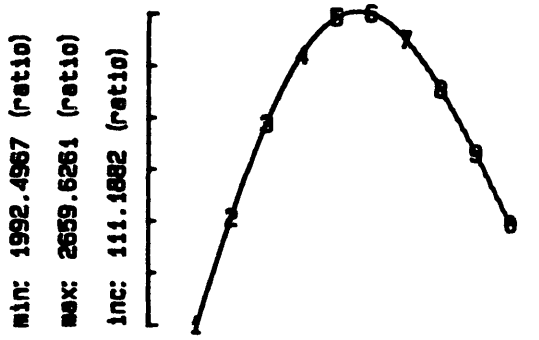

z1: -20 z2: 300 x1: 6006
i1: 132 Q: -10 M/L: .1 g2

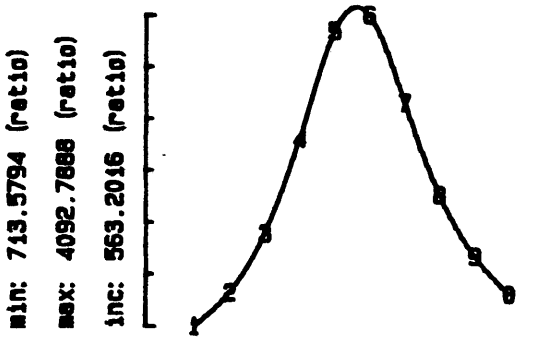

z1: -20 z2: 300 x1: 6006
i1: 132 Q: -1 M/L: .1 g3

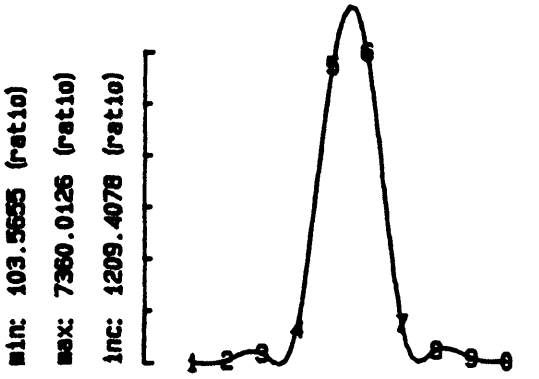

z1: -20 z2: 30 x1: 6006
i1: 132 Q: -1 M/L: .1 g4

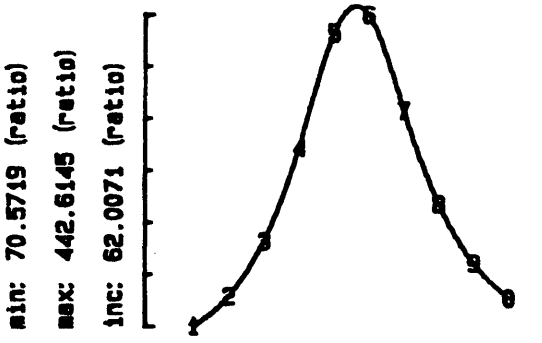

z1: -20 z2: 300 x1: 6006
i1: 132 Q: -.1 M/L: .1 g5

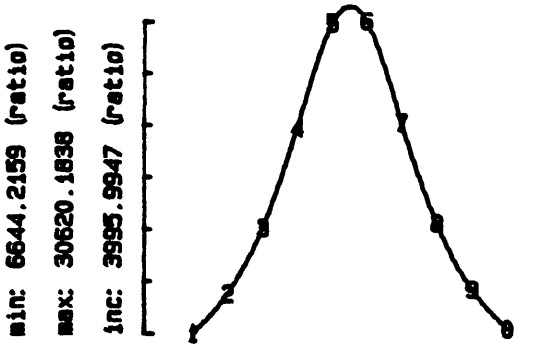

z1: -20 z2: 300 x1: 53526
i1: 132 Q: -1 M/L: .01 g6

Graphs D5

ellipticity v/t

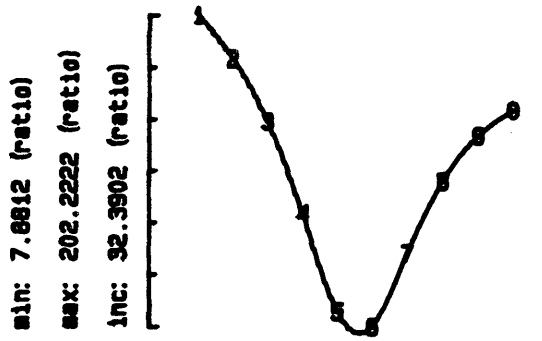

z1: -20 z2: 300 x1: 6006
i1: 132 Q: -1 M/L: 1 g1

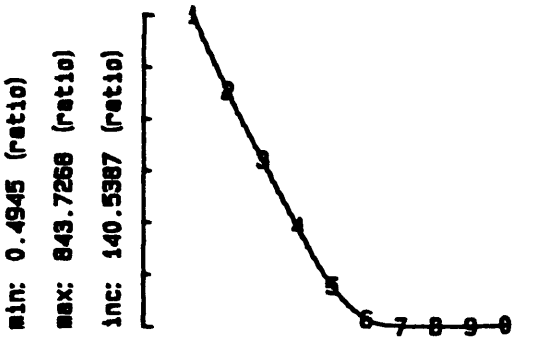

z1: -20 z2: 300 x1: 6006
i1: 132 Q: -10 M/L: .1 g2

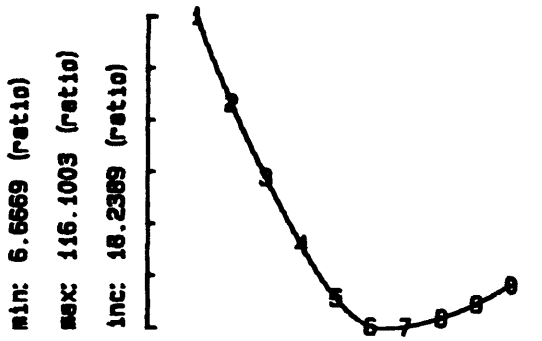

z1: -20 z2: 300 x1: 6006
i1: 132 Q: -1 M/L: .1 g3

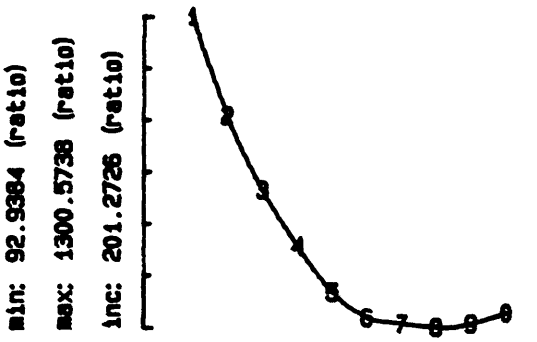

z1: -20 z2: 30 x1: 6006
i1: 132 Q: -1 M/L: .1 g4

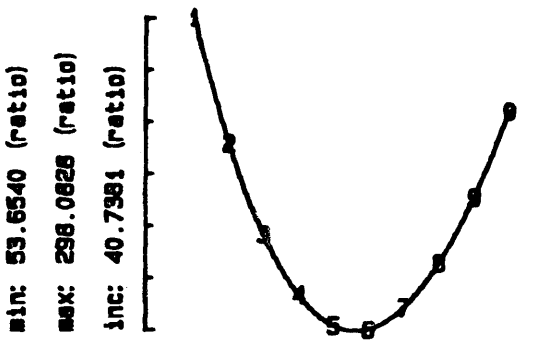

z1: -20 z2: 300 x1: 6006
i1: 132 Q: -.1 M/L: .1 g5

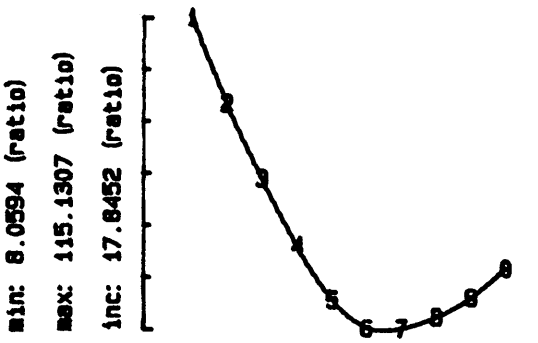

z1: -20 z2: 300 x1: 53526
i1: 132 Q: -1 M/L: .01 g6

Graphs D6

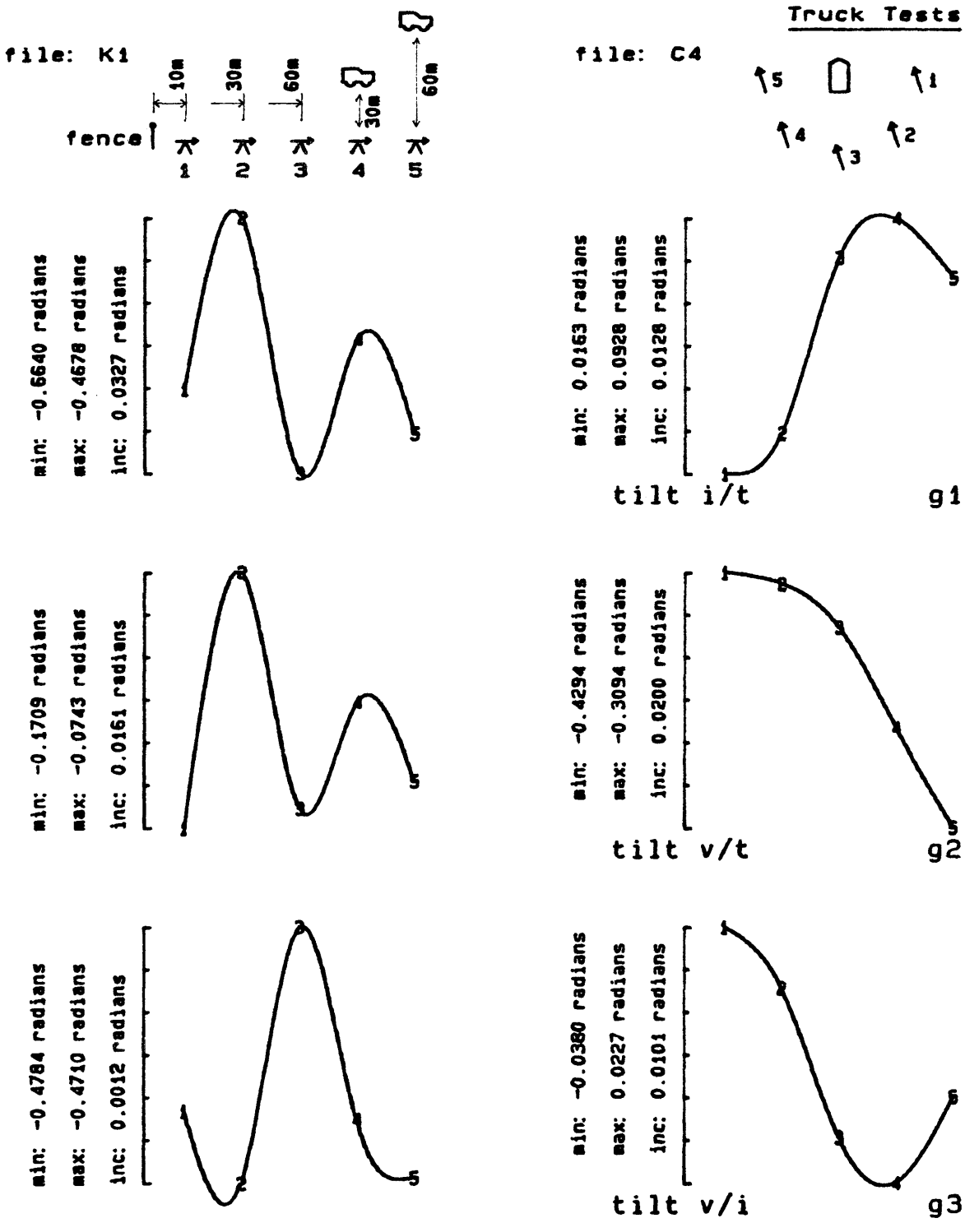
Truck Tests
file: K1
10m
30m
60m
30m
60m
fence
1
2
3
4
5
min: -0.6640 radians
max: -0.4678 radians
inc: 0.0327 radians
min: -0.1709 radians
max: -0.0743 radians
inc: 0.0161 radians
min: -0.4784 radians
max: -0.4710 radians
inc: 0.0012 radians
file: C4
5
1
4
2
3
min: 0.0163 radians
max: 0.0928 radians
inc: 0.0128 radians
tilt i/t
g1
min: -0.4294 radians
max: -0.3094 radians
inc: 0.0200 radians
tilt v/t
g2
min: -0.0380 radians
max: 0.0227 radians
inc: 0.0101 radians
tilt v/i
g3

Graphs D7

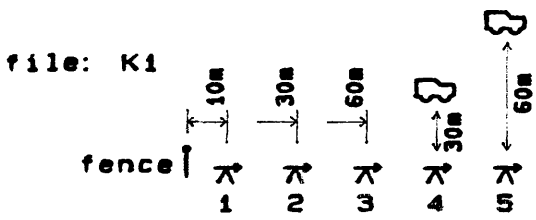

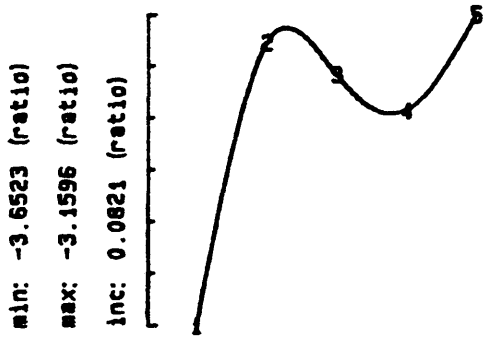

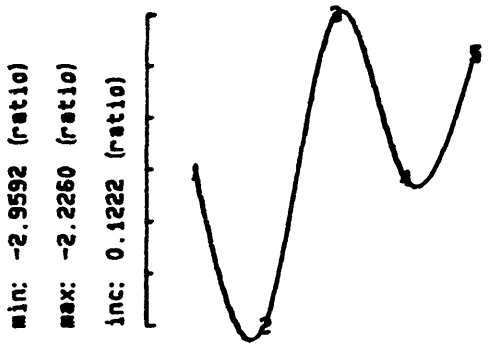

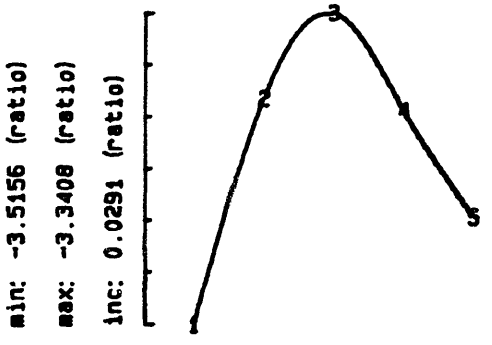

Truck Tests

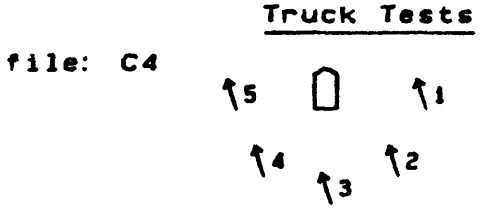

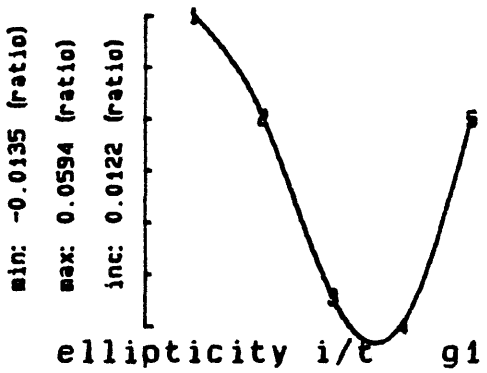

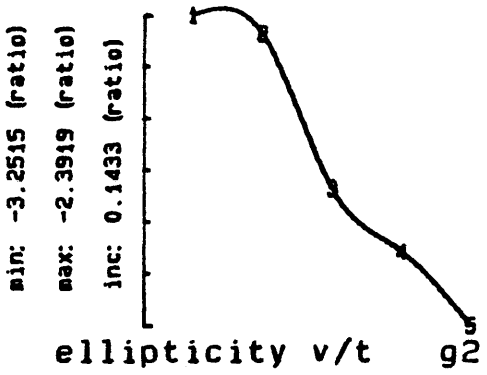

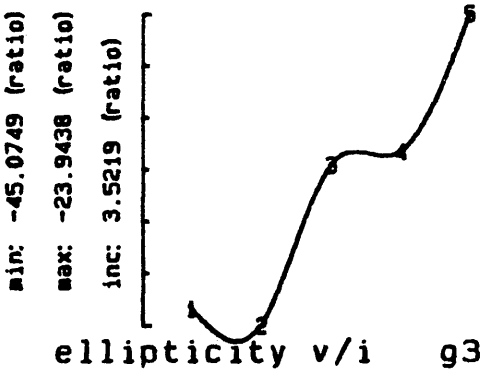

Graphs D8

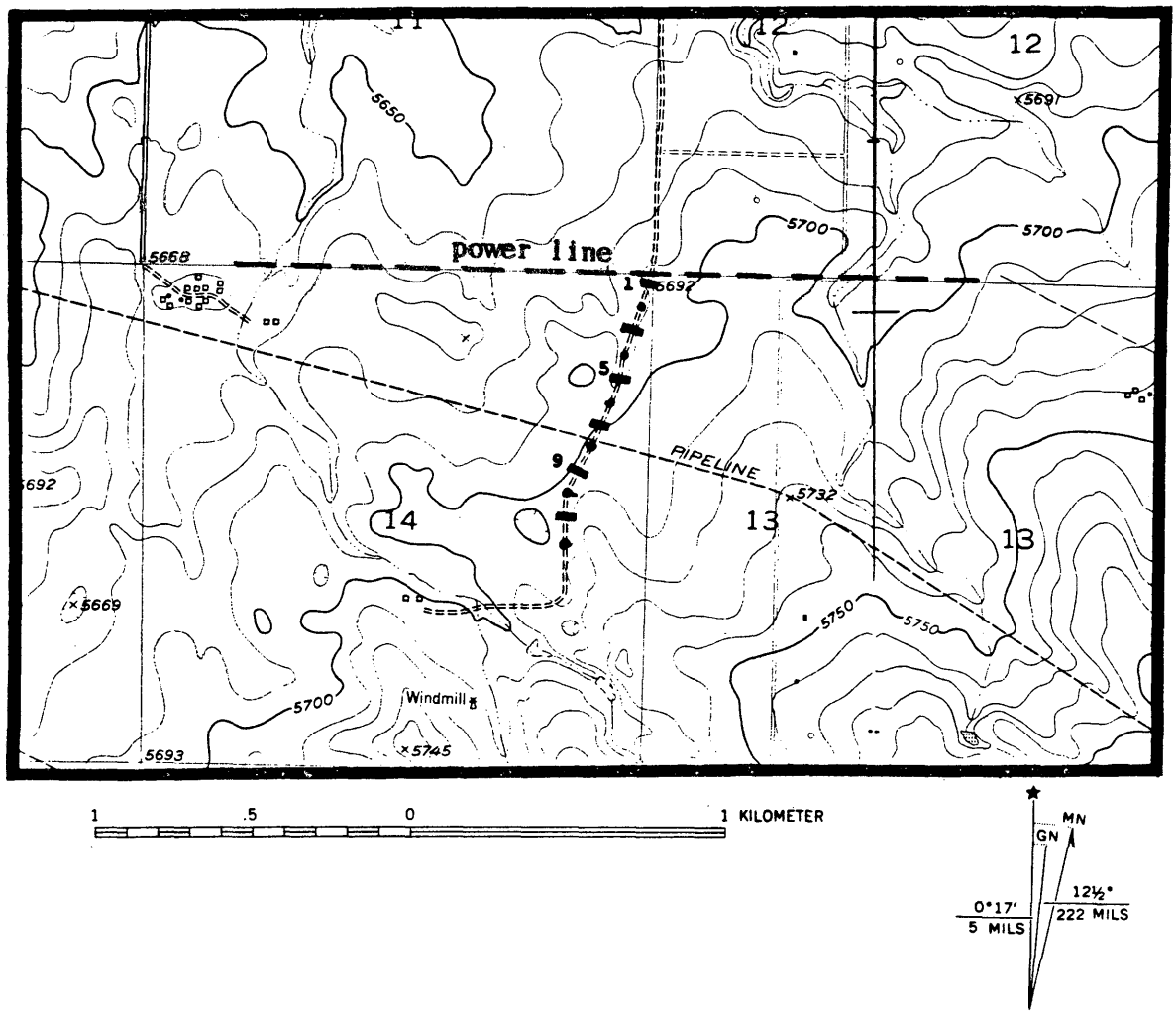

Detail map of Watkins line 1
U.S.G.S. Watkins Quadrangle;
T4S, R64W, sections 13,14
Colorado Interstate Gas Pipeline
Sensor probe orientation: due south

Map D9

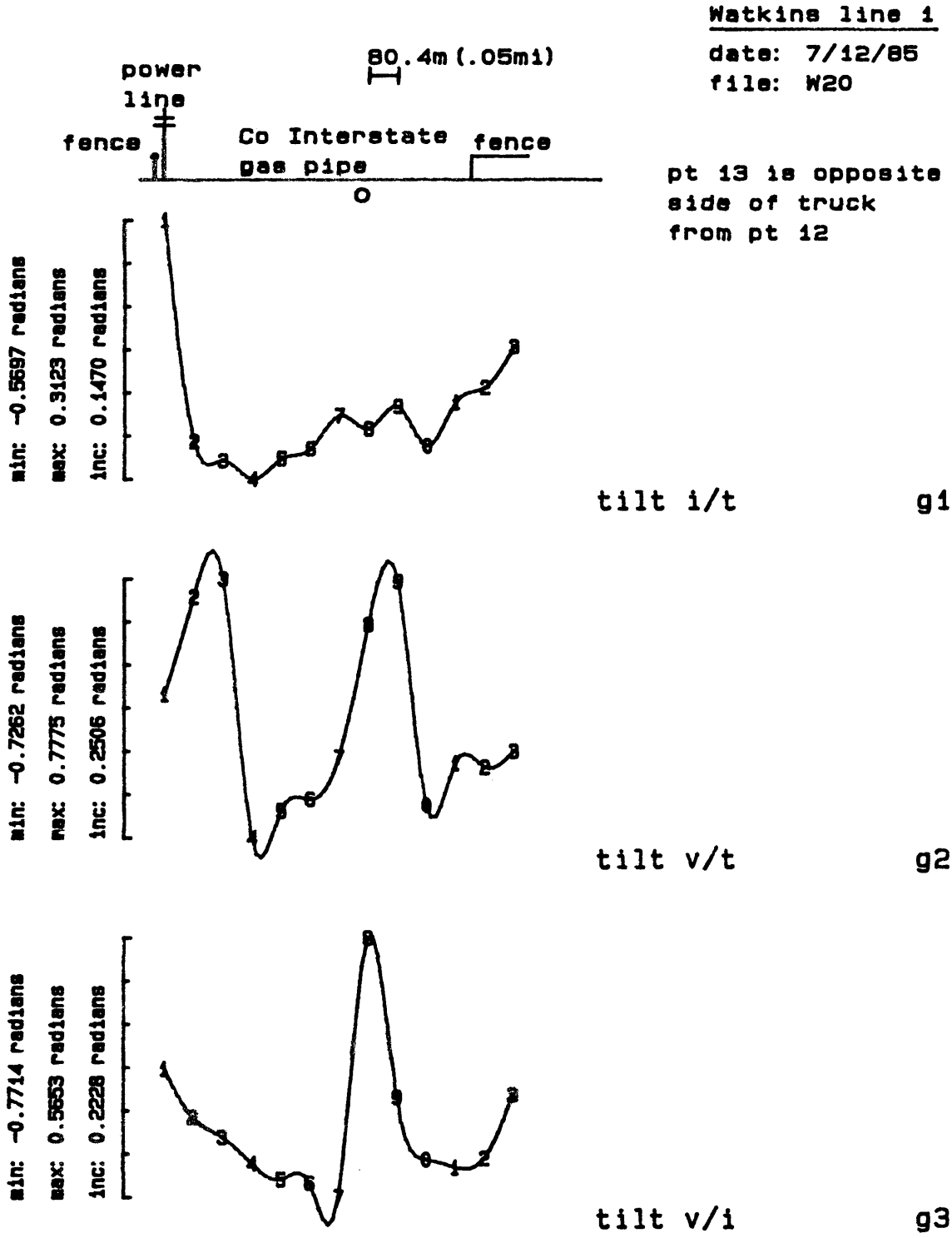
Watkins line 1
date: 7/12/85
file: W20
80.4m (.05mi)
power line
fence
Co Interstate gas pipe
fence
O
pt 13 is opposite side of truck from pt 12
min: -0.5697 radians
max: 0.3123 radians
inc: 0.1470 radians
tilt i/t g1
min: -0.7262 radians
max: 0.7775 radians
inc: 0.2506 radians
tilt v/t g2
min: -0.7714 radians
max: 0.5653 radians
inc: 0.2228 radians
tilt v/i g3

Graphs D10

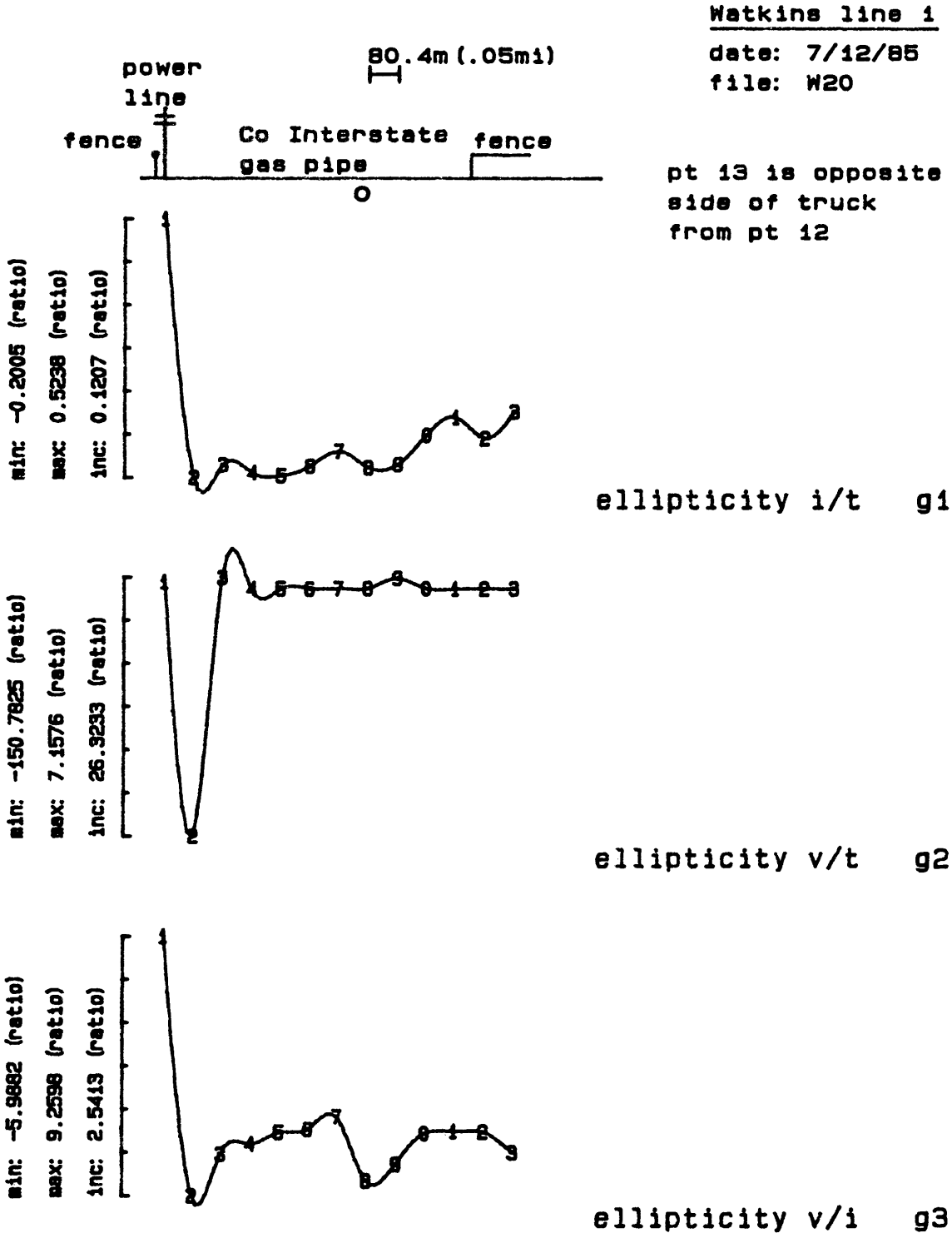
Watkins line 1
date: 7/12/85
file: W20
80.4m (.05mi)
power line
fence
Co Interstate gas pipe
fence
O
pt 13 is opposite side of truck from pt 12
min: -0.2005 (ratio)
max: 0.5238 (ratio)
inc: 0.1207 (ratio)
ellipticity i/t g1
min: -150.7825 (ratio)
max: 7.1576 (ratio)
inc: 26.9233 (ratio)
ellipticity v/t g2
min: -5.9882 (ratio)
max: 9.2598 (ratio)
inc: 2.5413 (ratio)
ellipticity v/i g3

Graphs D11

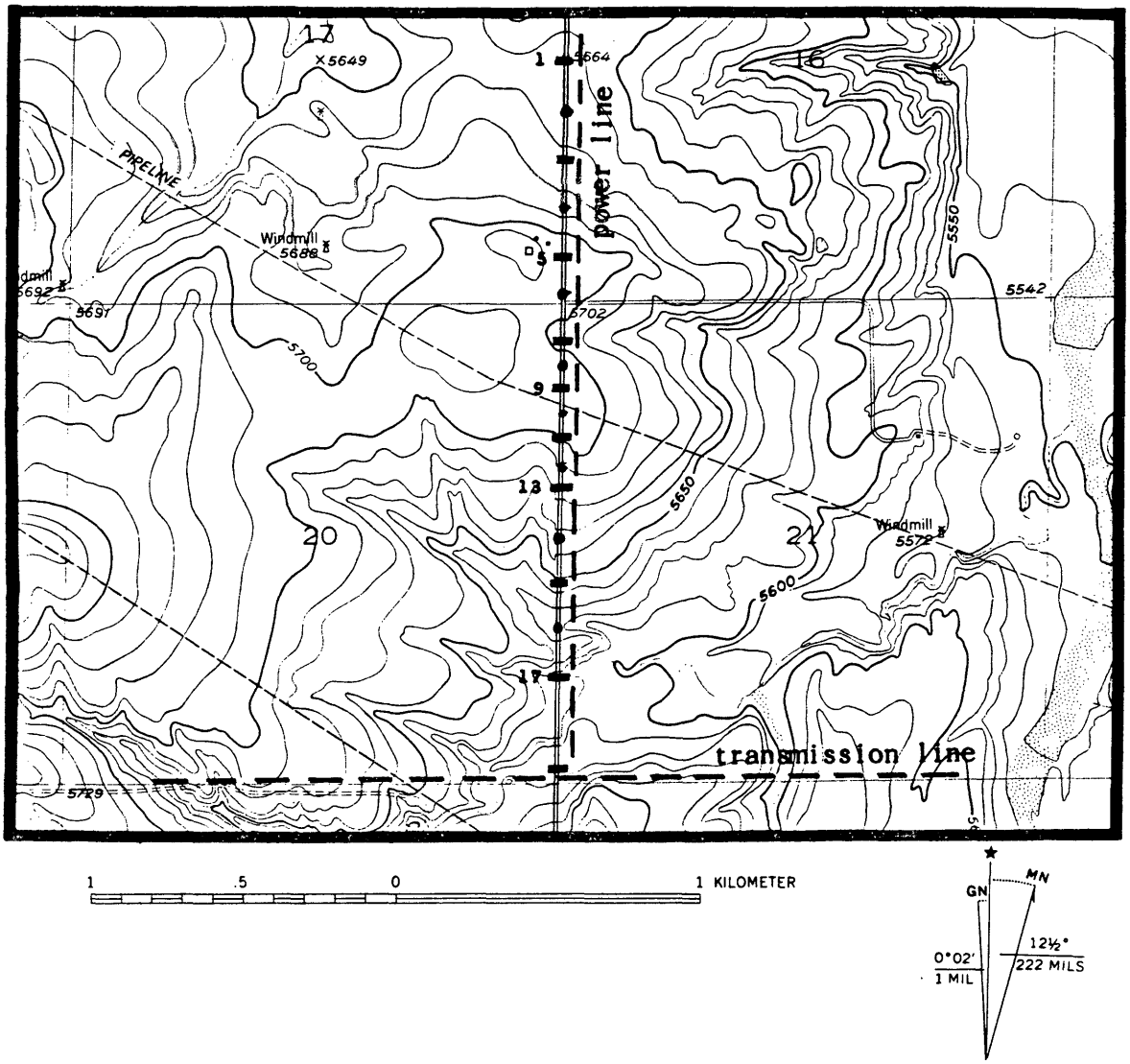

Detail map of Bennett line 1

U.S.G.S. Strasburg NW Quadrangle;

T4S, R63W, sections 16,17, 20,21

Amoco Pipeline

Chase Transportation Company Pipeline

Sensor probe orientation: due south

Map D12

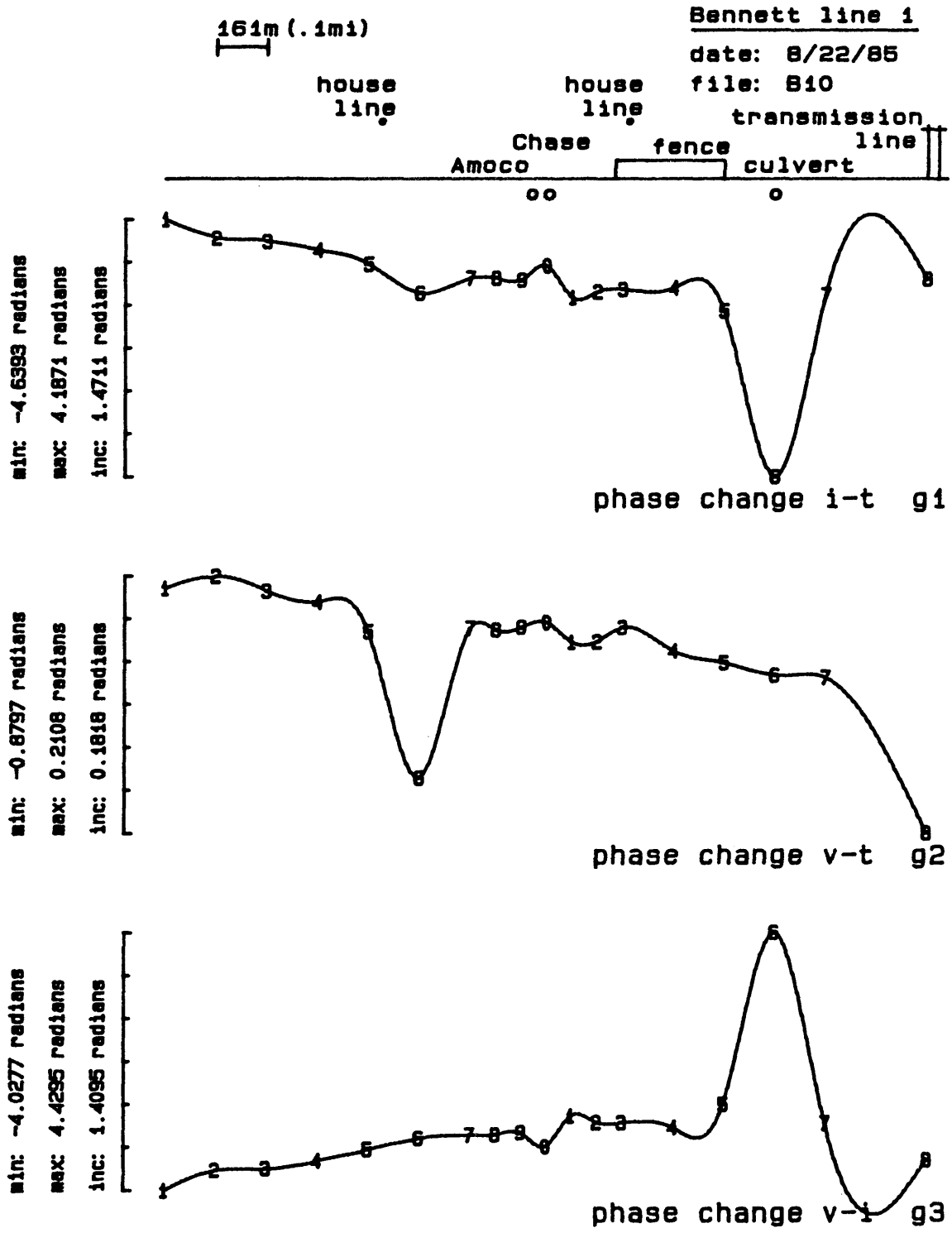
161m (.1mi)
Bennett line 1
date: 8/22/85
file: B10
house line
house line
transmission line
Chase
fence
Amoco
culvert
min: -4.6393 radians
max: 4.1871 radians
inc: 1.4711 radians
phase change i-t g1
min: -0.8797 radians
max: 0.2108 radians
inc: 0.1818 radians
phase change v-t g2
min: -4.0277 radians
max: 4.4295 radians
inc: 1.4095 radians
phase change v-i g3

Graphs D13

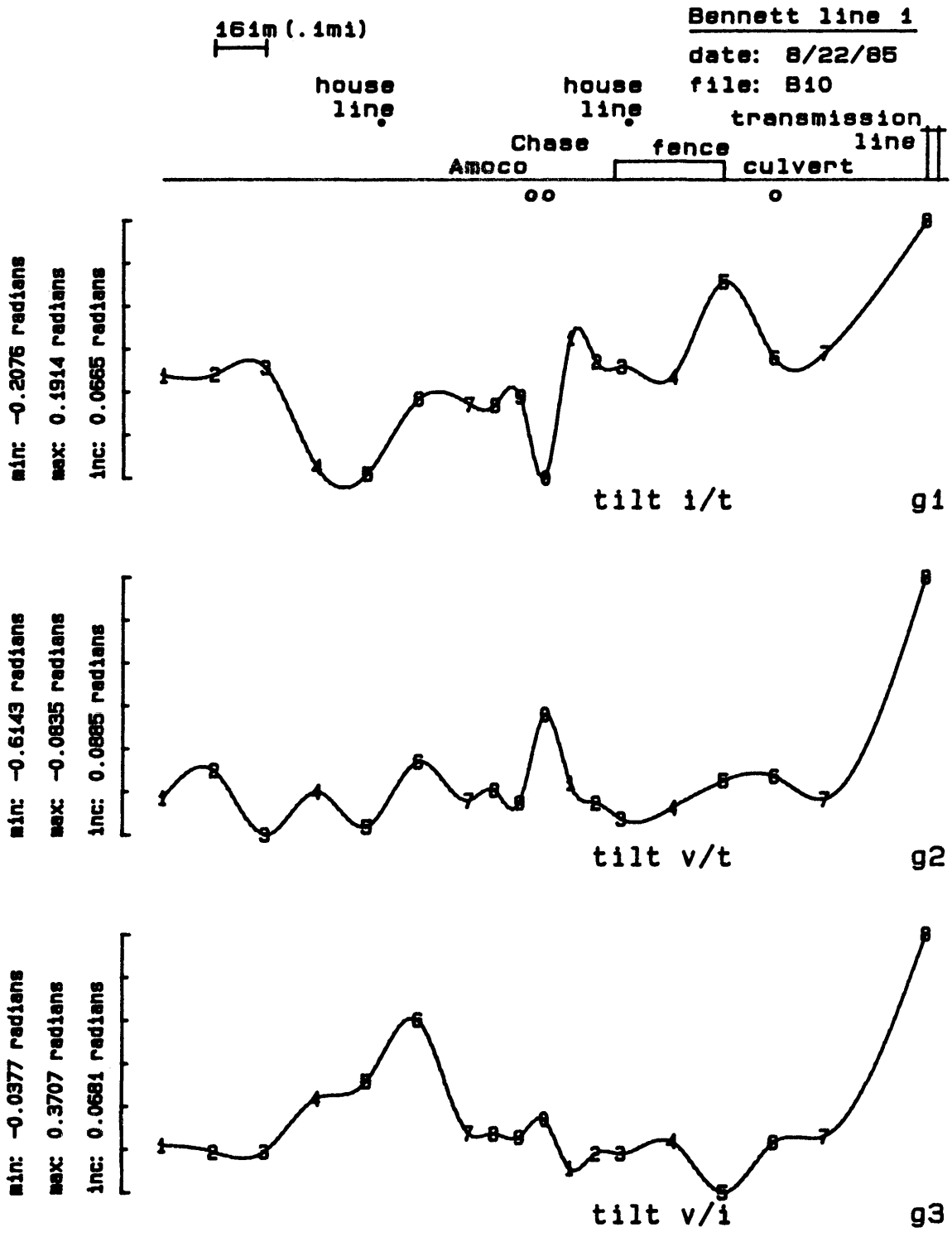
161m (.1mi)
Bennett line 1
date: 8/22/85
file: B10
house line
house line
transmission line
Chase
fence
Amoco
culvert
min: -0.2076 radians
max: 0.1914 radians
inc: 0.0665 radians
tilt i/t
g1
min: -0.6143 radians
max: -0.0835 radians
inc: 0.0885 radians
tilt v/t
g2
min: -0.0377 radians
max: 0.3707 radians
inc: 0.0681 radians
tilt v/i
g3

Graphs D14

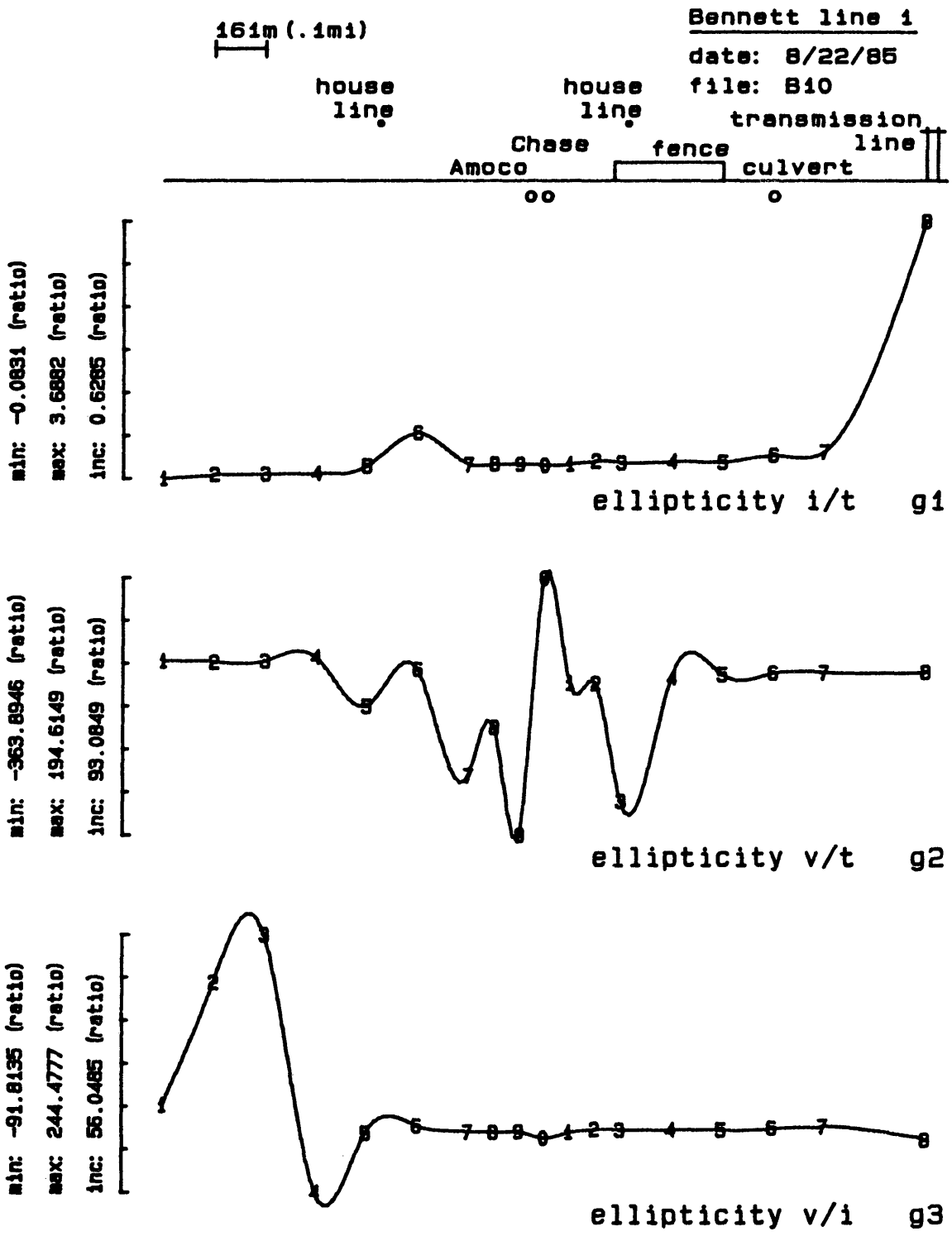
161m (.1mi)
Bennett line 1
date: 8/22/85
file: B10
house line
house line
transmission line
Chase
fence
Amoco
culvert
min: -0.0831 (ratio)
max: 3.6882 (ratio)
inc: 0.6285 (ratio)
ellipticity i/t g1
min: -363.8946 (ratio)
max: 194.6149 (ratio)
inc: 93.0849 (ratio)
ellipticity v/t g2
min: -91.8135 (ratio)
max: 244.4777 (ratio)
inc: 56.0485 (ratio)
ellipticity v/i g3

Graphs D15

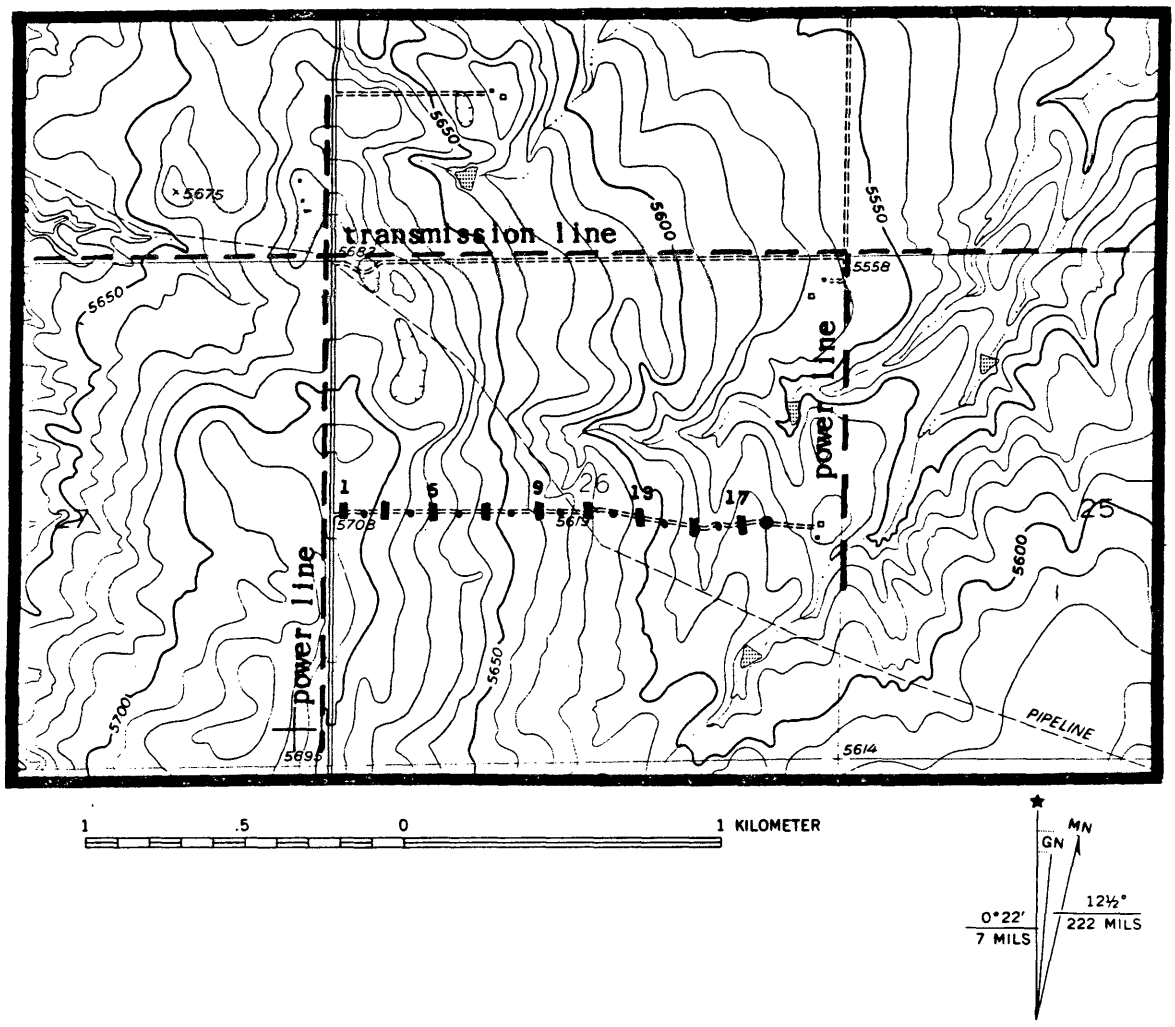

Detail map of Bennett line 4

U.S.G.S. Strasburg NW Quadrangle;

T4S, R63W, section 26

Amoco Pipeline

Sensor probe orientation: due east

Map D16

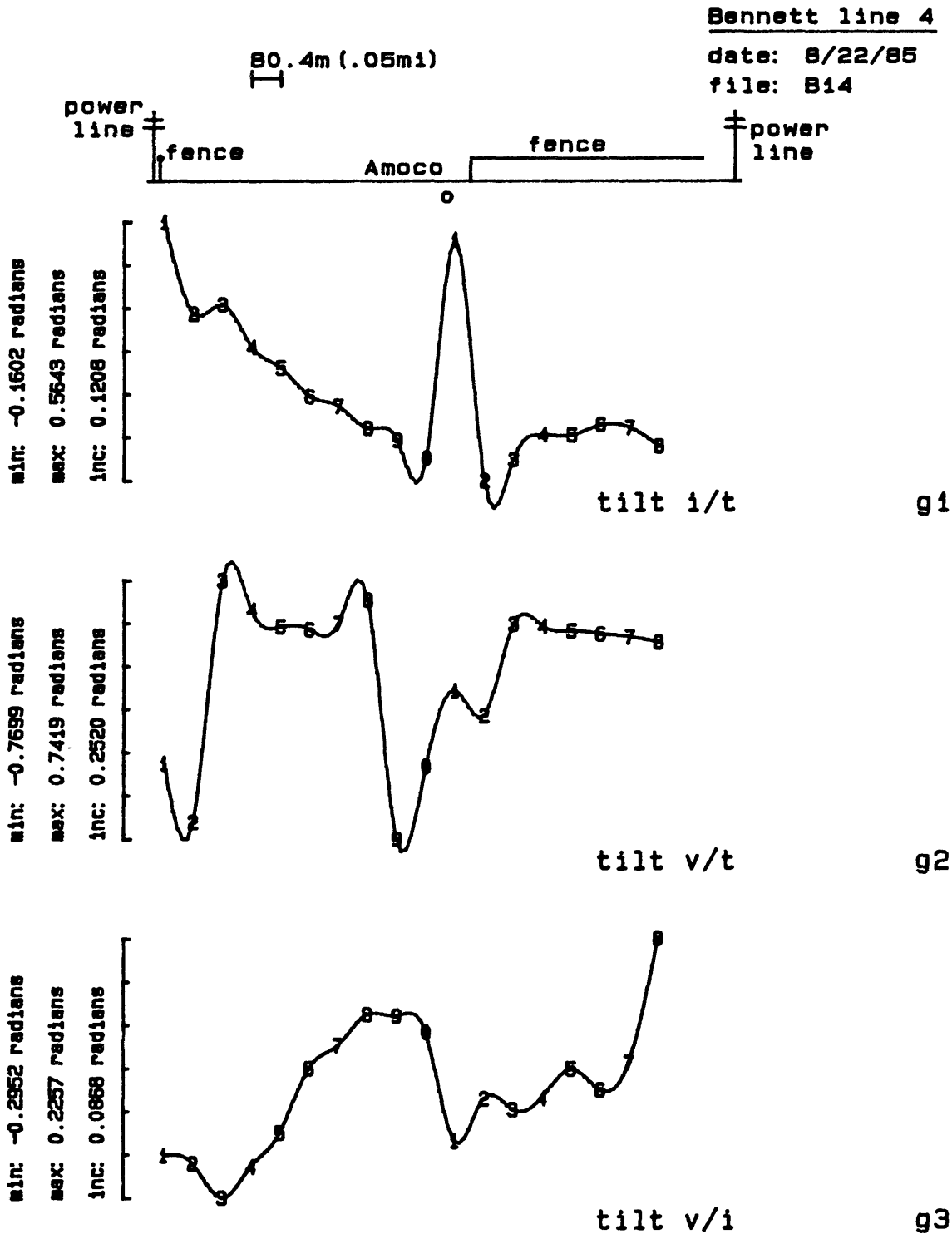
Bennett line 4
date: 8/22/85
file: B14
80.4m (.05mi)
power line
fence
Amoco
fence
power line
o
min: -0.1602 radians
max: 0.5643 radians
inc: 0.1208 radians
tilt i/t
g1
min: -0.7699 radians
max: 0.7419 radians
inc: 0.2520 radians
tilt v/t
g2
min: -0.2952 radians
max: 0.2257 radians
inc: 0.0868 radians
tilt v/i
g3

Graphs D17

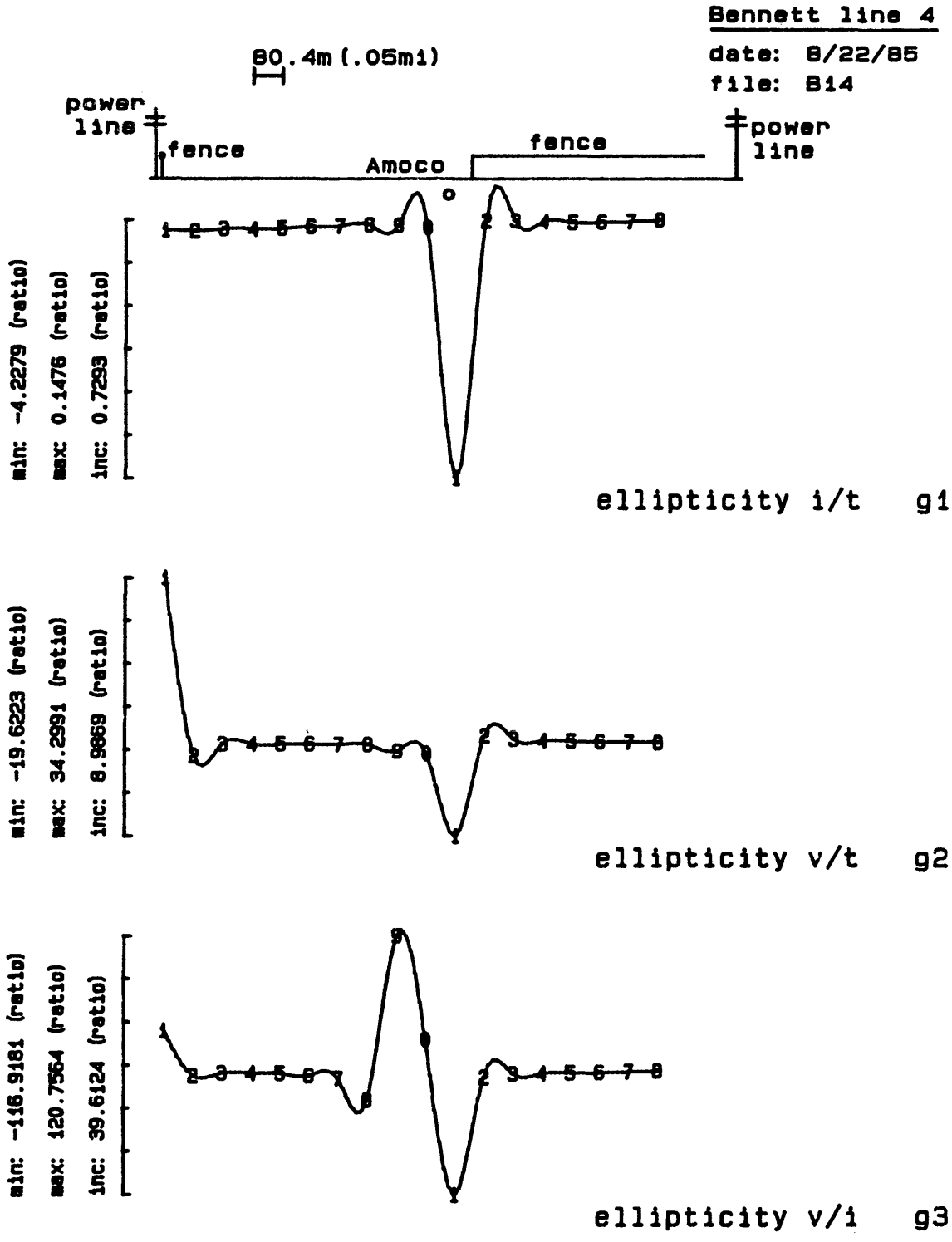
Bennett line 4
date: 8/22/85
file: B14
80.4m (.05mi)
power line
fence
Amoco
fence
power line
min: -4.2279 (ratio)
max: 0.1476 (ratio)
inc: 0.7293 (ratio)
ellipticity i/t g1
min: -19.6223 (ratio)
max: 34.2991 (ratio)
inc: 8.9869 (ratio)
ellipticity v/t g2
min: -116.9181 (ratio)
max: 120.7564 (ratio)
inc: 39.6124 (ratio)
ellipticity v/i g3

Graphs D18

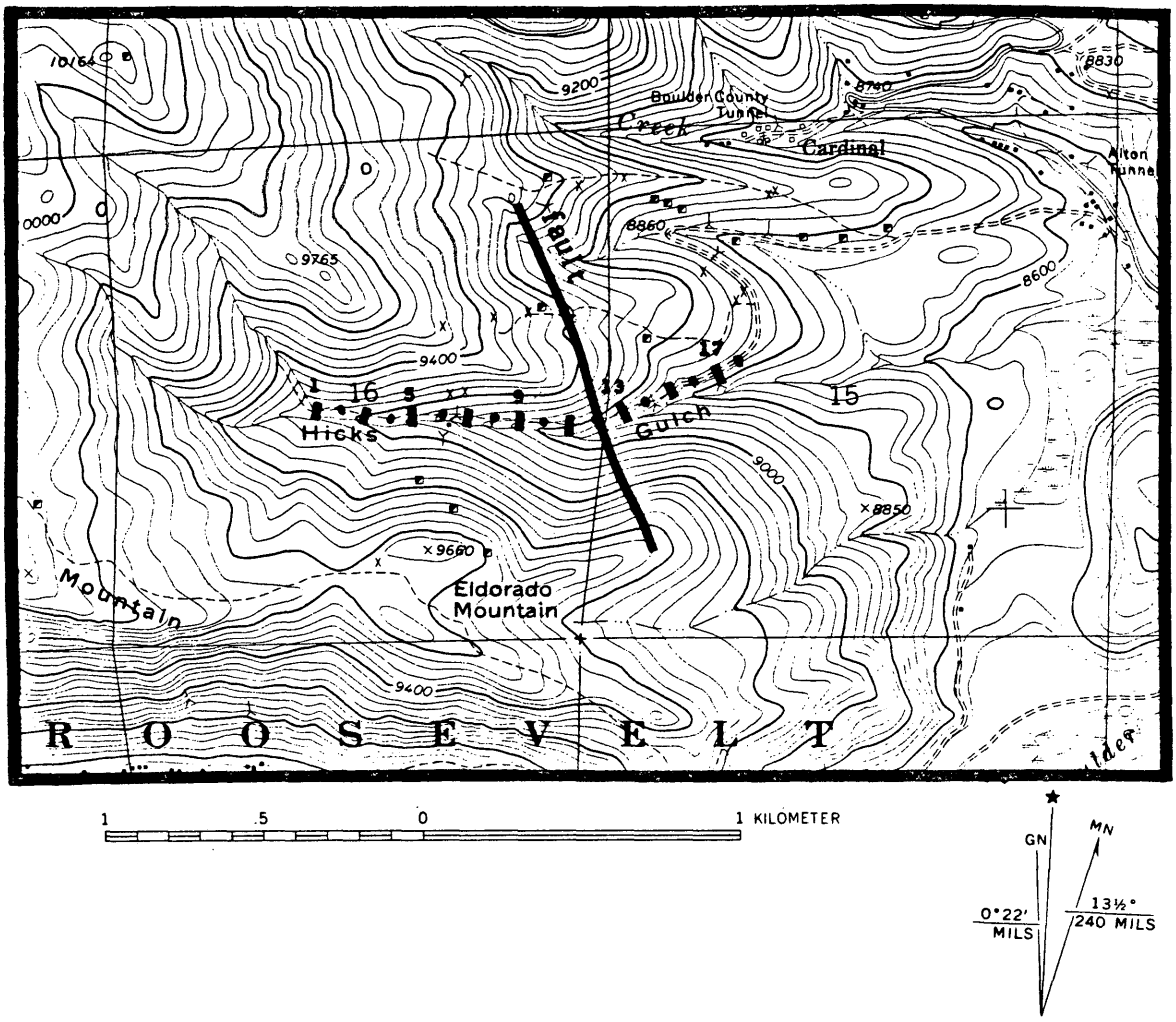

Detail map of Nederland line 1

U.S.G.S. Nederland Quadrangle;

T1S, R73W, sections 15,16

Geologic reference: U.S.G.S. gelogic quadrangle GQ 833

Wild Wagoner-Apex Fault

strike: N 22° W, dip 75° NE

Sensor probe orientation: N 60° E

Map D19

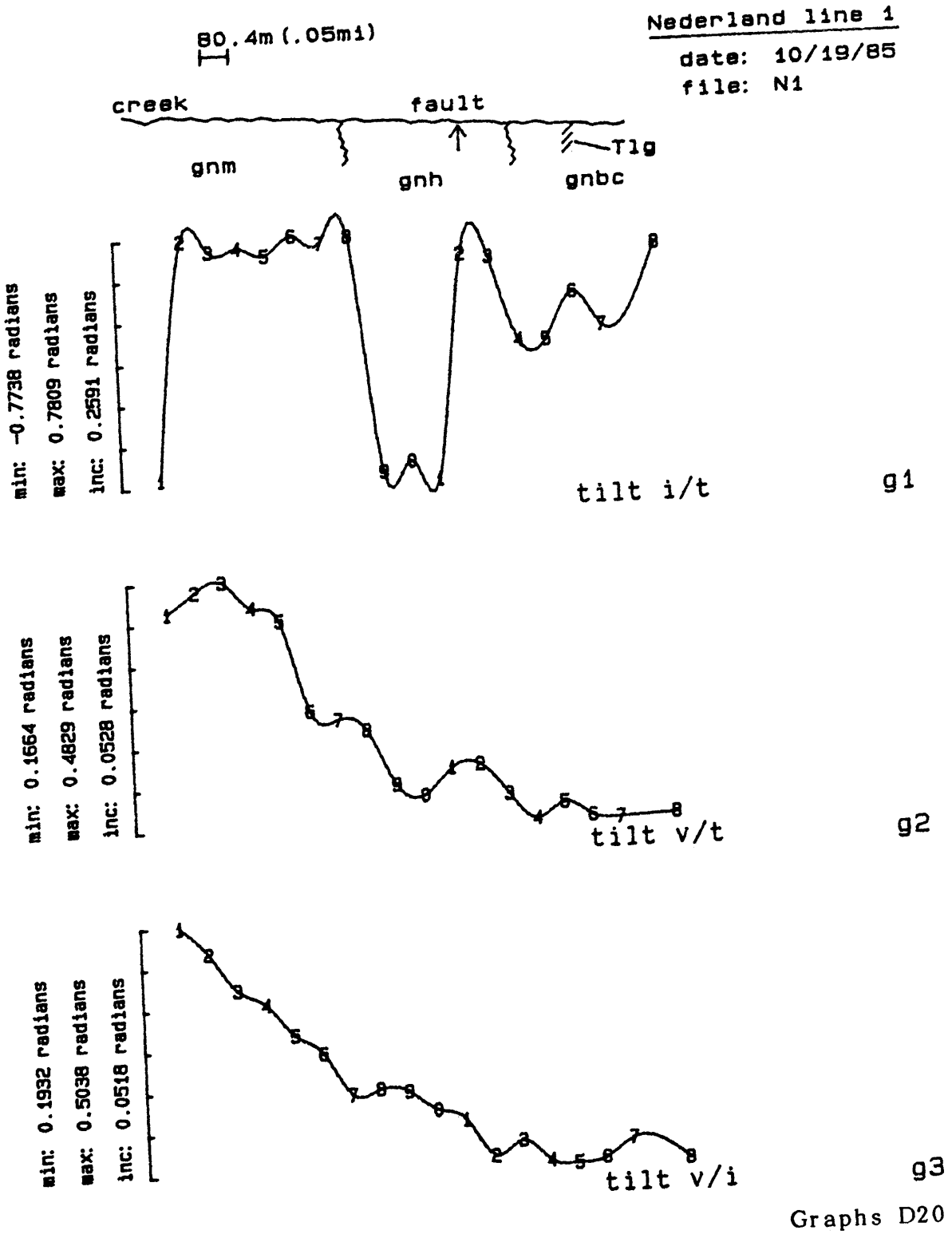
80.4m (.05mi)
Nederland line 1
date: 10/19/85
file: N1
creek
fault
Tlg
gnm
gnh
gnbc
min: -0.7738 radians
max: 0.7809 radians
inc: 0.2591 radians
tilt i/t
g1
min: 0.1664 radians
max: 0.4829 radians
inc: 0.0528 radians
tilt v/t
g2
min: 0.1932 radians
max: 0.5038 radians
inc: 0.0518 radians
tilt v/i
g3

Graphs D20

T-3179

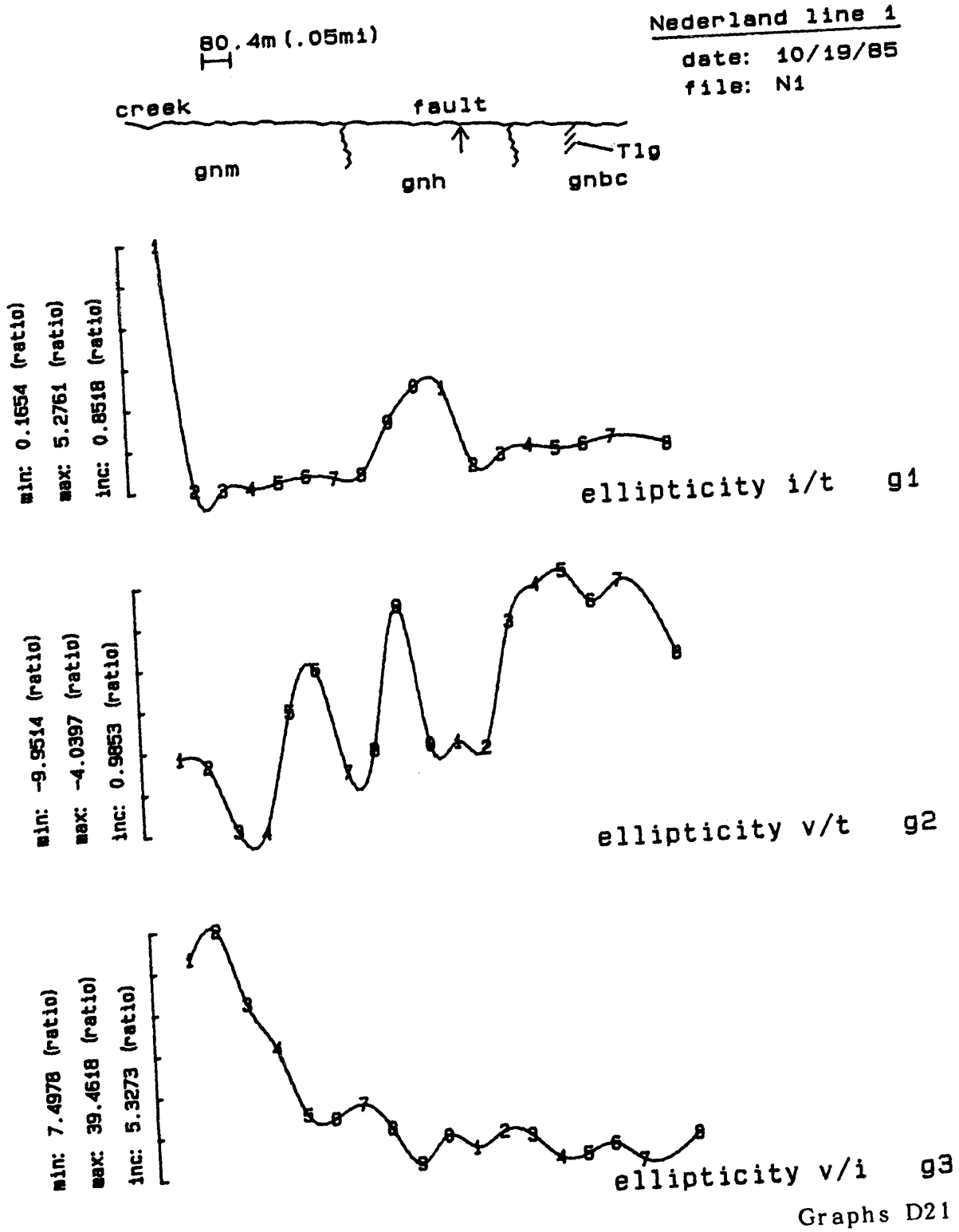

Graphs D21

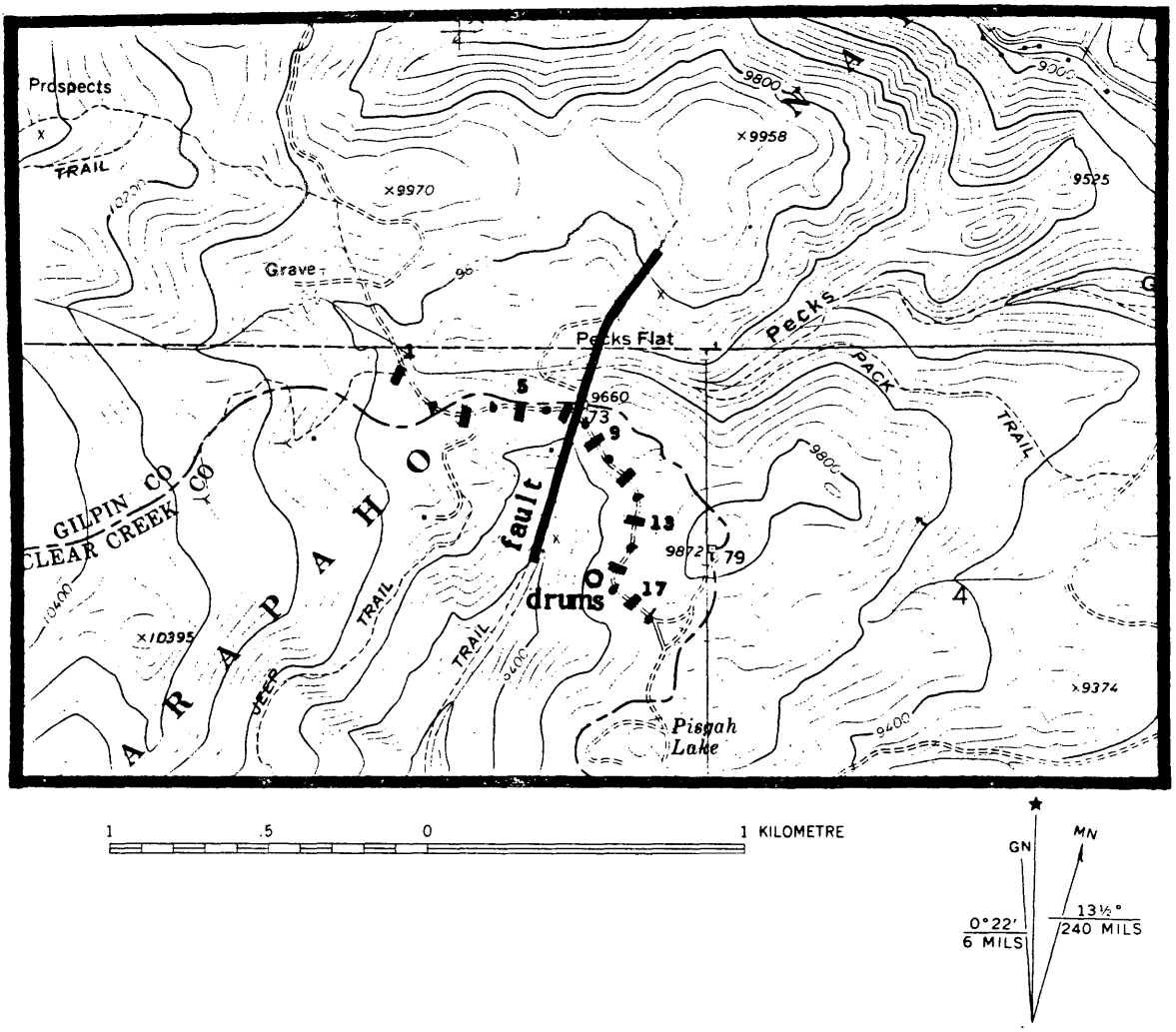

Detail map of Central City line 1

U.S.G.S. Central City Quadrangle;

T3S, R73W, section 4

Geologic reference: U.S.G.S. gelogic quadrangle GQ 267

Wild Wagoner-Apex Fault

strike: N 20° E, dip 90° NE

Sensor probe orientation: S 70° E

Map D22

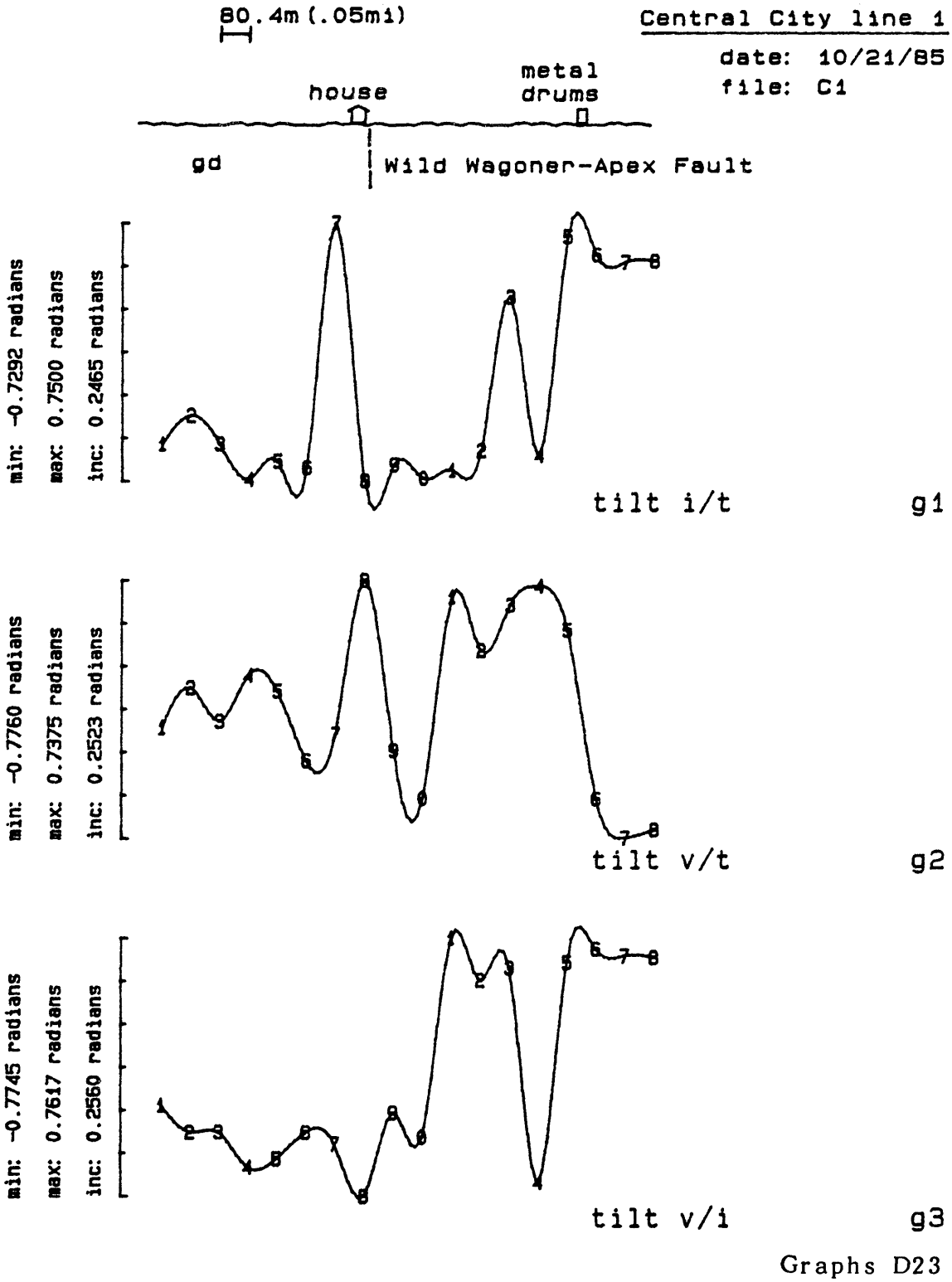
80.4m (.05mi)
Central City line 1
date: 10/21/85
file: C1
house
metal drums
gd
Wild Wagoner-Apex Fault
min: -0.7292 radians
max: 0.7500 radians
inc: 0.2465 radians
tilt i/t
g1
min: -0.7760 radians
max: 0.7375 radians
inc: 0.2523 radians
tilt v/t
g2
min: -0.7745 radians
max: 0.7617 radians
inc: 0.2560 radians
tilt v/i
g3

Graphs D23

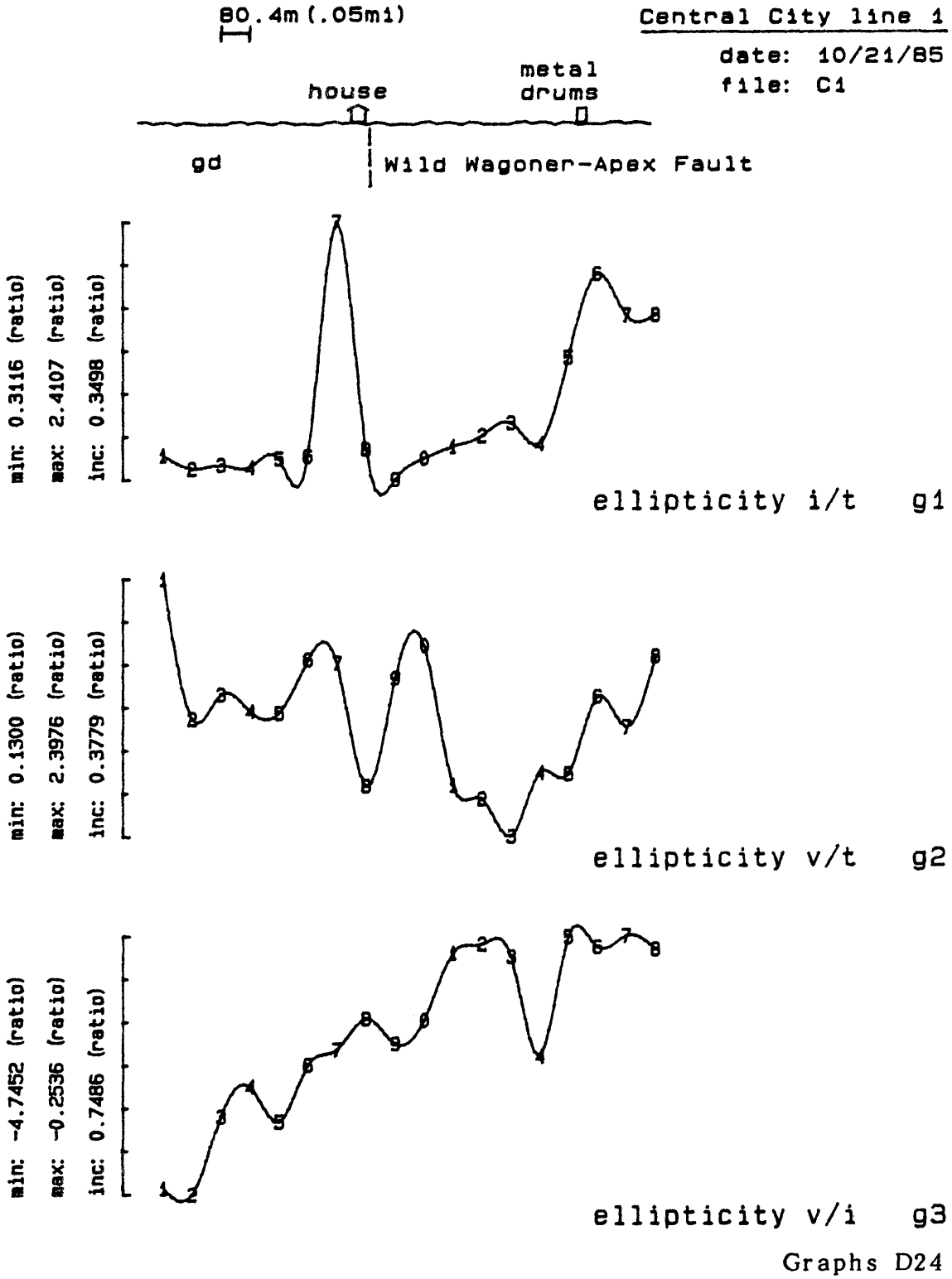
80.4m (.05mi)
Central City line 1
date: 10/21/85
file: C1
house
metal drums
gd
Wild Wagoner-Apex Fault
min: 0.3116 (ratio)
max: 2.4107 (ratio)
inc: 0.3498 (ratio)
ellipticity i/t g1
min: 0.1300 (ratio)
max: 2.3976 (ratio)
inc: 0.3779 (ratio)
ellipticity v/t g2
min: -4.7452 (ratio)
max: -0.2536 (ratio)
inc: 0.7486 (ratio)
ellipticity v/i g3

Graphs D24

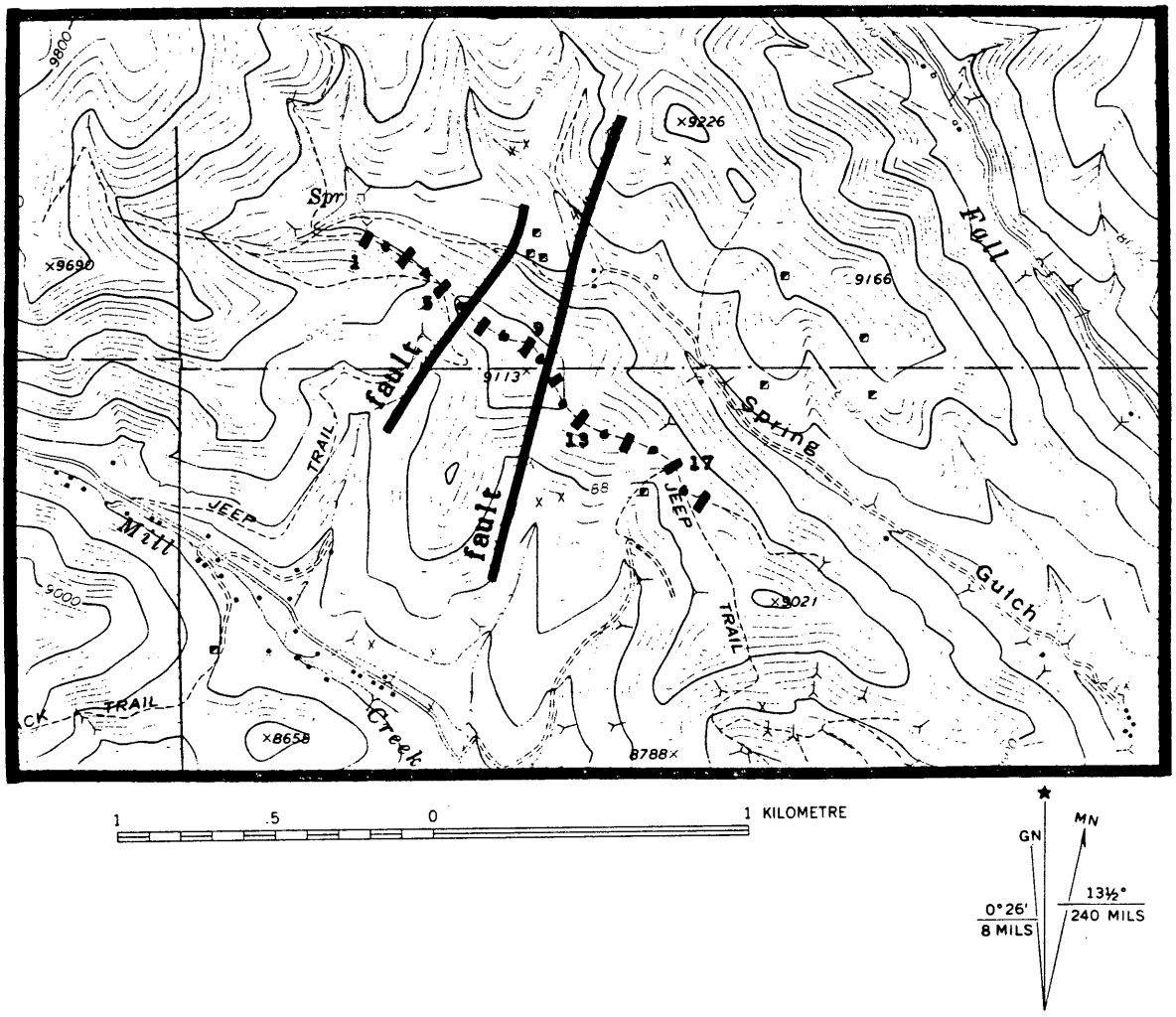

Detail map of Central City line 3

U.S.G.S. Central City Quadrangle;

T3S, R73W

Geologic reference: U.S.G.S. gelogic quadrangle GQ 267

Wild Wagoner-Apex Fault

strike: N 20° E, dip 90° NE

Sensor probe orientation: S 70° E

Map D25

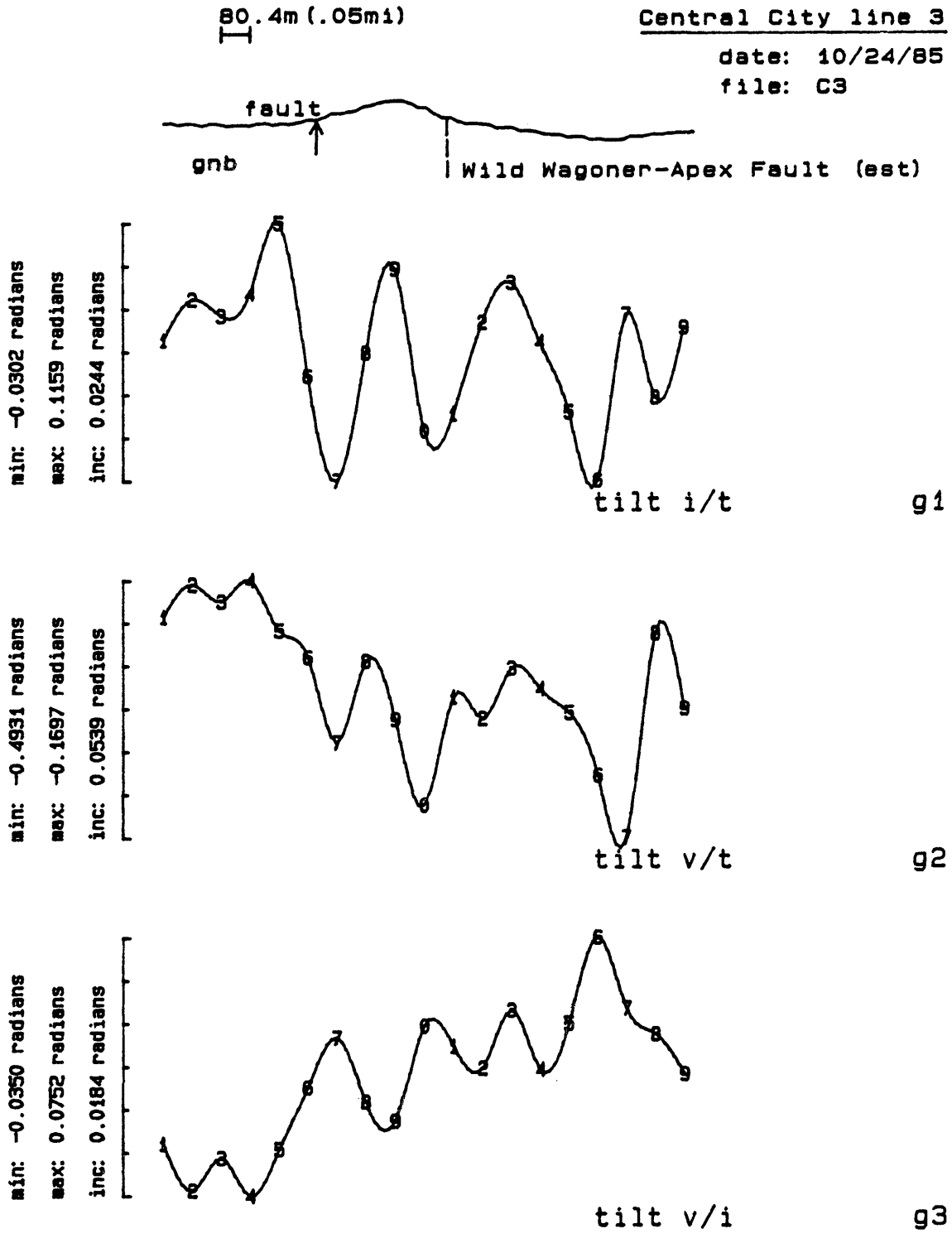
80.4m (.05mi)
Central City line 3
date: 10/24/85
file: C3
fault
gnb
Wild Wagoner-Apex Fault (est)
min: -0.0302 radians
max: 0.1159 radians
inc: 0.0244 radians
tilt i/t
g1
min: -0.4931 radians
max: -0.1697 radians
inc: 0.0539 radians
tilt v/t
g2
min: -0.0350 radians
max: 0.0752 radians
inc: 0.0184 radians
tilt v/i
g3

Graphs D26

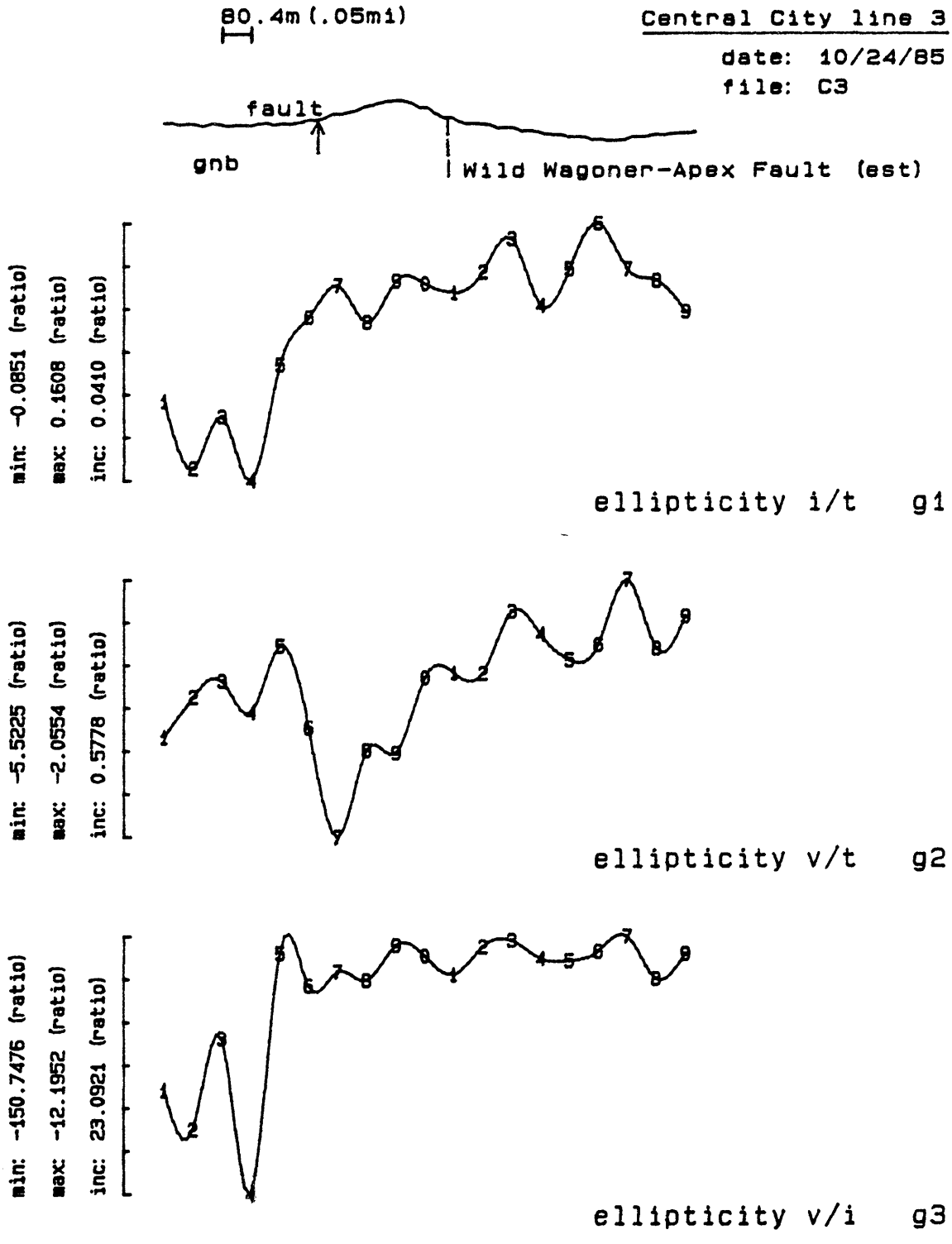
80.4m (.05mi)
Central City line 3
date: 10/24/85
file: C3
fault
gnb
Wild Wagoner-Apex Fault (est)
min: -0.0851 (ratio)
max: 0.1608 (ratio)
inc: 0.0410 (ratio)
ellipticity i/t g1
min: -5.5225 (ratio)
max: -2.0554 (ratio)
inc: 0.5778 (ratio)
ellipticity v/t g2
min: -150.7476 (ratio)
max: -12.1952 (ratio)
inc: 23.0921 (ratio)
ellipticity v/i g3

Graphs D27

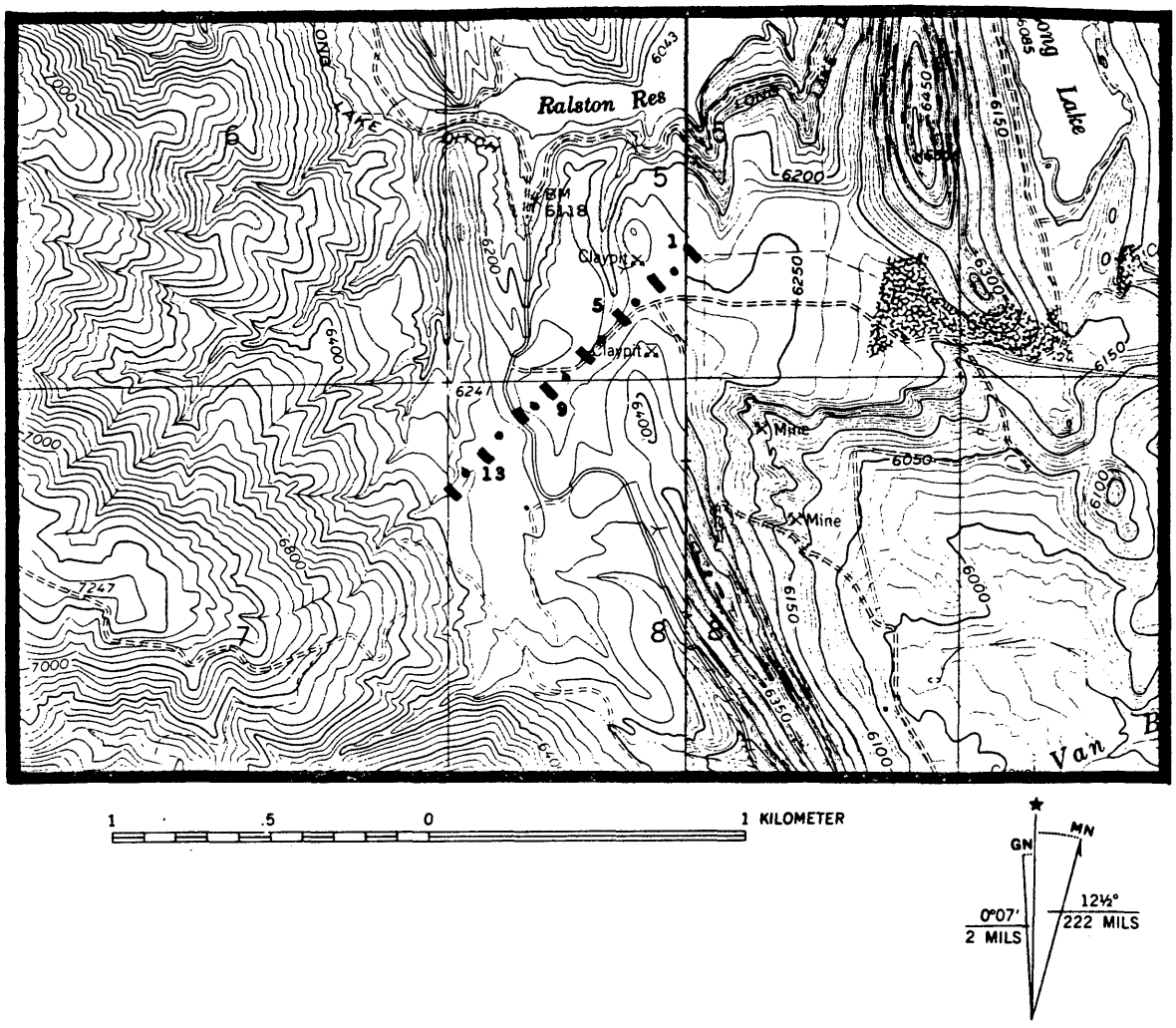

Detail map of Golden line 1
U.S.G.S. Ralston Buttes Quadrangle;
U.S.G.S. Golden Quadrangle;
T3S, R70W, sections 5,8
Geologic reference: U.S.G.S. prof. paper 520
Sensor probe orientation: S 50° W

Map D28

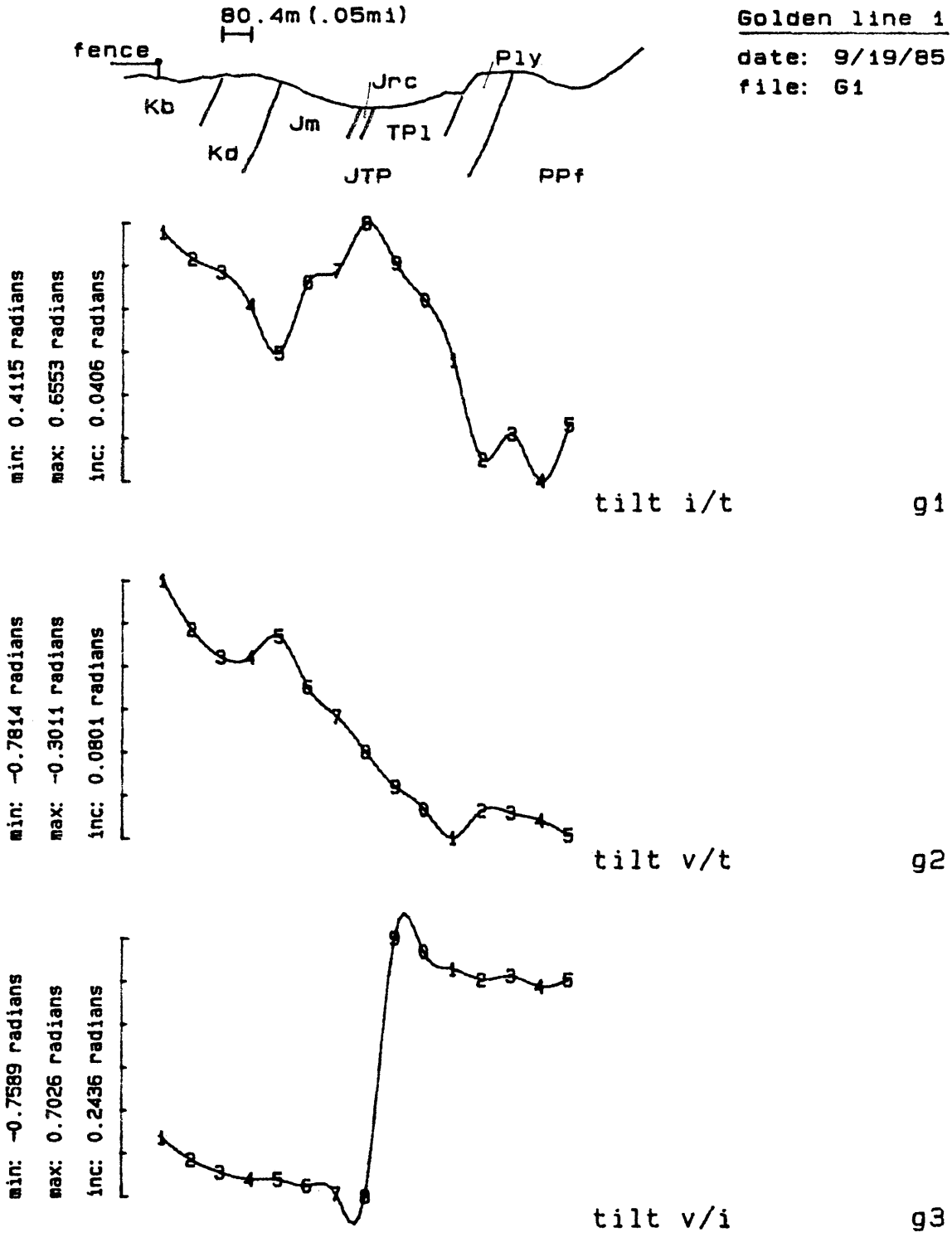
80.4m(.05mi)
fence
Kb
Kd
Jm
Jrc
TPl
JTP
Ply
PPf
Golden line 1
date: 9/19/85
file: G1
min: 0.4115 radians
max: 0.6553 radians
inc: 0.0406 radians
tilt i/t
g1
min: -0.7814 radians
max: -0.3011 radians
inc: 0.0801 radians
tilt v/t
g2
min: -0.7589 radians
max: 0.7026 radians
inc: 0.2436 radians
tilt v/i
g3

Graphs D29

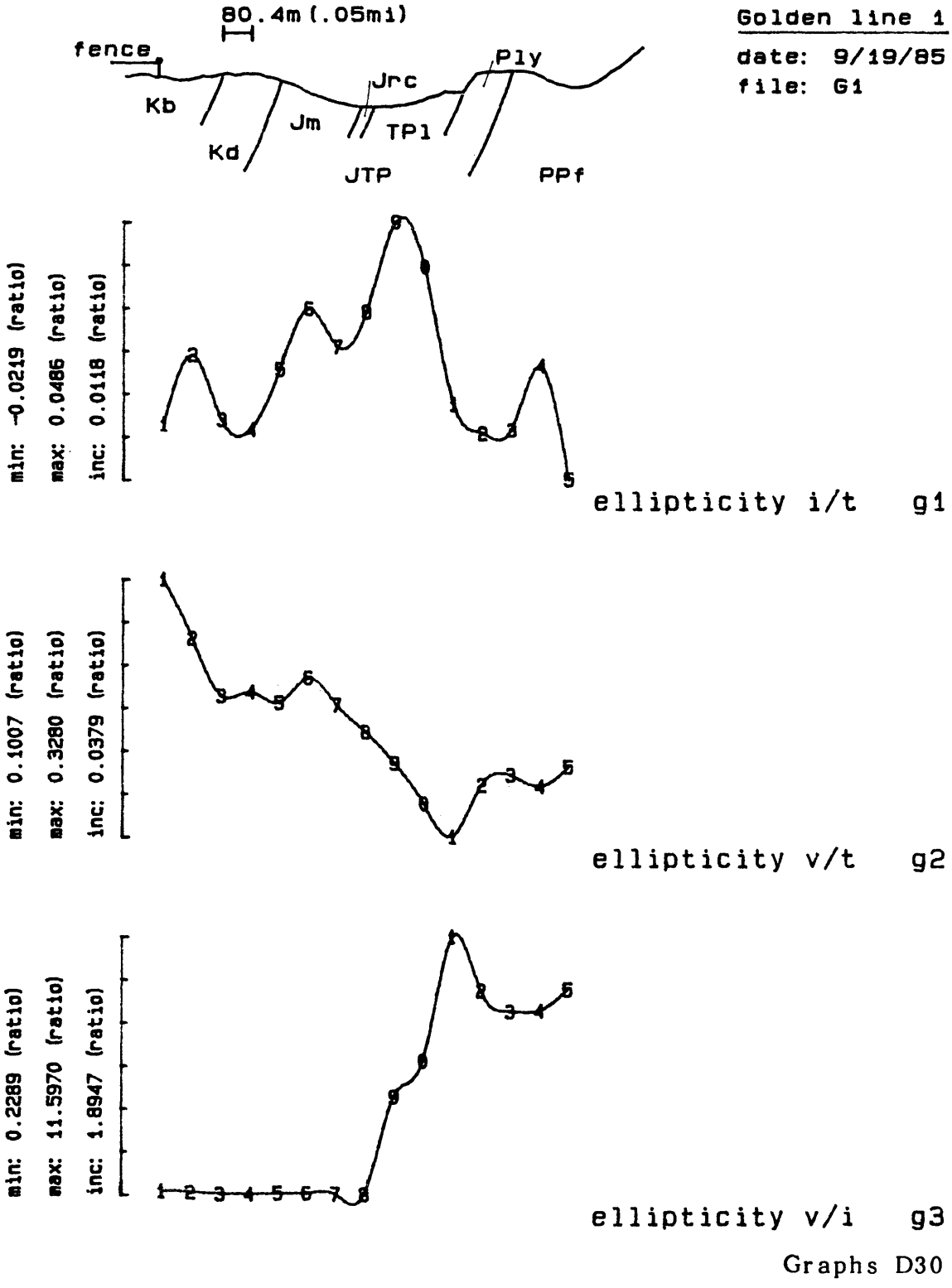
80.4m (.05mi)
fence
Kb
Kd
Jm
Jrc
TP1
JTP
Ply
PPf
Golden line 1
date: 9/19/85
file: G1
min: -0.0219 (ratio)
max: 0.0486 (ratio)
inc: 0.0118 (ratio)
ellipticity i/t g1
min: 0.1007 (ratio)
max: 0.3280 (ratio)
inc: 0.0379 (ratio)
ellipticity v/t g2
min: 0.2289 (ratio)
max: 11.5970 (ratio)
inc: 1.8947 (ratio)
ellipticity v/i g3

Graphs D30

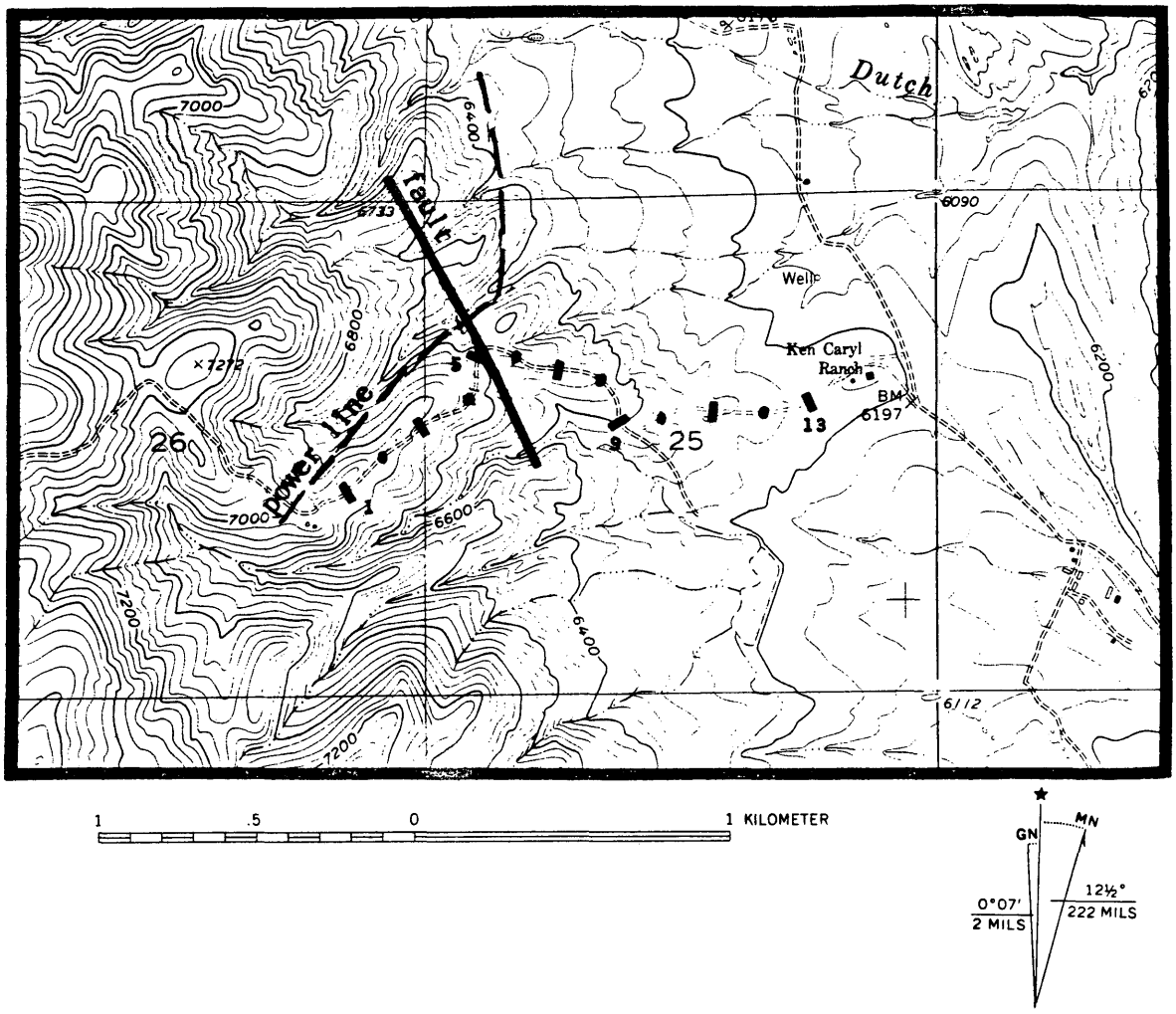

Detail map of Indian Hills line 1

U.S.G.S. Indian Hills Quadrangle;

T5S, R70W, sections 25,26

Geologic reference: U.S.G.S. gelogic quadrangle GQ 1073

Ken Caryl Fault

strike: N 45° W, dip 90° NE

Sensor probe orientation: N 45° E

Map D31

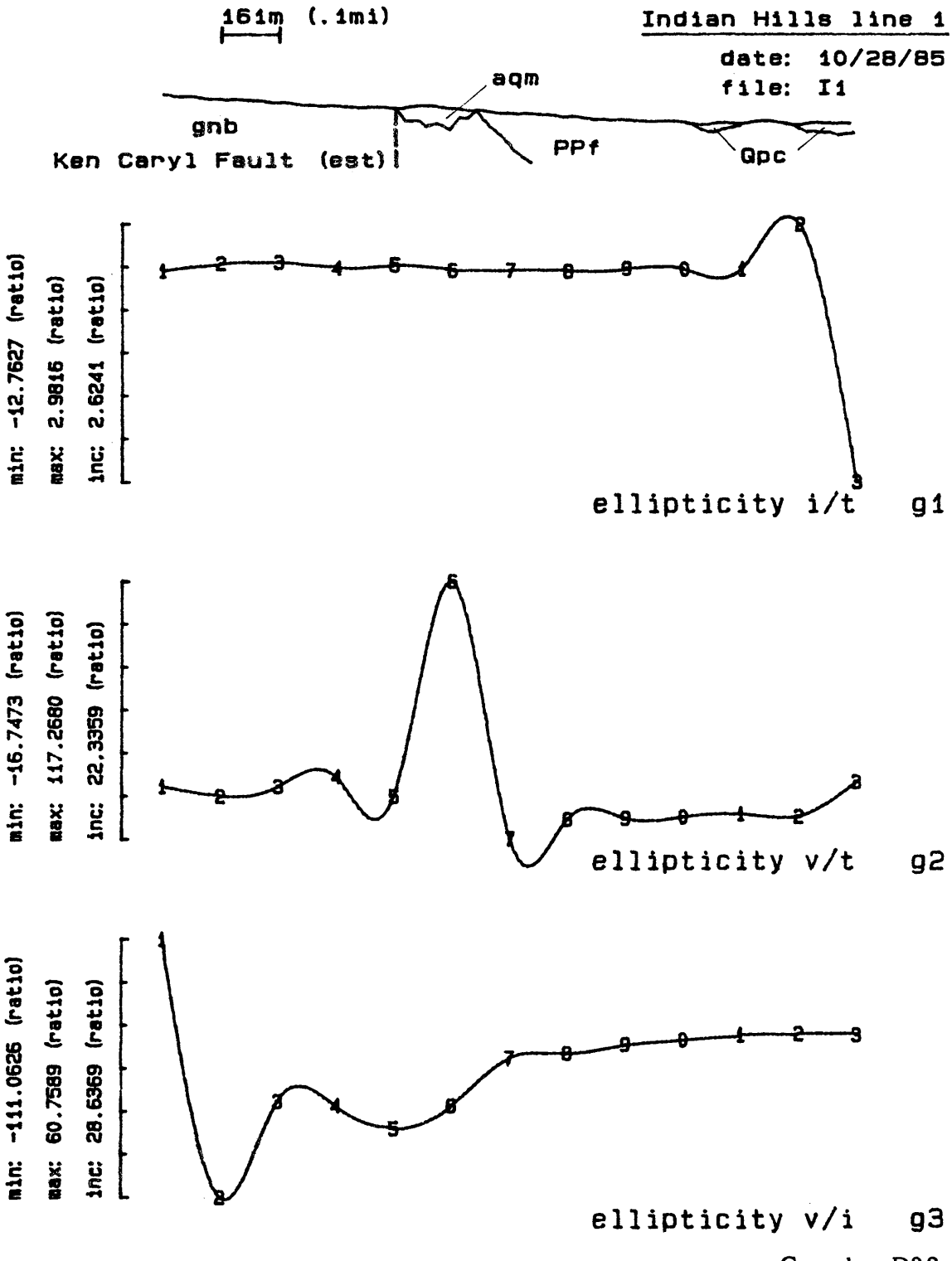
161m (.1mi)
Indian Hills line 1
date: 10/28/85
file: I1
aqm
gnb
Ken Caryl Fault (est)
PPf
Qpc
min: -12.7627 (ratio)
max: 2.9816 (ratio)
inc: 2.6241 (ratio)
ellipticity i/t g1
min: -16.7473 (ratio)
max: 117.2680 (ratio)
inc: 22.3359 (ratio)
ellipticity v/t g2
min: -111.0626 (ratio)
max: 60.7589 (ratio)
inc: 28.6369 (ratio)
ellipticity v/i g3

Graphs D32

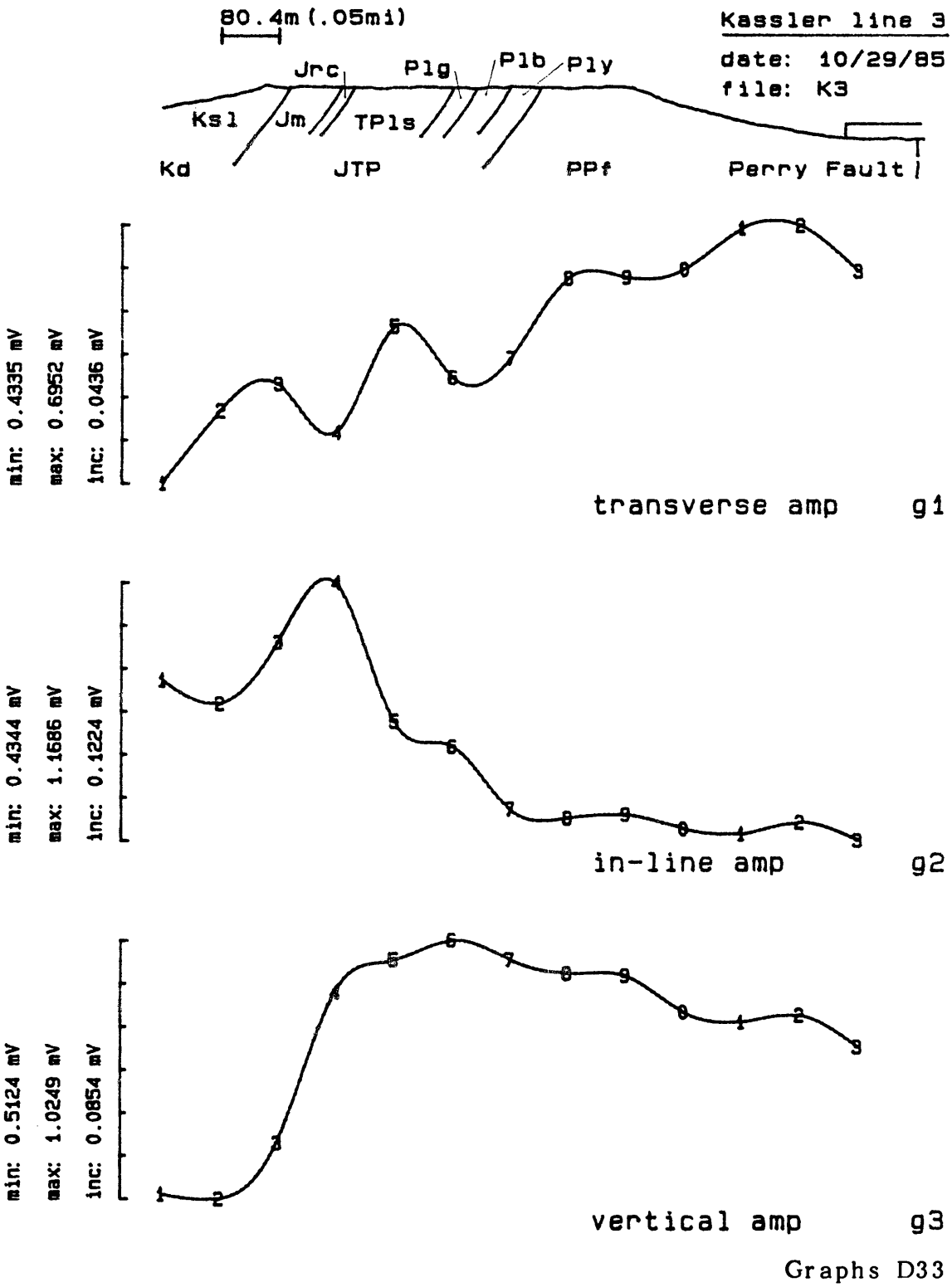
80.4m (.05mi)
Kassler line 3
date: 10/29/85
file: K3
Jrc
Plg
Plb
Ply
Ksl
Jm
TPls
Kd
JTP
PPf
Perry Fault
min: 0.4335 mV
max: 0.6952 mV
inc: 0.0436 mV
transverse amp
g1
min: 0.4344 mV
max: 1.1686 mV
inc: 0.1224 mV
in-line amp
g2
min: 0.5124 mV
max: 1.0249 mV
inc: 0.0854 mV
vertical amp
g3

Graphs D33